

The spin temperature of high-redshift damped Lyman- α systems

N. Kanekar^{1*}, J. X. Prochaska², A. Smette³, S. L. Ellison⁴, E. V. Ryan-Weber⁵, E. Momjian⁶,
F. H. Briggs⁷, W. M. Lane⁸, J. N. Chengalur¹, T. Delafosse², J. Grave², D. Jacobsen⁴,
and A. G. de Bruyn^{9,10}

¹National Centre for Radio Astrophysics, TIFR, Post Bag 3, Ganeshkhind, Pune 411 007, India; ²UCO/Lick Observatory, UC Santa Cruz, Santa Cruz, CA 95064, USA; ³European Southern Observatory, Alonso de Cordova 3107, Casilla 19001, Vitacura, Santiago, Chile; ⁴Department of Physics and Astronomy, University of Victoria, B.C., V8P 1A1, Canada; ⁵Swinburne University of Technology, Mail H30, P.O. Box 218, Hawthorn, 3122 VIC, Australia; ⁶National Radio Astronomy Observatory, 1003 Lopezville Road, Socorro, NM 87801, USA; ⁷RSAA, The Australian National University, Mount Stromlo Observatory, ACT 2611, Australia; ⁸Naval Research Laboratory, Code 7213, 4555 Overlook Ave SW, Washington, DC 20375, USA; ⁹Kapteyn Astronomical Institute, University of Groningen, PO Box 800, 9700 AV Groningen, The Netherlands; ¹⁰ASTRON, PO Box 2, 7990 AA Dwingeloo, The Netherlands

Accepted yyyy month dd. Received yyyy month dd; in original form yyyy month dd

ABSTRACT

We report results from a program aimed at investigating the temperature of neutral gas in high-redshift damped Lyman- α absorbers (DLAs). This involved (1) HI 21cm absorption studies of a large sample of DLAs towards radio-loud quasars, (2) very long baseline interferometric studies to measure the low-frequency quasar core fractions, and (3) optical/ultraviolet spectroscopy to determine DLA metallicities and the velocity widths of low-ionization metal lines.

Including literature data, our sample consists of 37 DLAs with estimates of the harmonic-mean spin temperature T_s . We find a statistically significant (4σ) difference between the T_s distributions in the high- z ($z > 2.4$) and low- z ($z < 2.4$) DLA samples. The high- z sample contains more systems with high spin temperature, $T_s \gtrsim 1000$ K. The T_s distributions in DLAs and the Galaxy are also significantly ($\approx 6\sigma$) different, with more high- T_s sightlines in DLAs than in the Milky Way. The high T_s values in the high- z DLAs of our sample arise due to low fractions of the cold neutral medium (CNM). Only two of 23 DLAs at $z > 1.7$ have T_s values indicating CNM fractions $> 20\%$, comparable to the median value ($\approx 27\%$) in the Galaxy.

We tested whether the HI column density measured towards the optical quasar might be systematically different from that towards the radio core by comparing the HI column densities inferred from HI 21cm emission studies at different spatial resolutions (≈ 15 pc – 1 kpc) in the Large Magellanic Cloud. The high-resolution N_{HI} values are, on average, larger than the smoothed ones for $N_{\text{HI}} > 10^{21}$ cm⁻², but lower than the smoothed N_{HI} estimates for $N_{\text{HI}} < 10^{21}$ cm⁻². Since there are far more DLAs with low N_{HI} values than high ones, the use of the optical N_{HI} value for the radio sightline results in a statistical tendency to under-estimate DLA spin temperatures.

For 29 DLAs with metallicity estimates, we confirm the presence of an anti-correlation between T_s and metallicity $[Z/H]$, at 3.5σ significance via a non-parametric Kendall-tau test. This result was obtained with the assumption that the DLA covering factor is equal to the core fraction. However, Monte Carlo simulations show that the significance of the result is only marginally decreased if the covering factor and the core fraction are uncorrelated, or if there is a random error in the inferred covering factor.

We also find statistically significant evidence for redshift evolution in DLA spin temperatures even for the DLA sub-sample at $z > 1$. Since all DLAs at $z > 1$ have angular diameter distances comparable to or larger than those of their background quasars, they have similar efficiency in covering the quasars. We conclude that low covering factors in high- z DLAs cannot account for the observed redshift evolution in spin temperatures.

Key words: quasars: absorption lines – galaxies: high-redshift – ISM: evolution – radio lines: ISM

* E-mail: nkanekar@ncra.tifr.res.in (NK); Ramanujan Fellow.

1 INTRODUCTION

Quasar absorption spectra offer the possibility of selecting galaxies by their absorption signatures, and thus obtaining samples of high- z galaxies without a bias towards the most luminous systems. The highest HI column density absorbers detected in quasar spectra are the damped Lyman- α systems (DLAs). With HI column densities $N_{\text{HI}} \geq 2 \times 10^{20} \text{ cm}^{-2}$ (Wolfe et al. 2005), similar to values seen in sightlines through the Milky Way and nearby gas-rich galaxies, DLAs have long been identified as the high-redshift counterparts of normal galaxies in the local Universe. The nature of galaxies that give rise to DLAs at different redshifts, and their typical size, mass, kinematic structure and physical conditions, are all important ingredients for understanding galaxy evolution.

The Sloan Digital Sky Survey (SDSS; Abazajian et al. 2009) has resulted in the detection of a vast number of DLAs at high redshifts, with nearly seven thousand candidate absorbers now known at $z > 2.2$ (e.g. Prochaska et al. 2005; Prochaska & Wolfe 2009; Noterdaeme et al. 2009; Noterdaeme et al. 2012). Unfortunately, contamination from the background quasars has made it very difficult to identify the host galaxy of the DLAs in optical images (e.g. Warren et al. 2001; but see Fumagalli et al. 2010). The low sensitivity of today's radio telescopes has meant that one cannot image the DLA hosts in the standard radio HI 21cm and CO emission lines that have been used for detailed studies of the kinematics and dynamics of nearby galaxies. And, even following a number of recent studies, only a handful of high- z DLAs have been detected in H α or Ly α emission (e.g. Møller et al. 2004; Fynbo et al. 2010, 2011; Péroux et al. 2012; Noterdaeme et al. 2012), with typical star formation rates (SFRs) $\lesssim \text{few } M_{\odot}$ per year (Péroux et al. 2012), even for high-metallicity absorbers. Thus, despite much effort over the last three decades, relatively little information has so far been gleaned from emission studies of DLAs.

Detailed absorption studies remain our primary source of information about the absorbers. Around two hundred DLAs have measured metallicities, elemental abundances and kinematics, from high-resolution optical echelle spectroscopy (e.g. Pettini et al. 1994, 1997, 1999, 2008; Prochaska et al. 2003; Prochaska et al. 2007; Dessauges-Zavadsky et al. 2004; Khare et al. 2004; Ledoux et al. 2006; Petitjean et al. 2008; Penprase et al. 2010; Cooke et al. 2011; Battisti et al. 2012). These studies have yielded interesting results. For example, mean DLA metallicities have been shown to increase with decreasing redshift, as expected from models of galaxy evolution, although low-metallicity DLAs are quite common even at low redshifts (Prochaska et al. 2003; Kulkarni et al. 2005, 2010; Rafelski et al. 2012). A positive correlation has been found between the metallicity and both the velocity spreads of low-ionization metal lines (Wolfe & Prochaska 1998; Ledoux et al. 2006), and the rest equivalent width of the SiII λ 1526 line (Prochaska et al. 2008). This has been interpreted as evidence for a mass-metallicity relation in DLAs, similar to that seen in emission-selected high- z galaxies (e.g. Tremonti et al. 2004; Savaglio et al. 2005; Erb et al. 2006; Neeleman et al. 2013). Molecular hydrogen (H $_2$) absorption, along with CI absorption, has been detected in about a dozen DLAs, with strong upper limits on the molecular fraction in $\sim 80\%$ of the observed systems (e.g. Levshakov & Varshalovich 1985; Ge & Bechtold 1997; Ge et al. 2001; Ledoux et al. 2003; Noterdaeme et al. 2008; Milutinovic et al. 2010; Jorgenson et al. 2010). This has provided information on local conditions in the molecular phase, including estimates of the number density, temperature and strength of the ultraviolet (UV) radiation

field (e.g. Srianand et al. 2005), along with measurements of the microwave background temperature at different redshifts (e.g. Noterdaeme et al. 2011).

While absorption spectra have yielded many successes in DLA studies, the fact that they only trace a pencil beam through each galaxy implies that many of the major questions in the field remain to be answered. For example, the asymmetric wings seen in low-ionization metal line profiles were originally thought to imply an origin in rapidly-rotating thick disks (Prochaska & Wolfe 1997), but have also been shown to arise naturally in hierarchical merging scenarios (Haehnelt et al. 1998; but see Prochaska & Wolfe 2010), dwarf galaxy ejecta (Nulsen et al. 1998), and outflows from starburst galaxies (Schaye 2001). The star formation histories of $z > 2$ DLAs, deduced from their elemental abundances, indicate an unambiguous origin in dwarf irregular galaxies for a few DLAs (Dessauges-Zavadsky et al. 2006), but also suggest that all the absorbers do not arise in a single galaxy class (Dessauges-Zavadsky et al. 2007). On the other hand, the large velocity spreads seen in a number of DLAs and the curious paucity of systems with narrow velocity spreads ($\Delta v \lesssim 30 \text{ km s}^{-1}$) are difficult to reconcile with an origin in dwarf galaxies (e.g. Prochaska & Wolfe 1997; Wolfe et al. 2005). The complications of interpreting absorption spectra have meant that even basic questions pertaining to the typical size and structure of DLAs, and their redshift evolution, remain issues of controversy.

HI 21cm emission studies of high redshift DLAs are currently not possible owing to the weakness of the HI 21cm line and the low sensitivity of today's radio telescopes; the highest redshift at which HI 21cm emission has been detected is $z \approx 0.26$ (Catinella et al. 2008). However, HI 21cm absorption studies of DLAs lying towards radio-loud quasars provide an important tool both to study physical conditions in the neutral gas in the absorbers and to probe fundamental constant evolution. For DLAs lying towards extended background radio sources, HI 21cm absorption studies provide a measure of the spatial extent of the neutral gas as well as the opacity-weighted velocity field, although such studies have only so far been possible in a couple of DLAs (e.g. Briggs et al. 1989; Kanekar & Briggs 2004). Conversely, for DLAs towards compact radio sources, a comparison between the HI column density measured from the Lyman- α absorption profile and the integrated HI 21cm optical depth yields the spin temperature T_s of the absorbing gas. In addition, for compact targets, comparisons between the redshifts of HI 21cm absorption lines with those of other transitions (e.g. resonant UV lines, OH Lambda-doubled lines, rotational lines; Wolfe et al. 1976; Drinkwater et al. 1998; Chengalur & Kanekar 2003) can be used to test for changes in the fundamental constants of physics.

The spin temperature contains information on the distribution of neutral gas between the different temperature phases of the interstellar medium (ISM) in the absorber, specifically on the fractions of warm and cold gas. The fact that the spin temperature appeared systematically higher in high- z DLAs than in the Galaxy has made T_s a quantity of interest in DLA studies for the last three decades (e.g. Wolfe & Davis 1979; Wolfe et al. 1981). However, until the recent advent of new radio telescopes like the Giant Metrewave Radio Telescope (GMRT) and the Green Bank Telescope (GBT) with excellent low frequency coverage, only a few T_s estimates were available in high- z DLAs (e.g. Wolfe & Davis 1979; Wolfe et al. 1985; de Bruyn et al. 1996; Carilli et al. 1996; Briggs et al. 1997; Kanekar & Chengalur 1997). Over the last decade, we have used the GBT, the GMRT and the Westerbork Synthesis Radio Telescope (WSRT) to carry out sensitive searches for redshifted HI 21cm ab-

sorption in a large sample of DLAs at high redshifts, $z \gtrsim 2$. We have also used the Very Long Baseline Array (VLBA) to measure the low-frequency core fractions of the background quasars for most of the absorbers of the sample. Finally, we have obtained the metallicity, dust depletion and kinematic structure in the low ionization metal lines for a significant fraction of the DLAs in our sample, either from our own observations or from the literature. In this paper, we report results from these studies and their implications for physical conditions in the neutral gas.¹

2 OBSERVATIONS, DATA ANALYSIS AND SPECTRA

2.1 HI 21cm absorption line searches

Our searches for redshifted HI 21cm absorption were carried out with the GMRT, the GBT and the WSRT, targeting 26 DLAs at $0.68 < z < 3.42$. In addition, two known HI 21cm absorbers were re-observed, to confirm earlier detections. The new targets were selected from the literature, mostly from the CORALS sample of Ellison et al. (2001), the UCSD sample of Jorgenson et al. (2006) and the SDSS. Five targets were observed with the GMRT, 22 with the GBT, and one with the WSRT, all between 2003 and 2009.

2.1.1 GBT observations and data analysis

The GBT observations were carried out with the PF1-800, PF1-450 and PF1-342 receivers, in projects AGBT03A-015, AGBT05B-018, AGBT06B-042, AGBT08A-076 and AGBT09A-025. Most observations used the Spectral Processor (SP) as the backend, with two linear polarizations and bandwidths of 1.25, 2.5 or 5 MHz, sub-divided into 1024 channels. The SP was not available for the observations of two sources, 1122–168 and 0454+039; these were hence observed with the Auto-Correlation Spectrometer (ACS), using two circular polarizations, a bandwidth of 50 MHz sub-divided into 16384 channels, and nine-level sampling. All observations used position-switching for bandpass calibration, with On and Off times of 5m each, and data recorded every 5 or 10 seconds. A switching noise diode was used to measure system temperatures during all observations. Most runs also included observations of standard flux density calibrators like 3C286 or 3C48 to check the flux scale.

All GBT data were analysed in the AIPS++ single-dish package DISH, using standard procedures. All data were first visually inspected, both before and after calibration, and individual records affected by either radio frequency interference (RFI) or backend failures were edited out. For each target, the data were calibrated and the quasar flux density was measured in the centre of the band from the averaged spectrum. Some of the observations were affected by severe out-of-band RFI (although the receiver did not saturate), and the flux densities were found to vary dramatically from one record to another, typically yielding average flux densities very different from those in the literature and often also differing values in the two polarizations. In such cases, we chose to use flux densities from the literature, interpolating between measurements to obtain values at the respective redshifted HI 21cm line frequencies. In general, the measured system temperatures (T_{sys}) were found to match expected values (except in cases where the

data were rendered unusable by extremely strong RFI) and the root-mean-square (RMS) noise values on the spectra were close to the expected values, based on the T_{sys} estimates. After the flux density measurements, a second-order baseline was fitted to line- and RFI-free channels in each record during the process of calibration and the residual spectra were averaged together to obtain the HI 21cm spectrum for each source. In some cases, a further first- or second-order baseline was fit to the spectrum, again excluding line- and RFI channels, to obtain the final HI 21cm spectrum for each DLA. Finally, data on eight targets were rendered unusable by strong RFI at or near the redshifted HI 21cm line frequencies.

2.1.2 GMRT and WSRT observations, and data analysis

The GMRT observations used the 327-MHz receivers and the 30-antenna hardware correlator, with two polarizations and a bandwidth of 1 MHz sub-divided into 128 channels, or 2 MHz sub-divided into 256 channels. The number of working antennas varied between 22 and 30 on the different runs, due to maintenance activities and technical problems. Observations of the standard calibrators 3C48, 3C147 and 3C286 were used to test the system performance at the beginning of each observing run, and then to calibrate the flux density scale. An observing run typically consisted of a full-synthesis track on the target source, interleaving 40-minute scans on the target with 7-minute scans on compact phase calibrators to calibrate the antenna gains. The system passband was calibrated with observations of bright radio sources, usually the flux density calibrators themselves, approximately every 3 hours.

The WSRT observations of 0528–250 used the 92cm receivers, with two DZB/IVC sub-bands of bandwidth 1.25 MHz each sub-divided into 512 channels, with two polarizations. The two intermediate-frequency DZB/IVC sub-bands were used in order to reduce the digital noise. The standard calibrators 3C48 and 3C286 were observed at the start and end of each run to calibrate the flux density scale and the system bandpass. A total of 50 hours of observing time were obtained on the target source.

All GMRT and WSRT data were analysed in “classic” AIPS, following standard procedures. After initial editing of bad data (e.g. due to malfunctioning antennas, shadowing, correlator problems, RFI, etc), the antenna gains, passband shapes and amplitude scales were determined, using the data on the various calibrators. After applying the initial calibration, a number of channels were averaged together to obtain a “channel-0” continuum visibility dataset and a series of self-calibration and imaging cycles were then used to accurately determine the antenna gains. This was accompanied with intermediate flagging steps to further edit out bad data. For the GMRT, 3-D imaging procedures were used for all 327 MHz data, with the field sub-divided into 37 facets during imaging. In the case of the WSRT, the low source elevation meant that additional care had to be taken to remove data affected by shadowing by foreground trees. The self-calibration and imaging procedure consisted of 3-4 phase-only calibration and imaging cycles, followed by a single amplitude-and-phase self-calibration and imaging step. This was followed by subtraction of the image from the calibrated visibilities, with the residual U-V data then examined for any systematic behaviour and bad data edited out, after which the self-calibration and imaging cycles were repeated. This procedure was carried out for each source until no further improvement was obtained in the image and U-V residuals, typically after 2-3 such cycles. The final image was then subtracted out from the calibrated multi-channel U-V visibility dataset, using the task UVSUB. Following this, the task UVLIN was used to subtract out any residual

¹ When required, we will use the standard Λ -CDM cosmology, with $H_0 = 67.4 \text{ km s}^{-1} \text{ Mpc}^{-1}$, $\Omega_m = 0.315$ and $\Omega_\Lambda = 0.685$ (Planck Collaboration 2013).

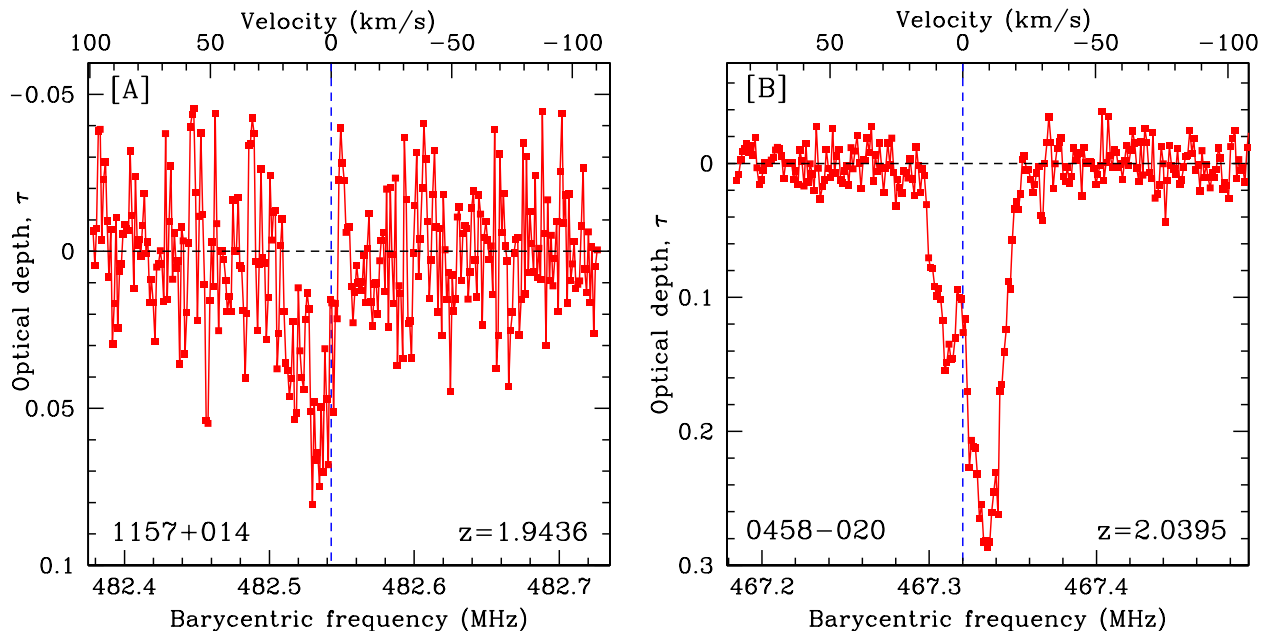


Figure 1. Detections of HI 21cm absorption in two known HI 21cm absorbers, [A] at $z = 1.9436$ towards 1157+014 and [B] $z = 2.0395$ towards 0458-020, with HI 21cm optical depth plotted against barycentric frequency, in MHz. The top axis in each panel shows velocity (in km s^{-1}), relative to the DLA redshift. See main text for discussion.

emission, by a first-order polynomial fit to the spectrum on each visibility baseline. The residual U-V data were then shifted to the heliocentric frame using the task `CVEL`, and were imaged to produce the final spectral cube. A spectrum was then obtained by taking a cut through the location of the target source. In some cases, a second-order baseline was fit to this spectrum to obtain the final HI 21cm spectrum of the source. Finally, the source flux density was measured by using the task `JMFIT` to fit a gaussian model to the final continuum image; all target sources were unresolved by the WSRT and GMRT synthesized beams and a single gaussian was hence used as the model in all cases.

In the case of the WSRT data, the extremely low elevation of 0528-250 meant that the flux density scale could not be determined accurately. We found that both the source flux density and the RMS noise on the spectrum were lower by a factor of ≈ 1.71 than the expected values, indicating a multiplicative problem with the flux scale. Fortunately, this scaling issue does not affect the HI 21cm optical depth spectrum. Note that the quoted flux density and RMS noise values in Table 1 have been corrected by this factor of 1.71, for consistency with the literature.

2.1.3 Spectra and results

New detections of HI 21cm absorption were obtained in two DLAs, at $z \sim 3.387$ towards 0201+113 and $z \sim 2.347$ towards 0438-436. These results were discussed in detail by Kanekar et al. (2006) and Kanekar et al. (2007), and the spectra are not shown here. HI 21cm absorption was also detected in two known HI 21cm absorbers, at $z \sim 1.9436$ towards 1157+014 (Wolfe et al. 1981) and $z = 2.0395$ towards 0458-020 (Wolfe et al. 1985); these spectra are shown in Fig. 1. For the non-detections, the final HI 21cm spectra are shown in Figure 2, in order of increasing right ascension.

The observational details and results of the GBT, GMRT and WSRT spectroscopy are summarized in Table 1. The columns of this table are: (1) the quasar name, (2) the quasar emission red-

shift, (3) the DLA redshift, (4) the redshifted HI 21cm line frequency, (5) the telescope used for the HI 21cm search, (6) the on-source integration time, in hours, (7) the bandwidth, in MHz, (8) the velocity resolution, in km s^{-1} , after Hanning-smoothing and re-sampling, (9) the RMS noise at this velocity resolution, in mJy, (10) the source flux density, in Jy, (11) for detections, the integrated HI 21cm optical depth $\int \tau_{21\text{cm}} dV$, or, for non-detections, the 3σ limit on $\int \tau_{21\text{cm}} dV$, assuming a gaussian line profile with a line FWHM of $\Delta V = 15 \text{ km s}^{-1}$, with the RMS noise computed at a similar velocity resolution. For the eight GBT targets where the final HI 21cm spectrum was unusable due to RFI, column (10) contains “RFI”, and the remaining column entries have been left blank. We note, in passing, that the assumed line FWHM of 15 km s^{-1} is comparable to the widths of spectral components in known redshifted HI 21cm absorbers; assuming a narrower line FWHM would yield a more stringent lower limit on the spin temperature (see Section 3 for discussion).

2.2 VLBA imaging studies

We used the VLBA 327 MHz, 606 MHz and 1.4 GHz receivers in proposals BK89, BK131, BK153, BK159 and BK175 to obtain high spatial resolution images of the compact radio structure of the quasars behind a sample of DLAs and HI 21cm absorbers, to measure the quasar core fractions, and thus estimate the DLA covering factors. For each target, the VLBA observing frequency was chosen to be within a factor of ≈ 2 of the redshifted HI 21cm line frequency, to ensure that the spatial extent of the background radio continuum was determined close to the line frequency. In practice, the VLBA observing frequency was within a factor of 1.5 of the redshifted HI 21cm line frequency for all targets except for three HI 21cm absorbers at $z \sim 1.3$ lying towards faint background quasars (J0850+5159, J0852+3435 and 2337-011, all with flux densities $\lesssim 100 \text{ mJy}$ at the redshifted HI 21cm line frequency). These three

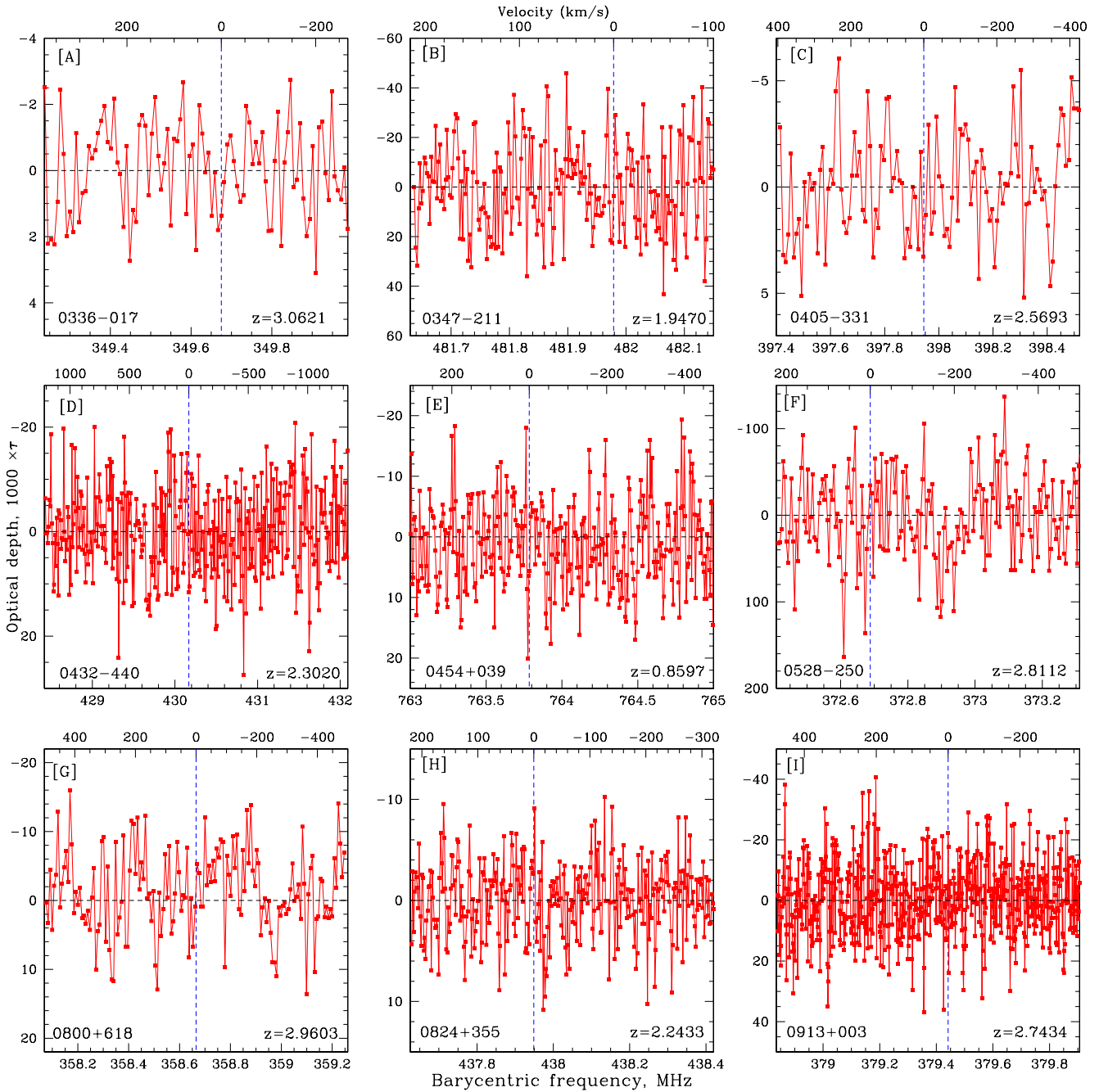


Figure 2. The sixteen non-detections of HI 21cm absorption, in order of increasing right ascension, with optical depth ($10^3 \times \tau$) plotted against barycentric frequency, in MHz. The top axis in each panel shows velocity (in km s^{-1}), relative to the DLA redshift, while the expected HI 21cm line frequency, from the optically-determined redshift, is indicated by the dashed line in each panel. The panels contain spectra for [A] the $z = 3.0621$ DLA towards 0336–017, [B] the $z = 1.9470$ DLA towards 0347–211, [C] the $z = 2.5693$ DLA towards 0405–311, [D] the $z = 2.3020$ DLA towards 0432–440, [E] the $z = 0.8597$ DLA towards 0454+039, [F] the $z = 2.8112$ DLA towards 0528–250, [G] the $z = 2.9603$ DLA towards 0800+618, [H] the $z = 2.2433$ DLA towards 0824+355, [I] the $z = 2.7434$ DLA towards 0913+003, [J] the $z = 2.7670$ DLA towards 1013+615, [K] the $z = 0.6819$ DLA towards 1122–168, and [L] the $z = 2.7799$ DLA towards 1354–170. [M] The $z = 2.7076$ DLA towards 1402+044, [N] the $z = 3.4483$ DLA towards 1418–064, [O] the $z = 2.5200$ DLA towards 1614+051, and [P] the $z = 2.9082$ DLA towards 2342+342. The dashed vertical line marks the expected redshifted HI 21cm frequency. The shaded vertical region in panel [L] (for 1354–170) indicates a frequency range affected by RFI.

sources were observed with the higher-sensitivity L-band receivers of the VLBA.

The results from the initial VLBA data of proposals BK89 and BK131 were presented by Kanekar et al. (2009a). We will not describe these data again here, but will instead simply use the core

flux density estimates from that paper. 13 DLAs and HI 21cm absorbers were observed with the VLBA in proposals BK153, BK159 and BK175, six with the 327 MHz receivers, three with the 606 MHz receivers and four with the 1.4 GHz receivers. Bandwidths of 12, 4 and 32 MHz were used at 327 MHz, 606 MHz and

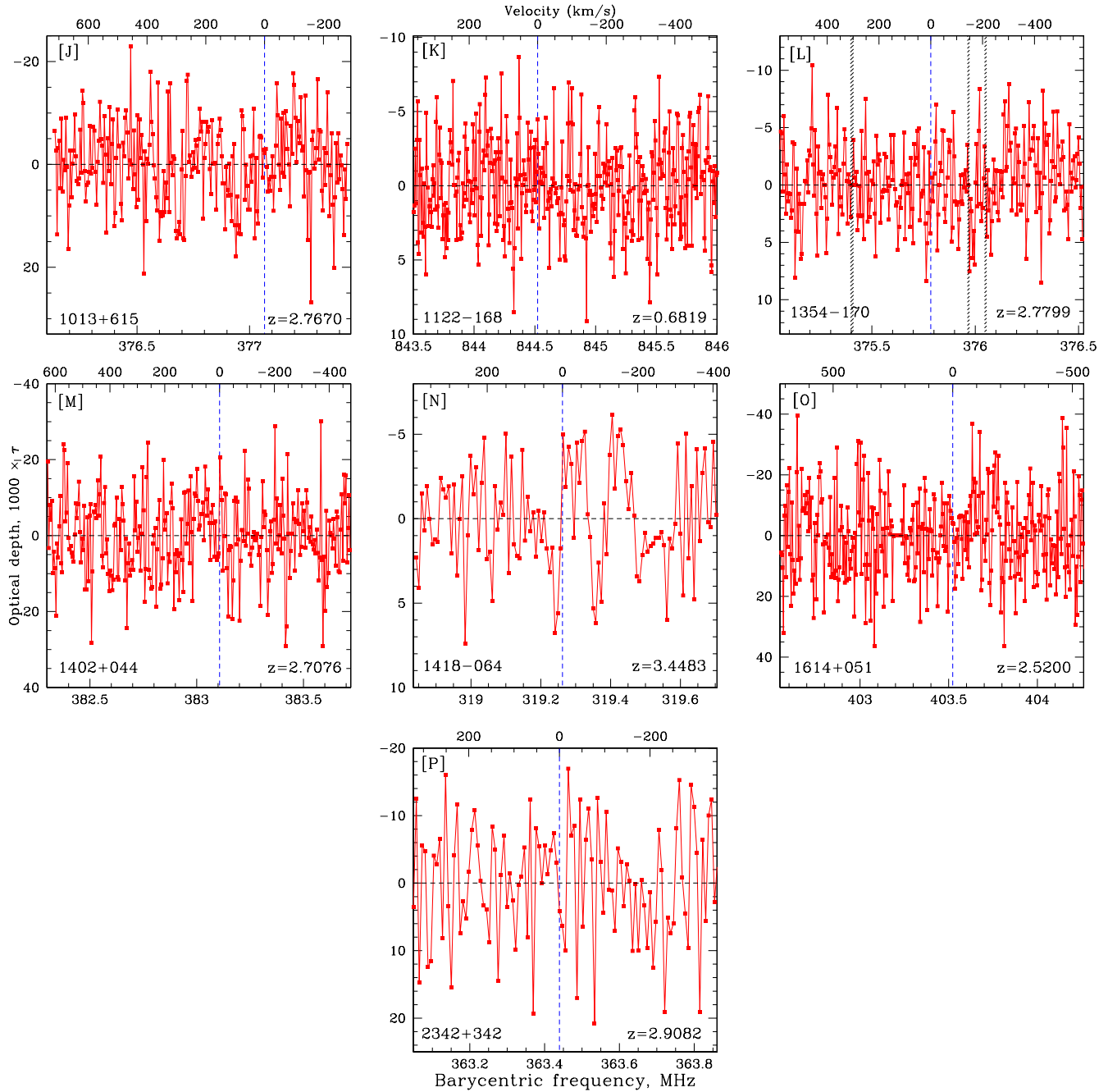


Figure 2. (contd.)

1.4 GHz, respectively, sub-divided into 32 spectral channels and with two polarizations and two-bit sampling. The on-source time was ≈ 2 hours for each source. One or more of the strong fringe finders 0438–436, 3C454.3, 3C84, 3C147, 3C286 and 3C345 were observed during each run for bandpass calibration; phase referencing was not used.

The VLBA data were also reduced in “classic” AIPS, following procedures similar to those described in section 2.1.2. However, for the VLBA data, the flux density scale was calibrated by using online measurements of the antenna gains and system temperatures, and the calibration steps included ionospheric corrections and fringe-fitting to determine the delay rates. Unfortunately, the ionospheric phase stability was relatively poor during the 327 MHz

and 606 MHz observations and only 5–6 antennas could be retained during the self-calibration procedure. Further, the final VLBA images were produced with phase self-calibration alone, again after the usual iterative procedure involving a number of self-calibration and imaging cycles. The core flux density of each source was measured using the task JMFIT, by fitting an elliptical gaussian model to the core radio emission. The core emission was found to be fairly compact in most cases, with little extended emission; a single gaussian was hence used as the model for most sources. For three sources, adding more source components yielded a clear decrease in the χ^2 and thus an appreciably better fit: a two-component model was hence used for two of these, 2003–025 and 1122–168, and a three-component model for 0824+355.

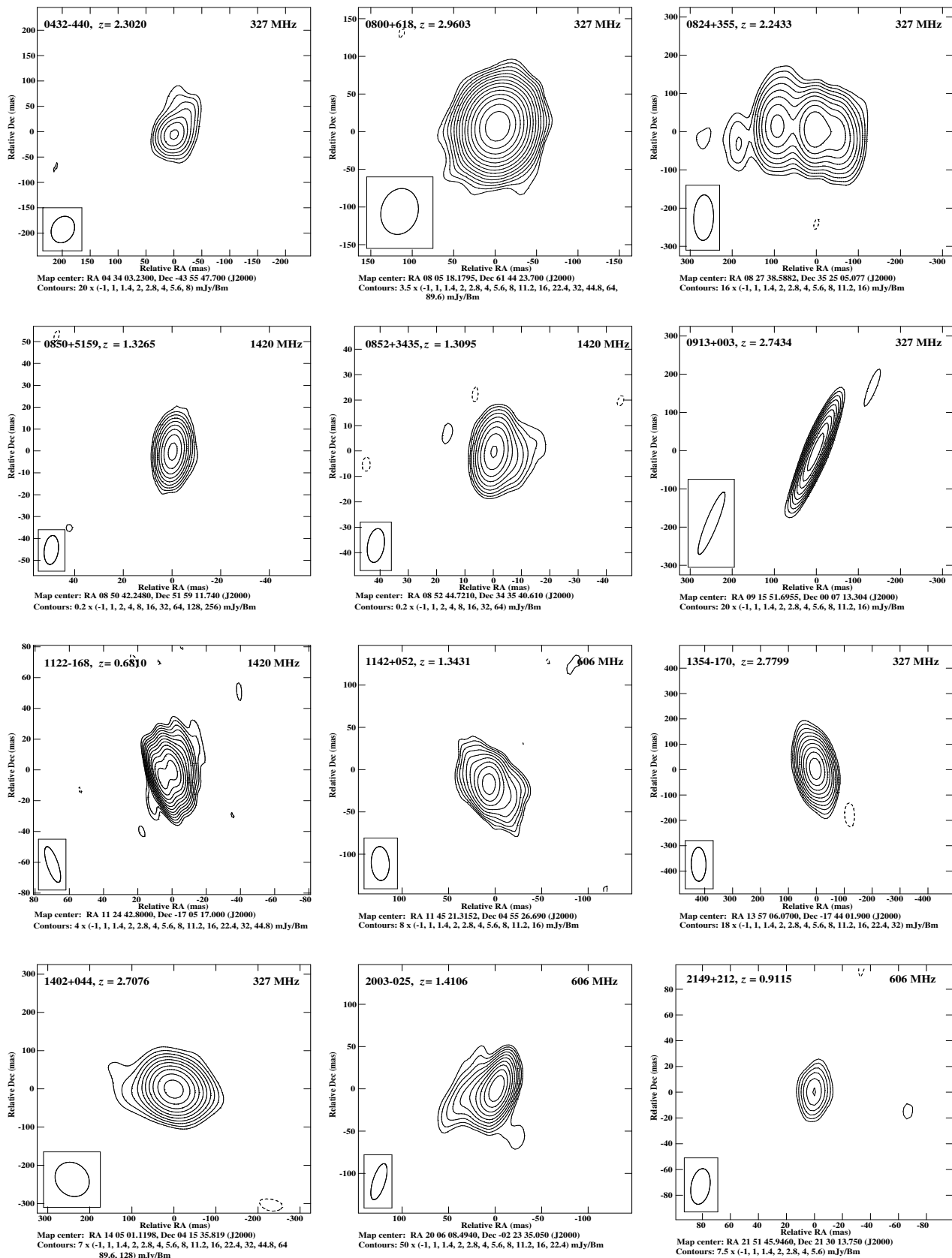


Figure 3. VLBA images of the compact radio structure of the 13 background quasars; the quasar name, DLA redshift and observing frequency are indicated at the top of each panel. The dashed contour is the largest negative value in each image, with the outermost positive contour at the same level; the penultimate solid contour thus indicates the lowest believable structure in each image. The synthesized beam is shown at the bottom left corner of each panel.

Table 1. Summary of HI 21cm observations.

QSO	z_{QSO}	z_{DLA}	$\nu_{21\text{cm}}$ MHz	Telescope	Time hours	BW MHz	Resn. km s^{-1}	RMS mJy	$S_{21\text{cm}}^d$ Jy	$\int \tau_{21} dV$ km s^{-1}
0149+335	2.431	2.1408	452.24	GBT	2	2.5	3.2	RFI	–	–
0201+113	3.610	3.3869	323.78	GMRT	20	1.0	7.2	1.0	0.42	0.714 ± 0.017
0336–017	3.200	3.0621	349.67	GMRT	11	1.0	6.7	1.1	0.83	< 0.07
0347–211	2.944	1.9470	481.98	GBT	2	1.25	1.5	16.8	0.94	< 0.29
0405–331	2.570	2.5693	397.95	GBT	6	5,1.25	1.8,7.4	2.5 ^a	1.0	< 0.12
0432–440	2.649	2.3020	430.17	GBT	0.5	5.0	6.8	5.6	0.61	< 0.22
0438–436	2.863	2.3474	424.33	GBT	1.5	1.25	1.7	10.4	7.1	0.216 ± 0.027
0405–443	3.020	1.9130	487.61	GBT	0.2	1.25	1.5	RFI	–	–
0454+039	1.350	0.8597	763.78	GBT	0.5	50	2.4	3.2	0.46	< 0.15
0458–020	2.229	2.0395	467.32	GBT	1	0.625,1.25	0.78,1.6	16.2	1.5	5.866 ± 0.059^b
0528–250	2.779	2.8112	372.69	WSRT	50	1.25	3.9	7.0 ^c	0.140 ^c	< 1.3
0800+618	3.033	2.9603	358.66	GMRT	5	2.0	6.5	4.0	0.70	< 0.19
0824+355	2.249	2.2433	437.95	GBT	2	1.25	1.7	9.6	2.6	< 0.068
0913+003	3.074	2.7434	379.44	GBT	1	12.5	1.2	10.2	0.84	< 0.18
0944+636	2.617	2.4960	406.29	GBT	2	2.5	3.6	RFI	–	–
1013+615	2.800	2.7670	377.07	GBT	4	2.5	3.9	8.1	1.00	< 0.20
1122–168	2.397	0.6819	844.52	GBT	1.5	50.0	2.2	1.7	0.58	< 0.059
1157+014	2.000	1.9436	482.47	GBT	2	0.625	0.76	14.2	0.70	1.020 ± 0.091
1215+333	2.610	1.9991	473.61	GBT	0.2	1.25	1.6	RFI	–	–
1230–101	2.394	1.9314	484.55	GBT	1	1.25	1.5	RFI	–	–
1354–170	3.150	2.7799	375.78	GBT	2.5	2.5	3.9	8.7	2.6	< 0.10
1402+044	3.215	2.7076	383.11	GBT	1.5	2.5	3.8	11.5	1.1	< 0.21
1418–064	3.689	3.4483	319.31	GMRT	11	1.0	7.3	1.3	0.44	< 0.10
1614+051	3.215	2.5200	403.52	GBT	3	2.5	3.6	16	1.1	< 0.30
1645+635	2.380	2.1253	454.49	GBT	0.5	1.25	1.6	RFI	–	–
1755+578	2.110	1.9698	478.28	GBT	1	1.25	1.5	RFI	–	–
1850+402	2.120	1.9888	475.24	GBT	1	1.25	1.5	RFI	–	–
2342+342	3.053	2.9082	363.44	GMRT	10	1.0	6.4	1.4	0.29	< 0.22

^aThe quoted RMS noise is on the final HI 21cm spectrum, produced by smoothing the two spectra to the same velocity resolution and then averaging with weights based on the RMS noise values.

^bThe quoted integrated HI 21cm optical depth for the $z = 2.0395$ DLA towards 0458–020 is the average of the values obtained in the two observing runs in March and May 2008, while the RMS noise is at a resolution of 2.4 kHz, averaging over the two runs. See Section 5 for details.

^cThe low elevation of 0528–250 during the WSRT observations resulted in a multiplicative error by a factor of 1.71 in the flux density scale. The measured flux density and RMS noise were 82 mJy and 4.1 mJy, respectively; however, the quoted values in the table are on the flux scale of Carilli et al. (1996). Note that the flux scale has no effect on the inferred optical depth.

^d $S_{21\text{cm}}$ is the source flux density at the redshifted HI 21cm line frequency.

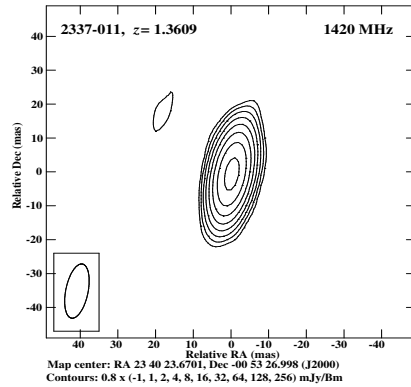
**Figure 3.** (contd.)

Table 2. Results from VLBA low-frequency imaging of quasars behind high- z DLAs.

QSO	z_{QSO}	z_{abs}	$\nu_{21\text{cm}}$ MHz	ν_{VLBA} MHz	S_{tot}^a Jy	Beam mas \times mas	S_{fit} Jy	Angular size mas \times mas	Spatial extent pc \times pc	f^c
0432–440	2.649	2.3020	430.17	327	0.69	54×40	0.26	$58.2^{+2.5}_{-2.5} \times 24.4^{+2.1}_{-2.3}$	$490^{+21}_{-21} \times 205^{+18}_{-19}$	0.38
0800+618	3.033	2.9603	358.66	327	0.70	61×45	0.44	$13.5^{+0.8}_{-0.8} \times 10.3^{+0.6}_{-0.8}$	$107^{+6}_{-6} \times 82^{+5}_{-6}$	0.63
0824+355	2.249	2.2433	437.95	327	2.00	119×47	0.40	$27.8^{+6.2}_{-27.8} \times 2.4^{+0.8}_{-2.4}$	$235^{+52}_{-235} \times 20^{+7}_{-20}$	0.20
							0.37	$66.2^{+9.2}_{-9.6} \times 41.1^{+9.9}_{-15.6}$	$560^{+78}_{-81} \times 348^{+84}_{-132}$	–
							0.36	$79.2^{+9.4}_{-9.7} \times 51.7^{+3.4}_{-5.1}$	$670^{+79}_{-82} \times 437^{+29}_{-43}$	–
J0850+5159	1.894	1.3265	610.53	1420	0.061	13.3×5.8	0.069	$1.49^{+0.04}_{-0.03} \times 0.95^{+0.17}_{-0.21}$	$12.9^{+0.3}_{-0.3} \times 8.0^{+1.5}_{-1.8}$	1.0
J0852+3435	1.655	1.3095	615.03	1420	0.066	13.4×5.9	0.062	$2.9^{+0.03}_{-0.03} \times 0.89^{+0.25}_{-0.35}$	$25.0^{+0.3}_{-0.3} \times 7.7^{+2.2}_{-3.0}$	0.93
0913+003	3.074	2.7434	379.44	327	0.48	173×27	0.26	$16.6^{+17.4}_{-9.3} \times 7.6^{+2.2}_{-7.6}$	$134^{+141}_{-75} \times 62^{+18}_{-62}$	0.54
1122–168	2.397	0.6819	844.52	1420	0.29	24.1×6.5	0.012	$4.2^{+1.5}_{-2.4} \times 0.0^{+0.0}_{-0.0}$	$30.7^{+11.0}_{-17.5} \times 0.0^{+0.0}_{-0.0}$	0.04
							0.043	$12.5^{+0.4}_{-0.3} \times 5.7^{+0.9}_{-1.0}$	$91.3^{+2.9}_{-2.2} \times 41.6^{+6.6}_{-7.3}$	–
1142+052	1.345	1.3431	606.21	606	1.01	40×19	0.30	$36.6^{+1.6}_{-1.6} \times 19.1^{+1.8}_{-2.1}$	$317^{+14}_{-14} \times 165^{+16}_{-18}$	0.30
1354–170	3.150	2.7799	375.78	327	0.83	134×53	0.81	$88.3^{+1.8}_{-1.8} \times 38.6^{+2.0}_{-2.1}$	$712^{+15}_{-15} \times 311^{+16}_{-17}$	0.97
1402+044	3.215	2.7076	383.11	327	1.26	93×78	0.43	$44.5^{+6.5}_{-7.3} \times 23.4^{+10.6}_{-23.4}$	$362^{+53}_{-59} \times 190^{+86}_{-190}$	0.34
2003–025	1.457	1.4106	589.23	606	3.7	44×13	1.97	$14.9^{+0.6}_{-0.5} \times 11.0^{+1.1}_{-1.3}$	$129^{+5}_{-4} \times 95^{+10}_{-11}$	0.53
							1.48	$48.5^{+2.1}_{-2.1} \times 31.2^{+3.2}_{-3.4}$	$421^{+18}_{-18} \times 271^{+28}_{-30}$	–
2149+212	1.538	0.9115	743.08	606	1.92	28×13	0.05	$13.3^{+4.2}_{-13.3} \times 7.1^{+5.5}_{-7.1}$	$107^{+34}_{-107} \times 57^{+44}_{-57}$	0.03
2337–011	2.085	1.3606	601.71	1420	0.12	16.2×5.9	0.13	$1.5^{+0.2}_{-0.3} \times 0.60^{+0.19}_{-0.60}$	$13.0^{+1.7}_{-2.6} \times 5.2^{+1.6}_{-5.2}$	1.0

^aThe total flux density S_{tot} at the VLBA observing frequency was estimated by extrapolating from measured values in the literature, usually from the 365 MHz Texas survey (Douglas et al. 1996) and the 1.4 GHz Very Large Array FIRST and NVSS surveys (Becker et al. 1995; Condon et al. 1998).

^bFor 1122–168, the deconvolved angular size and spatial extent are both 0.0 along one axis. This is because the angular extent of the core along this axis is significantly smaller than the VLBA synthesized beam.

^cWe assume that the DLA covering factor f is equal to the quasar core fraction, i.e. the ratio of the core flux density to the total integrated flux density, S_{tot} . For the three sources, 1122–168, 0824+355 and 2003–025, where the model contained multiple Gaussian components, the more compact component has been identified with the core. In such cases, the covering factor estimates assume that only the core has been covered by the foreground DLA.

The VLBA images are presented in Figure 3, in order of increasing right ascension, with the results summarized in Table 2. The columns of this table contain: (1) the quasar name, (2) the quasar emission redshift, (3) the DLA redshift, (4) the redshifted HI 21cm line frequency, in MHz, (5) the VLBA observing frequency ν_{VLBA} , in MHz, (6) the total source flux density S_{tot} at the VLBA observing frequency, obtained from single-dish or low-resolution interferometer studies, (7) the VLBA beam, in mas \times mas, (8) the core flux density S_{VLBA} , in Jy, measured from the VLBA image (for the three sources with multiple gaussian components, the most compact component was identified as the core), (9) the deconvolved size of the radio emission, in mas \times mas, (10) the spatial extent of the core radio emission at the DLA redshift, and (11) the DLA covering factor f , assumed to be equal to the quasar core fraction, i.e. the ratio of the core flux density measured in the VLBA image S_{VLBA} to the total source flux density S_{tot} at the VLBA frequency (see Section 3). For systems without measurements of the total flux density at the VLBA observing frequency, S_{tot} was estimated by

extrapolating from measurements at other frequencies. It should be emphasized that the estimates of the deconvolved size of the core emission and its spatial extent are upper limits, because any residual phase errors would increase the apparent size of the core emission. Finally, we note that error bars have not been included on the covering factor estimates. While we estimate that the errors on the VLBA flux density calibration are $\approx 10\%$, the VLBA and total flux density measurements were not carried out simultaneously, implying that individual covering factor estimates could have larger errors due to source variability.

2.3 Optical spectroscopy

2.3.1 VLT-UVES spectroscopy

Very Large Telescope Ultraviolet Echelle Spectrograph (VLT-UVES) data were obtained as part of the programme 67.A-0567(A) (PI: Lane) for 1127–145 in May/June 2001. Five 3060-second ex-

Table 3. Ionic column densities

Ion	λ (Å)	$\log f$	$\log[N_0/\text{cm}^{-2}]^b$	$\log[N/\text{cm}^{-2}]^b$
(1) 0738+313, $z = 0.0912$, HIRES, $\log[N_{\text{HI}}/\text{cm}^{-2}] = 21.18 \pm 0.06$				
MgI	2852.964	0.2577	> 12.98	> 12.98
CaII	3934.777	-0.1871	12.28 ± 0.03	12.26 ± 0.03
	3969.591	-0.4921	12.18 ± 0.08	
TiII	3230.131	-1.1630	< 12.74	12.51 ± 0.04
	3384.740	-0.4461	12.51 ± 0.04	
(2) 0738+313, $z = 0.2212$, HIRES, $\log[N_{\text{HI}}/\text{cm}^{-2}] = 20.90 \pm 0.07$				
MgI	2852.964	0.2577	> 12.46	> 12.46
MgII	2796.352	-0.2130	> 13.49	> 13.75
	2803.531	-0.5151	> 13.75	
CaII	3934.777	-0.1871	11.86 ± 0.07	11.92 ± 0.06
	3969.591	-0.4921	12.12 ± 0.09	
TiII	3230.131	-1.1630	< 12.58	< 11.91
	3384.740	-0.4461	< 11.91	
FeII	2586.650	-1.1605	> 14.30	> 14.30
	2600.173	-0.6216	> 13.82	
(3) 0952+179, $z = 0.2378$, UVES, $\log[N_{\text{HI}}/\text{cm}^{-2}] = 21.32 \pm 0.05$				
MgI	2852.964	0.2577	12.68 ± 0.03	12.68 ± 0.03
MgII	2796.352	-0.2130	> 13.87	> 14.13
	2803.531	-0.5151	> 14.13	
TiII	3073.877	-0.9622	12.62 ± 0.03	12.62 ± 0.03
	3230.131	-1.1630	< 12.58	< 11.91
MnII	2576.877	-0.4549	12.50 ± 0.03	12.58 ± 0.03
	2594.499	-0.5670	12.67 ± 0.03	
FeII	2586.650	-1.1605	14.52 ± 0.03^a	14.52 ± 0.03
	2600.173	-0.6216	> 14.09	
(4) 1127-145, $z = 0.3127$, UVES+STIS, $\log[N_{\text{HI}}/\text{cm}^{-2}] = 21.70 \pm 0.08$				
MgI	2852.964	0.2577	13.19 ± 0.03	13.19 ± 0.03^a
MgII	2796.352	-0.2130	> 14.07	> 14.35
	2803.531	-0.5151	> 14.35	
CaII	3934.777	-0.1871	12.69 ± 0.03	12.70 ± 0.03
	3969.591	-0.4921	12.73 ± 0.03	
MnII	2576.877	-0.4549	13.30 ± 0.03	13.26 ± 0.03
	2594.499	-0.5670	13.20 ± 0.03	
	2606.462	-0.7151	13.23 ± 0.03	
FeII	2344.214	-0.9431	> 14.71	> 15.16
	2374.461	-1.5045	> 15.16	
	2382.765	-0.4949	> 14.32	
	2586.650	-1.1605	> 14.92	
ZnII	2600.173	-0.6216	> 14.43	
	2026.136	-0.3107	13.57 ± 0.05	13.57 ± 0.05

Table 3. (contd.) Ionic column densities

Ion	λ (Å)	$\log f$	$\log[N_0/\text{cm}^{-2}]^b$	$\log[N/\text{cm}^{-2}]^b$
(5) 0827+243, $z = 0.5247$, UVES, $\log[N_{\text{HI}}/\text{cm}^{-2}] = 20.30 \pm 0.04$				
CaII	3934.777	-0.1871	12.59 ± 0.03	12.59 ± 0.03
	3969.591	-0.4921	12.60 ± 0.03	
TiII	3073.877	-0.9622	< 11.86	11.82 ± 0.04
	3230.131	-1.1630	< 11.97	
	3242.929	-0.6345	11.55 ± 0.12	
	3384.740	-0.4461	11.92 ± 0.04	
FeII	2249.877	-2.7397	14.79 ± 0.05	14.84 ± 0.03
	2260.781	-2.6126	14.96 ± 0.03	
	2344.214	-0.9431	> 14.66	
	2374.461	-1.5045	14.84 ± 0.03	
	2382.765	-0.4949	> 14.43	
(6) 0311+430, $z = 2.2890$, GMOS, $\log[N_{\text{HI}}/\text{cm}^{-2}] = 20.30 \pm 0.11$				
ZnII	2026.136	-0.3107	< 12.5	< 12.5
CrII	2056.254	-0.9788	< 13.05	< 13.05
MnII	2594.499	-0.5670	12.37 ± 0.11	12.50 ± 0.07
	2606.462	-0.7151	12.63 ± 0.09	
FeII	2249.877	-2.7397	14.80 ± 0.10	14.86 ± 0.06
	2260.781	-2.6126	14.91 ± 0.05	
	2374.461	-1.5045	> 14.32	

^aNote that the FeII λ 2586 line in the $z = 0.2378$ DLA towards 0952+179 and the MgI line in the $z = 0.3127$ DLA towards 1127-145 are both close to saturation. If the lines are saturated, the quoted column densities would be lower limits.

^bThe column densities measured from individual transitions are listed in the penultimate column ($\log[N_0/\text{cm}^{-2}]$), while the adopted column density for the species is listed in the final column ($\log[N/\text{cm}^{-2}]$). The adopted column density of a given species was obtained by a weighted mean of the measured column densities from all unsaturated lines. All limits are at 3σ significance.

posures were obtained with both UVES arms in the 346+580 nm standard wavelength setting, with a 1.0 arcsec slit.

Besides the above UVES observations, we also downloaded UVES data on a few DLAs of the sample from the VLT archive, along with the requisite calibration files obtained within a few nights of the science exposures. The instrumental calibration plan dictates how frequently the calibration exposures are obtained, based on knowledge of the instrument stability. The blue arm data downloaded by us on 0952+179 as part of program 69.A-0371(A) (PI: Savaglio) consist of three 5700 sec exposures with the 346 nm central wavelength setting. Data for 0827+243 were obtained as part of program 68.A-0170(A) (PI: Mallen-Ornelas) with both UVES arms in the 346+564 standard settings and four one-hour exposures. In all cases, the data were obtained with a 1.0 arcsec slit, with the detector binned by 2 in both the spatial and spectral directions.

The UVES data of 1127-145 were reduced with the UVES MIDAS pipeline version 2.1.0², while the archival UVES data were reduced using a custom version of the UVES pipeline, based on

² UVES pipelines are available at <http://www.eso.org/sci/data-processing/software/pipelines/>

Midas reduction routines. All data reduction followed the standard procedure for UVES data (e.g. Ellison et al. 2001), with wavelength calibration and normalization carried out for the individual spectra, before the spectra were optimally combined to produce the final one-dimensional spectrum on a heliocentric wavelength scale.

2.3.2 HST-STIS spectroscopy of 1127–145

The Space Telescope Imaging Spectrograph (STIS) on the Hubble Space Telescope (HST) was used in the E230M echelle mode in proposal 9173 (PI: J. Bechtold) to obtain an ultraviolet spectrum of 1127–145. These data were downloaded from the HST archive. The total exposure time on target amounted to 52,380 s with the $0.2'' \times 0.2''$ aperture. The HST-STIS data were reduced with the IDL version of CalSTIS v7.0 (Lindler 1999), following standard procedures, combining data from different exposures with weights inversely proportional to their variance.

2.3.3 GMOS observations of 0311+430

The $z = 2.2890$ DLA towards 0311+430 (York et al. 2007) was observed on 14 November 2007 with the Gemini Multi-Object Spectrograph (GMOS) on the Gemini North telescope (in proposal GN-2007B-Q-76). The quasar was observed in nod and shuffle mode with the R600 grating, a central wavelength of 800 nm and a $0.75''$ slit. The CCD was binned by two pixels in both the spatial and spectral directions. In nod and shuffle mode, the target is observed at two spatial positions on the slit in an ABBA configuration. The exposure time at each position was 30 seconds (120 seconds per cycle) with 19 cycles per exposure. Each exposure therefore has an effective integration time of 2280 seconds, with 6 exposures taken in all.

The data were reduced using the Gemini IRAF package following standard procedures, but with special modifications for the nod and shuffle mode. First, a bias was constructed, with an interactive fit to the overscan region, using GBIAS. A dark calibration frame was constructed using GNSDARK and subtracting the bias frame from the previous step. GSFLAT was used to make the master flat field from individual lamp exposures with interactive polynomial fits to remove the underlying spectral shape of the illumination. The application of these calibration frames (bias, dark and flat) to the science data was achieved using GSREDUCE. Sky subtraction is done using GNSSKYSUB on the 2-dimensional (2D) spectra by subtracting the shuffled image pixels from those in the unshuffled position. This step in the procedure is one of the great benefits of the nod and shuffle mode, and results in superior subtraction with much lower sky residuals than traditional long slit spectroscopy. For our reductions, with multiple exposures, GNSSKYSUB is called as part of the GNSCOMBINE routine which applies offsets to the various dithers and yields a single 2D spectrum. After the combination, the 2D frame has a positive and a negative spectrum at position A and B respectively. A first order wavelength correction (based on the image header information) of the science image and mosaicing of the 3 CCDs is achieved by running GSREDUCE again. GSREDUCE is also used to apply the master calibration files to the arc frames, before the wavelength solution is determined and applied to the science frame using GSWAVELENGTH and GSTRANSFORM respectively. The 1-D spectra (one positive and one negative) were then extracted using GSEXTRACT and averaged together after inversion of the negative spectrum. The final spectrum (obtained after binning by 2 in both spatial and spectral directions) has a wavelength

coverage of 6570 – 9450Å, a FWHM resolution of $\sim 3.1\text{Å}$ and a signal-to-noise ratio (S/N) per pixel of 30 – 50.

2.3.4 Keck-HIRES spectroscopy

The $z = 0.0912$ and $z = 0.2212$ DLAs towards 0738+313 were observed on 26 December 2006 with the Keck/ HIRES spectrometer (Vogt et al. 1994), configured with the blue cross-dispersor (i.e. HIRESb). We employed the E3 decker which affords a spectral resolution of $\text{FWHM} \approx 4 \text{ km s}^{-1}$. The grating was tilted to $\text{XDANGL}=1.039$ giving a nearly continuous wavelength coverage from $\lambda \approx 3100 - 5900\text{Å}$, but with two gaps owing to the CCD mosaic. The science frames (two exposures at 900s each) and associated calibration files were reduced with the HIREDUX data reduction pipeline³ (for details, see Prochaska et al. 2007). The spectra were optimally extracted and co-added (binning by 2 in the spatial direction), corrected to vacuum wavelengths and the heliocentric reference frame. The S/N at $\lambda \approx 4000\text{Å}$ is approximately 13 per 1.3 km s^{-1} pixel.

2.3.5 Abundances and velocity widths

The Keck-HIRES, VLT-UVES, GMOS-N and HST-STIS spectra were used to derive column densities and elemental abundances for six DLAs, at $z = 0.0912$ and $z = 0.2212$ towards 0738+313, $z = 0.2378$ towards 0952+179, $z = 0.3127$ towards 1127–145, $z = 0.5247$ towards 0827+243 and $z = 2.2890$ towards 0311+430. For all absorbers, the column densities for different species were estimated from the observed line profiles using the apparent optical depth method (AODM; Savage & Sembach 1991).

For the $z = 0.3127$ DLA towards 1127–145, the weakness of the ZnII lines in the HST-STIS spectrum prompted us to also try a different route. Here, the strong absorption lines in the VLT-UVES spectrum were first analysed with FITLYMAN (Fontana & Ballester 1995), with Voigt profiles first fitted to the CaII doublets alone, in order to determine the turbulent Doppler parameters and the redshifts of the individual components. These values were then fixed, together with the column density of the individual CaII doublets, and the ZnII and MnII lines included in the fit to determine the ZnII column density from the HST-STIS spectrum and the MnII column density from the VLT-UVES spectrum. This approach yielded $\log[N_{\text{ZnII}}/\text{cm}^{-2}] = 13.45 \pm 0.08$, consistent with the AODM value of $\log[N_{\text{ZnII}}/\text{cm}^{-2}] = 13.57 \pm 0.05$; the AODM value will be used in the following discussion, as it involves fewer assumptions. We note, in passing, that the Voigt profile fit to the MgI line yielded a larger MgI column density than that obtained from the AODM, with $\log[N_{\text{MgI}}/\text{cm}^{-2}] = 13.95 \pm 0.07$. This may be because the MgI line is nearly saturated in this absorber; in such situations, the AODM estimate should be regarded as a lower limit

Table 3 lists the column densities derived for various species in the six DLAs, along with the HI column density of the absorber. The abundances, relative to the solar abundance, on the solar scale of Asplund et al. (2009), are summarized for each system in Section 5. The metal lines detected in each spectrum (and, in some cases, a few undetected transitions) are plotted in Figs. 4 – 9.

Finally, we measured the velocity width at 90% optical depth, ΔV_{90} , of the low-ionization metal lines detected in our Keck-HIRES or VLT-UVES spectra of a subset of the absorbers of our sample following the criteria and procedures described in

³ <http://www.ucoick.org/~xavier/HIREDUX/index.html>

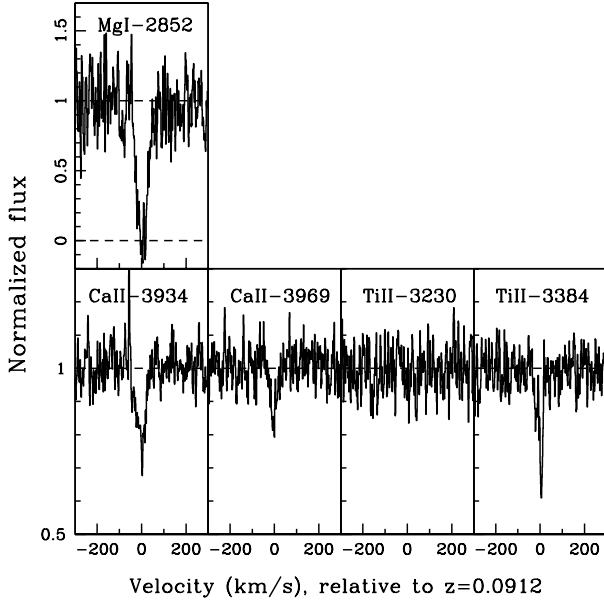


Figure 4. Low-ionization metal absorption profiles from the $z = 0.0912$ DLA towards 0738+313, from the Keck-HIRES spectrum. The x-axis represents velocity, in km s^{-1} , relative to the DLA redshift.

Prochaska & Wolfe (1997). In the majority of cases, we analyzed an unsaturated, low-ion transition observed at high S/N. For ≈ 5 systems, however, this did not prove possible (e.g. the DLA at $z = 0.2212$ toward 0738+313). In these cases, we measured ΔV_{90} from a modestly saturated line or a transition from a non-dominant ion (e.g. MgI $\lambda 2852$). Inspection of the full set of line profiles for these systems indicate that the results should be representative of the gas kinematics. The derived ΔV_{90} values are listed in Table 4, along with the transition used for the estimate.

3 SPIN TEMPERATURES, COVERING FACTORS AND VELOCITY WIDTHS

For a DLA towards a radio-loud background quasar, the HI column density N_{HI} , the HI 21cm optical depth $\tau_{21\text{cm}}$ and the spin temperature T_s are related by the expression (Rohlfs & Wilson 2006)

$$N_{\text{HI}} = C_0 \times T_s \times \int \tau_{21\text{cm}} dV, \quad (1)$$

where N_{HI} is in cm^{-2} , T_s is in K, the integral $\int \tau_{21\text{cm}} dV$ is over the observed line profile in velocity space, in km s^{-1} , and the constant $C_0 = 1.823 \times 10^{18} \text{ cm}^{-2} \text{ K}^{-1} \text{ km}^{-1} \text{ s}$. Note that the HI 21cm optical depth is given by $\tau_{21\text{cm}} = -\log[1 - \Delta S/S]$, where ΔS is the line depth and S is the flux density of the background quasar.

Equation 1 implicitly assumes that the all quantities are measured at the same spatial resolution. However, in the case of DLAs, the HI column density is measured from the redshifted Lyman- α absorption line towards the optical quasar, i.e. along a narrow pencil beam through the absorber. Conversely, the HI 21cm optical depth is measured against the more-extended radio emission. Ideally, the HI 21cm absorption studies should be carried out with very long baseline interferometry, so that the radio and optical sightlines have similar transverse extents in the absorber. Unfortunately, current VLBI arrays such as the VLBA or the European VLBI Network

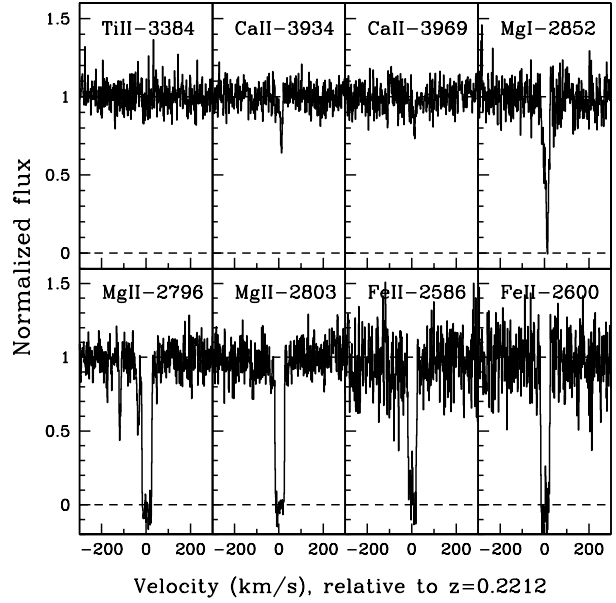


Figure 5. Low-ionization metal absorption profiles from the $z = 0.2212$ DLA towards 0738+313, from the Keck-HIRES spectrum. The x-axis contains velocity, in km s^{-1} , relative to the DLA redshift.

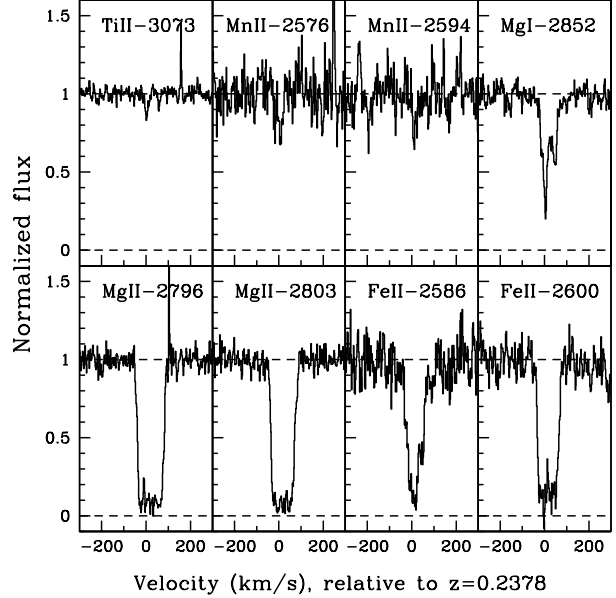


Figure 6. Low-ionization metal absorption profiles from the $z = 0.2378$ DLA towards 0952+179, from the VLT-UVES spectrum. The x-axis contains velocity, in km s^{-1} , relative to the DLA redshift.

have both very poor low-frequency coverage and low sensitivity. Further, even the 1000 km baselines of the next-generation Square Kilometre Array would only give a spatial resolution of ≈ 1 kpc at the redshift of a DLA at $z \approx 2$ (e.g. Kanekar & Briggs 2004), far worse than the “effective” resolution of hundreds of AU allowed by optical absorption spectroscopy (arising from the size of the background quasar). As a result, HI 21cm absorption studies are likely to continue to probe conditions on far larger spatial scales than op-

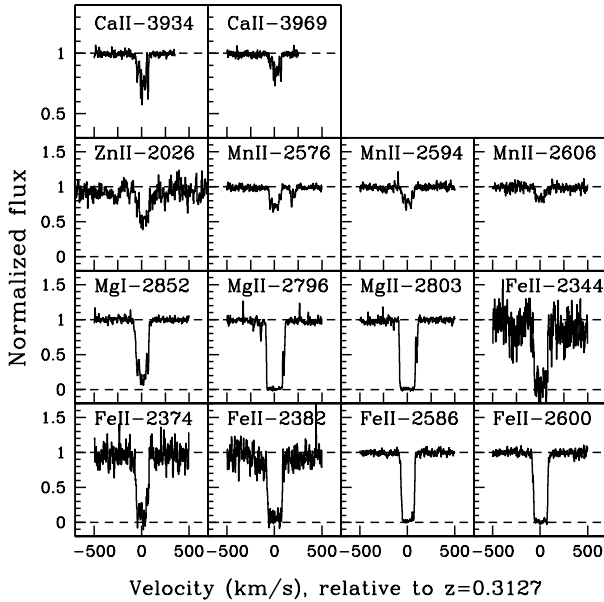


Figure 7. Low-ionization metal absorption profiles from the $z = 0.3127$ DLA towards 1127–145, from the VLT-UVES and HST-STIS spectra. The x-axis contains velocity, in km s^{-1} , relative to the DLA redshift.

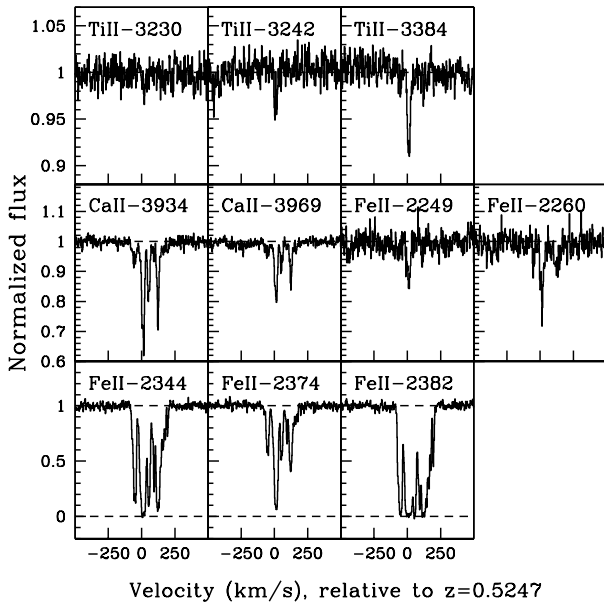


Figure 8. Low-ionization metal absorption profiles from the $z = 0.5247$ DLA towards 0827+243, from the VLT-UVES spectrum. The x-axis contains velocity, in km s^{-1} , relative to the DLA redshift.

tical absorption studies in the foreseeable future. One must hence attempt to correct for resolution effects, as has been done in the present and earlier studies (e.g. Briggs & Wolfe 1983; Carilli et al. 1996; Kanekar et al. 2009a; Ellison et al. 2012). This is discussed in detail below.

There are two effects that must be taken into account in the case of HI 21cm absorption studies at low angular resolution. First, for extended radio structure in the quasar, the foreground absorber may cover only part of the radio emission, but the angular extent of the emission may be smaller than the telescope beam and hence

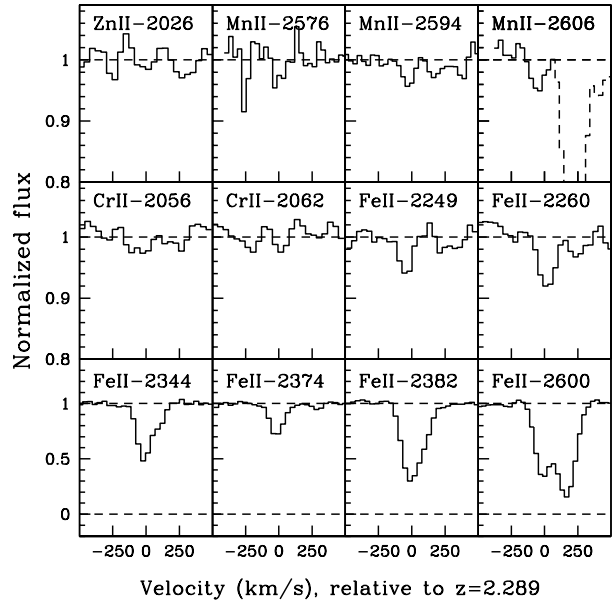


Figure 9. Low-ionization metal absorption profiles from the $z = 2.2890$ DLA towards 0311+430, from the GMOS-N spectrum. The x-axis contains velocity, in km s^{-1} , relative to the DLA redshift. The dashed part of the spectrum indicates absorption from a different redshift, which is slightly blended with the $\text{MnII}\lambda 2606$ line from the $z = 2.2890$ DLA.

unresolved. In such cases, if the (unresolved) total quasar flux density measured by the observer is S Jy, but only a fraction f of this emission is covered by the foreground absorber, the true HI 21cm optical depth is larger than the observed optical depth. The HI 21cm optical depth corrected for covering factor effects is given by $\tau_{21\text{cm}} = -\log[1 - \Delta S/(fS)]$ and equation (1) is modified to

$$N_{\text{HI}} = 1.823 \times 10^{18} \times T_s \times \int -\log \left[1 - \frac{\Delta S}{fS} \right] dV, \quad (2)$$

where f is referred to as the DLA covering factor. For most DLAs, the HI 21cm optical depth is low, $\tau_{21\text{cm}} \ll 1$, and the expression reduces to

$$N_{\text{HI}} = 1.823 \times 10^{18} \times [T_s/f] \int \frac{\Delta S}{S} dV. \quad (3)$$

The covering factor f is included in the above equation to account for the fact that low-frequency radio emission is often very extended, implying that the foreground DLA may not cover the entire background radio emission. The angular resolution of redshifted HI 21cm absorption studies (with single dishes or short-baseline interferometers like the GMRT or WSRT) is typically quite poor ($\gtrsim 10''$ for even the GMRT, i.e. $\gtrsim 80$ kpc for a DLA at $z \sim 3$), and the measured HI 21cm optical depth is hence a lower limit, because some of the radio emission may not be covered by the absorber. Curran et al. (2005) have emphasized unknown covering factors as a critical issue in interpreting the high spin temperatures typically obtained in HI 21cm absorption studies of high- z DLAs. This is because an apparently-low HI 21cm optical depth could arise due to an unknown low covering factor, a high spin temperature or an over-estimated HI column density.

The covering factor can be estimated from very long baseline interferometric (VLBI) studies close to the redshifted HI 21cm line frequency (Briggs & Wolfe 1983; Kanekar et al. 2009a), to measure the compact flux density arising from the radio core at this

frequency. The ratio of the core flux density to the total source flux density gives the quasar core fraction. In the following, we will assume that this quantity is a reasonable estimate of the covering factor. We note that this is not formally a measurement of the covering factor for an individual absorber because (1) it is possible that the absorber covers some fraction of the extended emission, in addition to the core emission, and (2) it is also possible that the absorber does not entirely cover the radio core. The latter is unlikely if the core size is significantly smaller than the size of a typical galaxy at the absorber redshift. Thus, for core sizes $\lesssim 1$ kpc, the ratio of the core flux density to the total source flux density should provide at least a lower limit to the covering factor.

We note, in passing, that the results of the paper are derived under the assumption that the DLA covering factor is equal to the quasar core fraction. However, in Section 7.9, we consider the possibility that the core fraction and covering factor are entirely unrelated, and use Monte Carlo simulations to show that the hypothesis that they are equal is actually not required for the results described below.

Until quite recently, there were very few estimates of DLA covering factors from low-frequency VLBI studies. This is because such studies are technically challenging due to propagation effects in the atmosphere, which can result in decorrelation of the signals on the long VLBI baselines. However, over the last few years, covering factors have been estimated for a large number of high- z DLAs, mostly with the low-frequency receivers of the VLBA (e.g. Kanekar et al. 2009a; Ellison et al. 2012; Srianand et al. 2012; Kanekar et al. 2013, ; this work).

The second issue that must be taken into account in the case of HI 21cm absorption studies at low angular resolution is the fact that, for DLAs, the HI column density in equation (3) is determined from the Lyman- α profile. Using this to derive the spin temperature involves the assumption that the HI columns along the optical and radio sightlines are the same. Since the optical quasar is far smaller than the radio core (typically, sizes of 100 – 1000 AU at optical wavebands and $\gtrsim 10$ pc in the radio), the HI column densities can, in principle, be different along the two sightlines. This assumption will be examined in detail in Section 7.3.

Next, for neutral gas along the line of sight at different temperatures, the spin temperature derived from equation (3) is the column-density-weighted harmonic mean of the spin temperatures of the different phases, i.e.

$$\frac{1}{T_s} = \sum_i \frac{n_i}{T_{s,i}} \quad (4)$$

where $n_i = N_i/N_{\text{HI}}$ is the fraction of the total HI column density in the i^{th} cloud, and $T_{s,i}$ is its spin temperature. Thus, a measurement of $T_s = T$ along a sightline could arise due to the presence of either a single intervening HI “cloud” with this spin temperature or a combination of clouds with spin temperatures above and below the measured value, T . For example, a measured spin temperature of ≈ 1000 K does not rule out the classic “two-phase” model of the neutral Galactic ISM (Field et al. 1969; McKee & Ostriker 1977), as this would arise naturally for sightlines with two types of HI “clouds”, at temperatures of ≈ 100 K and ≈ 8000 K.

It should be emphasized that the spin temperature along multi-phase sightlines is biased towards cold gas. Specifically, a sightline with HI equally divided between cold and warm phases, at spin temperatures of $T_s = 100$ K and $T_s = 8000$ K, respectively, would yield a derived spin temperature of ≈ 180 K. Conversely, a sightline with 90% of the HI at $T_s = 8000$ K, and 10% at $T_s = 100$ K would yield a derived spin temperature of ≈ 900 K. Further, col-

lisions drive the spin temperature towards the gas kinetic temperature (Wolfire et al. 1995, $\approx 40 - 200$ K;) in the cold neutral medium (CNM). However, in the warm neutral medium (WNM), the number density is too low to thermalize the transition and the spin temperature is typically significantly lower than the kinetic temperature T_k (e.g. $T_s \approx 1000 - 4000$ K for $T_k \approx 5000 - 8000$ K; Liszt 2001). The result of both these effects is that a high measured spin temperature ($\gtrsim 1000$ K) can only be explained by a preponderance of neutral gas in the WNM. The only caveat to this statement is if the HI column density measured towards the optical quasar is significantly larger than that towards the radio core, which, as we will discuss in Sec. 7.3, may occur on individual sightlines but is very unlikely to arise in a systematic manner.

For DLAs that do not show detectable HI 21cm absorption, one can use the upper limit on the HI 21cm optical depth in equation (3) to obtain a lower limit to the spin temperature. The derived limit depends on the assumed shape of the velocity profile; further, the detection sensitivity worsens with increasing line width ($\propto \sqrt{\Delta V}$, where ΔV is the line FWHM), implying that significant non-thermal broadening makes it harder to detect HI 21cm absorption. For non-detections, we will in all cases assume a gaussian profile of $\text{FWHM} = 15 \text{ km s}^{-1}$, corresponding to thermally-broadened HI at a kinetic temperature of 5000 K (i.e. in the WNM range). This is a conservative strategy as it allows for significant non-thermal broadening of cold HI along the line of sight. We also note that individual HI 21cm spectral components in DLAs with detected HI 21cm absorption typically have FWHMs of 5 – 15 km s^{-1} .

4 PROXIMATE DLAS AND SUB-DLAs

Two sub-classes of damped absorbers, proximate DLAs (“PDLAs”) and sub-DLAs, merit special mention (see also Ellison et al. 2012). PDLAs are defined as absorbers with redshifts within $\approx 3000 \text{ km s}^{-1}$ of the quasar redshift, i.e. arising in gas associated with the quasar host galaxy (e.g. Møller et al. 1998; Ellison et al. 2002; Prochaska et al. 2008). For such systems, the population distribution in the hyperfine levels, and thus the spin temperature, will be significantly influenced by the quasar radiation field at the HI 21cm line frequency (e.g. Field 1958; Wolfe & Burbidge 1975). Since this complicates the interpretation of the derived spin temperatures, we will exclude PDLAs from the later analysis and discussion.

Sub-DLAs are absorbers with HI column densities below the defining DLA column density of $N_{\text{HI}} = 2 \times 10^{20} \text{ cm}^{-2}$, but which still show damping wings in the Lyman- α profile (e.g. Péroux et al. 2003). Numerical estimates of self-shielding against the UV background in DLAs and sub-DLAs suggest that the absorbers are physically distinct: these studies find that most of the gas in DLAs is neutral, while that in sub-DLAs is predominantly ionized and at high temperatures (Viegas 1995; Prochaska 1999; Wolfe et al. 2005; Milutinovic et al. 2010). In keeping with the above, recent Galactic HI 21cm absorption studies have shown that the CNM fraction increases sharply at $N_{\text{HI}} \approx 2 \times 10^{20} \text{ cm}^{-2}$, with very low CNM fractions below this threshold (Kanekar et al. 2011). Sub-DLAs are thus likely to show significantly higher spin temperatures than DLAs; we will hence exclude them from the full sample and the later analysis.

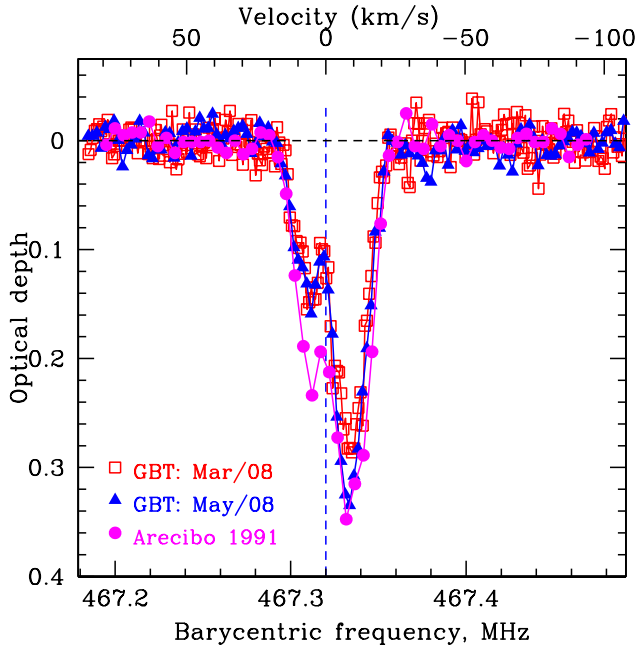


Figure 10. Comparison between the HI 21cm absorption profiles obtained from the $z = 2.0395$ DLA towards 0458–020 with the Arecibo telescope (in 1991) and the GBT telescope (in March and May 2008).

5 NOTES ON INDIVIDUAL SOURCES

The HI 21cm optical depths listed in Table 1 and the covering factors of Table 2 and Kanekar et al. (2009a) were used to derive spin temperatures for the DLAs and sub-DLAs of our sample whose HI 21cm data were not affected by RFI. The elemental abundances of Table 3 were used to complement and, in some cases, to improve the metallicities given in the literature. This section briefly summarizes the results for each absorber for which new data have been presented in this paper, again in order of increasing right ascension.

(i) 0201+113, $z = 3.3869$: The $z = 3.3869$ DLA towards 0201+113 was detected by White et al. (1993) and its HI column density was measured to be $N_{\text{HI}} = (1.8 \pm 0.3) \times 10^{21} \text{ cm}^{-2}$ by Ellison et al. (2001). After inconclusive results from a number of HI 21cm absorption studies with different radio telescopes (de Bruyn et al. 1996; Briggs et al. 1997; Kanekar & Chengalur 1997), HI 21cm absorption was finally detected from this absorber with the GMRT (Kanekar et al. 2007). The DLA covering factor is $f = 0.76$, from a 327 MHz VLBA imaging study (Kanekar et al. 2009a), yielding a spin temperature of $T_s = (1050 \pm 175) \times (f/0.76) \text{ K}$.

(ii) 0311+430, $z = 2.2890$: The $z = 2.2890$ DLA towards 0311+430 was found by Ellison et al. (2008) and has an HI column density of $(2.0 \pm 0.5) \times 10^{20} \text{ cm}^{-2}$ and a spin temperature of $T_s = (72 \pm 18) \times (f/0.52) \text{ K}$ (York et al. 2007; Kanekar et al. 2013). The SiII λ 1808 line, detected in the original low-resolution GMOS spectrum, yields $[\text{Si}/\text{H}] > -0.56$, assuming the line to be unsaturated (York et al. 2007; Ellison et al. 2008). We do not detect the ZnII λ 2026 line in our new GMOS spectrum (see Table 3), implying $\log[N_{\text{ZnII}}/\text{cm}^{-2}] < 12.5$ and $[\text{Zn}/\text{H}] < -0.43$. The metallicity of the $z = 2.2890$ DLA thus lies in the range $-0.56 < [\text{Z}/\text{H}] < -0.43$, from the ZnII upper limit and the SiII lower limit. However, we clearly detect the FeII λ 2249, λ 2260 and λ 2374 transitions in the new GMOS spectrum, with $\log[N_{\text{FeII}}/\text{cm}^{-2}] = 14.91 \pm 0.05$,

14.80 ± 0.10 and > 14.32 , respectively. Note that the FeII λ 2374 line yielded a lower column density than the other two lines, probably due to saturation effects. We have hence listed this as a lower limit, and used the former two lines to obtain $\log[N_{\text{FeII}}/\text{cm}^{-2}] = 14.86 \pm 0.06$, and $[\text{Fe}/\text{H}] = -0.89 \pm 0.13$. This yields a metallicity of $[\text{Z}/\text{H}] = [\text{Fe}/\text{H}] + 0.4 = -0.49 \pm 0.13$ for the $z = 2.2890$ DLA.

(iii) 0336–017, $z = 3.0621$: The $z = 3.0621$ DLA towards 0336–017 was found by Lu et al. (1993), with an HI column density of $N_{\text{HI}} = (1.5 \pm 0.3) \times 10^{21} \text{ cm}^{-2}$ (Prochaska et al. 2001). The DLA covering factor is $f = 0.68$ (Kanekar et al. 2009a); our upper limit on the HI 21cm optical depth then yields the lower limit $T_s > 8890 \times (f/0.68) \text{ K}$ on the DLA spin temperature, assuming an FWHM of 15 km s^{-1} for the HI 21cm line. We note that this T_s limit is extremely high, at the upper end of the range of WNM kinetic temperatures. The low-ionization metal lines of this DLA have a relatively large velocity spread, $\Delta V_{90} \approx 108 \text{ km s}^{-1}$ (see Table 4). However, even assuming that the HI 21cm line has a comparable velocity FWHM (perhaps due to non-thermal broadening) would only lower the spin temperature limit to $T_s \geq 8890 \times \sqrt{(15/108)}$, i.e. to $T_s \geq 3315 \text{ K}$. The HI content in this DLA thus appears to be dominated by warm gas, unless there is significant small-scale structure along the sightline and the HI column along the radio sightline is much lower than that towards the optical quasar.

(iv) 0347–211, $z = 1.9470$: The $z = 1.9470$ DLA towards 0347–211 was detected by Ellison et al. (2001) in the CORALS survey, and has an HI column density of $N_{\text{HI}} = (2.0 \pm 0.5) \times 10^{20} \text{ cm}^{-2}$. No low-frequency VLBI images of the background quasar are currently available; we hence do not have a reliable estimate of its covering factor. Our upper limit on the HI 21cm optical depth yields $T_s > (380 \times f) \text{ K}$.

(v) 0405–331, $z = 2.5693$: The PDLA towards 0405–331 has an HI column density of $N_{\text{HI}} = (4 \pm 1) \times 10^{20} \text{ cm}^{-2}$ (Ellison et al. 2001) and a covering factor of $f = 0.44$ (Kanekar et al. 2009a), yielding $T_s > 1220 \times (f/0.44) \text{ K}$.

(vi) 0432–440, $z = 2.3020$: The $z = 2.3020$ DLA towards 0432–440 has an HI column density of $N_{\text{HI}} = (6.0 \pm 1.5) \times 10^{20} \text{ cm}^{-2}$ (Ellison et al. 2001). The VLBA 327 MHz image of this DLA shows a weak extension, but we were unable to obtain a stable 2-component fit (probably due to the weakness of the extension); we hence used a single-Gaussian model here, obtaining $f = 0.38$. Combining this with our upper limit on the HI 21cm optical depth yields $T_s > 555 \times (f/0.38) \text{ K}$.

(vii) 0438–436, $z = 2.3474$: This DLA has an HI column density of $N_{\text{HI}} = (6.0 \pm 1.5) \times 10^{20} \text{ cm}^{-2}$ (Ellison et al. 2001), and a covering factor of $f = 0.59$ (Kanekar et al. 2009a). The GBT detection of HI 21cm absorption then yields $T_s = (900 \pm 250) \times (f/0.59) \text{ K}$ (Kanekar et al. 2006).

(viii) 0454+039, $z = 0.8597$: The $z = 0.8597$ DLA towards 0454+039 has an HI column density of $N_{\text{HI}} = (5.0 \pm 0.7) \times 10^{20} \text{ cm}^{-2}$ (Boisse et al. 1998; see also Steidel et al. 1995) and a covering factor $f = 0.53$ (Kanekar et al. 2009a). Our GBT upper limit to the HI 21cm optical depth then yields $T_s > 990 \times (f/0.53) \text{ K}$.

(ix) 0458–020, $z = 2.0395$: There are multiple estimates of the HI column density of this DLA, $N_{\text{HI}} = (4.5 - 6) \times 10^{21} \text{ cm}^{-2}$ (Wolfe et al. 1993; Pettini et al. 1994; Møller et al. 2004; Heinmüller et al. 2006), from different telescopes and spectrographs, all consistent with each other within the measurement errors. We will use the value $N_{\text{HI}} = (6 \pm 1) \times 10^{21} \text{ cm}^{-2}$ (Møller et al. 2004), as this was obtained from a high-sensitivity VLT-FORS1 spectrum (the other results use either echelle spectroscopy or 4m-class telescopes).

HI 21cm absorption in the $z = 2.0395$ DLA was originally de-

Table 4. The main sample of DLAs with HI 21cm absorption studies and low-frequency VLBI estimates of the covering factor. See Section 6 for a description of the columns of the table.

QSO	z_{QSO}	z_{abs}	$\log[\text{N}_{\text{HI}}/\text{cm}^{-2}]$	f	T_s (K)	[Z/H]	Z	[Z/Fe]	Dust	ΔV_{90}^a (km s^{-1})	Line	Refs. ^b
0738+313	0.635	0.0912	21.18 ± 0.06	0.98	775 ± 100	-1.21 ± 0.16	Fe ^c	< 0.46	Fe	42	TiII λ 3384	2-5
0738+313	0.635	0.2212	20.90 ± 0.08	0.98	870 ± 160	< -0.72	Zn	< 0.71	Cr	60	MgI λ 2852	2-6
0952+179	1.472	0.2378	21.32 ± 0.05	0.66	6470 ± 965	-1.89 ± 0.06	Fe ^c	< 1.27	Fe	98	MgI λ 2852	1,5,7-9
1127-145	1.184	0.3127	21.70 ± 0.08	0.90	820 ± 145	-0.76 ± 0.10	Zn	< 1.23	Fe	123	CaII λ 3934	1,6,7,9,10
1229-021	1.043	0.3950	20.75 ± 0.07	0.42	95 ± 15	-0.45 ± 0.15	Zn	> 0.81	Fe	122	MnII λ 2576	9,11-13
0235+164	0.940	0.5242	21.70 ± 0.09	1.00	210 ± 45	-0.14 ± 0.17	XR ^d	1.71 ± 0.45	Fe	-	-	14,15,16
0827+243	0.939	0.5247	20.30 ± 0.04	0.70	330 ± 65	-0.51 ± 0.05	Fe ^c	-	-	188	FeII λ 2374	5,7-9,16
1429+400	1.215	0.6039	21.20 ± 0.10	0.32	90 ± 23	-0.80 ± 0.21	Zn	0.70 ± 0.24	Fe	70	MnII λ 2576	17
1122-168	2.400	0.6819	20.45 ± 0.05	0.04	> 100	-0.90 ± 0.29	Fe ^c	< -0.17	Fe	144	FeII λ 2586	1,18
1331+305	0.849	0.6922	21.25 ± 0.02	0.90	965 ± 105	-1.35 ± 0.05	Zn	0.26 ± 0.06	Fe	26	MnII λ 2576	12,19,20
0454+039	1.350	0.8596	20.69 ± 0.06	0.50	> 1380	-0.99 ± 0.12	Zn	-0.02 ± 0.12	Fe	100	FeII λ 2260	1,12,21,22
2149+212	1.538	0.9115	20.70 ± 0.10	0.02	> 55	< -0.93	Zn	-	-	-	-	1,23,24
2355-106	1.639	1.1727	21.00 ± 0.10	1.00	2145 ± 570	-0.87 ± 0.20	Zn	0.50 ± 0.23	Fe	126	MnII λ 2576	17,25,26
1621+074	1.648	1.3367	21.35 ± 0.10	0.34	460 ± 105	-1.07 ± 0.14	Zn	0.45 ± 0.15	Fe	55	FeII λ 2260	17,26
2003-025	1.457	1.4106	20.54 ± 0.20	0.81	485 ± 195	-	-	-	-	-	-	1,24,25
1331+170	2.084	1.7764	21.18 ± 0.07	0.72	625 ± 115	-1.27 ± 0.09	Zn	0.74 ± 0.09	Fe	72	SiII λ 1808	9,27-30
1157+014	2.000	1.9436	21.80 ± 0.07	0.63	1015 ± 255	-1.44 ± 0.10	Zn	0.35 ± 0.10	Fe	84	NiII λ 1741	9,31-34
0458-020	2.286	2.0395	21.78 ± 0.07	1.00	560 ± 95	-1.27 ± 0.08	Zn	0.45 ± 0.10	Fe	84	CrII λ 2056	27,35-37
2039+187	3.056	2.1920	20.70 ± 0.09	0.35	160 ± 35	-	-	-	-	-	-	38,39
1048+347	2.520	2.2410	20.54 ± 0.06	0.69	> 2155	-	-	-	-	-	-	38,39
0311+430	2.870	2.2890	20.30 ± 0.11	0.52	72 ± 18	-0.49 ± 0.13	Fe ^c	> 0.33	Fe	-	-	1,38-40
0432-440	2.649	2.3020	20.78 ± 0.11	0.38	> 555	-1.09 ± 0.13	Si	0.34 ± 0.15	Fe	125	FeII λ 1608	1,41,42
0438-436	2.863	2.3474	20.78 ± 0.11	0.59	900 ± 250	-0.69 ± 0.12	Zn	0.59 ± 0.16	Fe	55	FeII λ 2260	1,41-43
0229+230	3.420	2.6200	20.30 ± 0.11	0.30	> 140	-	-	-	-	-	-	38,39
0229+230	3.420	2.6830	20.70 ± 0.09	0.30	> 270	-	-	-	-	-	-	38,39
1402+044	3.215	2.7076	21.01 ± 0.23	0.34	> 890	-	-	-	-	-	-	1,44-46
0913+003	3.074	2.7434	20.74 ± 0.11	0.54	> 925	-1.44 ± 0.16	Si	0.13 ± 0.19	Fe	105	SiII λ 1526	1,41,42
2039+187	3.056	2.7520	20.70 ± 0.09	0.35	> 790	-	-	-	-	-	-	38,39
1354-170	3.147	2.7799	20.30 ± 0.15	0.97	> 1030	-1.83 ± 0.16	Si	0.54 ± 0.18	Fe	30	FeII λ 1608	1,47
0800+618	3.033	2.9603	20.50 ± 0.02	0.63	> 570	-	-	-	-	-	-	1,48
0537-286	3.110	2.9746	20.30 ± 0.11	0.47	> 520	< -0.40	Zn	-	-	-	-	9,41,42,49
2342+342	3.053	2.9084	21.10 ± 0.10	0.71	> 2200	-1.06 ± 0.10	S	0.47 ± 0.12	Fe	100	SiII λ 1808	1,9,47,50
0336-017	3.197	3.0621	21.20 ± 0.10	0.68	> 8890	-1.36 ± 0.10	S	0.39 ± 0.11	Fe	108	SiII λ 1250	1,9,30,51
0335-122	3.442	3.1799	20.78 ± 0.11	0.62	> 1850	-2.53 ± 0.16	Si	0.07 ± 0.19	Fe	39	AlII λ 1670	9,41,42,49
0201+113	3.639	3.3869	21.25 ± 0.07	0.76	1050 ± 175	-1.19 ± 0.17	S	0.16 ± 0.22	Fe	64	NiII λ 1317	9,52-55
1239+376	3.819	3.4110	20.40 ± 0.09	0.54	> 2330	-	-	-	-	-	-	38,39
1418-064	3.689	3.4482	20.40 ± 0.10	0.69	> 930	-1.45 ± 0.14	Si	0.25 ± 0.17	Fe	41	FeII λ 1608	1,9,41,42

^aMost of the ΔV_{90} measurements were carried out by us; a few values are taken from Prochaska & Wolfe (1999) and Ledoux et al. (2006).

^bReferences for N_{HI} , metallicity, covering factor and spin temperature estimates: (1) This work, (2) Rao & Turnshek (1998), (3) Chengalur & Kanekar (1999), (4) Lane et al. (2000), (5) Kulkarni et al. (2005), (6) Lane et al. (1998), (7) Rao & Turnshek (2000), (8) Kanekar & Chengalur (2001a), (9) Kanekar et al. (2009a), (10) Chengalur & Kanekar (2000), (11) Brown & Spencer (1979), (12) Boisse et al. (1998), (13) Lanzetta & Bowen (1992), (14) Roberts et al. (1976), (15) Junkkarinen et al. (2004), (16) Chen et al. (2005), (17) Ellison et al. (2012), (18) de la Varga et al. (2000), (19) Wolfe et al. (2008), (20) Brown & Roberts (1973), (21) Pettini et al. (2000), (22) Steidel et al. (1995), (23) Nestor et al. (2008), (24) Rao et al. (2006), (25) Kanekar et al. (2009b), (26) Gupta et al. (2009), (27) Wolfe & Davis (1979), (28) Carswell et al. (2011), (29) Prochaska & Wolfe (1999), (30) Prochaska et al. (2001), (31) Wolfe et al. (1981), (32) Ledoux et al. (2003), (33) Dessauges-Zavadsky et al. (2007), (34) Dessauges-Zavadsky et al. (2006), (35) Wolfe et al. (1985), (36) Briggs et al. (1989), (37) Møller et al. (2004), (38) Ellison et al. (2008), (39) Kanekar et al. (2013), (40) York et al. (2007), (41) Ellison et al. (2001), (42) Akerman et al. (2005), (43) Kanekar et al. (2006), (44) Prochaska et al. (2005), (45) Noterdaeme et al. (2009), (46) Curran et al. (2010), (47) Prochaska et al. (2003), (48) Jorgenson et al. (2006), (49) Kanekar & Chengalur (2003), (50) Prochaska et al. (2007), (51) Ledoux et al. (2006), (52) White et al. (1993), (53) Kanekar et al. (2007), (54) Srianand et al. (2012), (55) Ellison et al. (2001), (56) Møller & Warren (1993), (57) Lu et al. (1996), (58) Srianand et al. (2010), (59) Storrie-Lombardi & Wolfe (2000), (60) Lopez & Ellison (2003), (61) Ledoux et al. (2002), (62) Bergeron & Stasińska (1986), (63) Roy et al. (2013).

^cIn five DLAs, at $z = 0.0912$ towards 0738+313, $z = 0.2378$ towards 0952+179, $z = 0.5247$ towards 0827+243, $z = 0.6819$ towards 1122-168 and $z = 2.2890$ towards 0311+430, the metallicity was estimated using $[\text{Z}/\text{H}] = [\text{Fe}/\text{H}] + 0.4$, following Prochaska et al. (2003). However, in four of the five cases (excluding the DLA towards 0827+243), limits are also available on $[\text{Zn}/\text{H}]$ or $[\text{Si}/\text{H}]$; these limits were used along with the $[\text{Fe}/\text{H}]$ measurements to derive the dust depletion $[\text{Z}/\text{Fe}]$.

^dIn the case of the $z = 0.5242$ DLA towards 0235+164, the metallicity is from an X-ray absorption study (Junkkarinen et al. 2004).

Table 5. DLAs or sub-DLAs with HI 21cm absorption studies, but not included in the “main” sample

QSO	z_{QSO}	z_{abs}	$\log[N_{\text{HI}}/\text{cm}^{-2}]$	f	T_s (K)	[Z/H]	Z	[Z/Fe]	Dust	ΔV_{90} (km s^{-1})	Line	Refs. ^b
PDLAs, with the absorber within 3000 km s^{-1} of the background quasar												
0105–008	1.374	1.3708	21.70 ± 0.15	0.32	305 ± 45	-1.40 ± 0.16	Zn	0.16 ± 0.16	Fe	33	FeII λ 2249	9,17,26
0824+355	2.249	2.2433	20.30	0.20	> 320	–	–	–	–	–	–	1,48
0405–331	2.570	2.5693	20.60 ± 0.11	0.44	> 1220	-1.37 ± 0.16	Si	0.35 ± 0.19	Fe	261	SiII λ 1526	1,41,42
1013+615	2.805	2.7681	20.60 ± 0.15	0.81*	> 945	–	–	–	–	–	–	1,44,54
0528–250	2.813	2.8110	21.35 ± 0.07	0.94	> 2103	-0.89 ± 0.10	Zn	0.45 ± 0.13	Fe	304	SiII λ 1253	1,54,56,57
1354–107	3.006	2.9660	20.78 ± 0.11	–	> 615	-1.28 ± 0.16	Si	0.24 ± 0.19	Fe	59	SiII λ 1808	41,42,49
J1337+3152	3.174	3.1745	21.36 ± 0.10	1.00*	600 ± 297	-1.73 ± 0.28	Zn	0.17 ± 0.29	Fe	–	–	58
Sub-DLAs, with $N_{\text{HI}} < 2 \times 10^{20} \text{ cm}^{-2}$												
2128–123	0.501	0.4297	19.37 ± 0.08	–	> 980	–	–	–	–	–	–	49,61
0215+015	1.715	1.3439	19.89 ± 0.09	–	> 1020	-0.66 ± 0.22	Fe	–	–	–	–	49,62
0237–233	2.223	1.6724	19.78 ± 0.07	0.90	390 ± 125	-0.57 ± 0.12	Zn	0.09 ± 0.12	Fe	43	FeII λ 2374	17,25
1402+044	3.215	2.4850	20.20 ± 0.20	0.35	> 380	–	–	–	–	–	–	1,44–46
J1406+3433	2.566	2.4989	20.20 ± 0.20	0.76	> 210	–	–	–	–	–	–	44,45,54
J0733+2721	2.938	2.7263	20.25 ± 0.20	–	> 690	–	–	–	–	–	–	45,54
DLAs with covering factor estimates at frequencies significantly higher (> 1.5 times) the redshifted HI 21cm line frequency												
0620+389	3.469	2.0310	20.30 ± 0.11	0.79	> 400	–	–	–	–	–	–	38,39
J0852+2431	3.617	2.7902	20.70 ± 0.20	0.49	> 420	–	–	–	–	–	–	45,54
J0816+4823	3.573	3.4358	20.80 ± 0.20	0.60	> 145	–	–	–	–	–	–	45,54
Absorbers without covering factor estimates												
J0011+1446	4.967	3.4523	21.65 ± 0.15	–	> 3040	–	–	–	–	–	–	63
0347–211	2.944	1.9470	20.30 ± 0.11	–	> 380	< –0.55	Zn	–	–	–	–	1,41,42
1614+051	3.215	2.5200	20.40	–	> 450	–	–	–	–	–	–	1,59
J0407–4410	3.020	2.5950	21.05 ± 0.10	–	> 380	-1.00 ± 0.10	Zn	0.35 ± 0.10	Fe	79	SiII λ 1808	51,54,60
J0407–4410	3.020	2.6214	20.47 ± 0.10	–	> 80	-1.99 ± 0.12	Si	0.33 ± 0.12	Fe	–	–	54,60
J0801+4725	3.276	3.2235	20.70 ± 0.15	–	> 2820	–	–	–	–	–	–	45,54,63
J1435+5435	3.811	3.3032	20.30 ± 0.20	–	> 420	–	–	–	–	–	–	45,54

References: See Table 4.

* These PDLAs also have covering factor estimates at frequencies > 1.5 times higher than the redshifted HI 21cm line frequency.

tected by Wolfe et al. (1985), with two distinct absorption components (see also Briggs et al. 1989). We observed the HI 21cm line with the GBT on two separate occasions, in March and May 2008; these spectra are shown in Fig. 10, overlaid on an old HI 21cm spectrum obtained with the Arecibo telescope (kindly provided by Art Wolfe). The GBT and Arecibo spectra are clearly different, with the secondary HI 21cm component significantly weaker in the GBT spectra. We note that part of this discrepancy might arise due to flux scale errors (and perhaps bandpass calibration issues) in the Arecibo spectrum, given that the source is at the edge of the Arecibo declination range. However, while the secondary component has the same depth in the two GBT runs, a statistically-significant difference is seen in the primary component. Indeed, the integrated HI 21cm optical depths obtained at the GBT are $\int \tau_{21\text{cm}} dV = (5.534 \pm 0.080) \text{ km s}^{-1}$ in March 2008 and $\int \tau_{21\text{cm}} dV = (6.198 \pm 0.088) \text{ km s}^{-1}$ in May 2008; the difference has $\approx 5\sigma$ significance, indicating that the HI 21cm absorption has changed on a timescale of ≈ 2 months. No significant narrow-band interference was observed on either observing run and the doppler shift between the runs is $\approx 20 \text{ km s}^{-1}$, comparable to the FWHMs of the components. We conclude that the spectra show evidence for variability in the HI 21cm profile, on

timescales of months, and possibly of years. Such line variations have been seen earlier, on timescales as short as a few days, in two low- z DLAs, at $z \sim 0.5242$ towards AO0235+164 (Wolfe et al. 1982) and $z \sim 0.3127$ towards 1127–145 (Kanekar & Chengalur 2001b). They can be explained by a number of scenarios, including refractive interstellar scintillation, gravitational microlensing, transverse motion of compact components in the quasar radio jet, etc (e.g. Briggs 1983; Kanekar & Chengalur 2001b; Gwinn 2001; Macquart 2005), all typically requiring small-scale structure in the quasar radio emission, the ISM of the absorber and/or the ISM of the Galaxy.

The DLA covering factor has been estimated to be ≈ 1 from a VLBI study in the HI 21cm line (Briggs et al. 1989). The average integrated HI 21cm optical depth from the two GBT runs is $\int \tau_{21\text{cm}} dV = (5.866 \pm 0.059) \text{ km s}^{-1}$; we then obtain $T_s = (560 \pm 95) \text{ K}$, assuming $f = 1$. Note that the HI 21cm optical depth is fairly high, $\tau \approx 0.3$, implying that the low optical depth approximation of equation (3) should not be used.

(x) 0528–250, $z = 2.8112$: The $z = 2.8112$ PDLA towards 0528–250 has an HI column density of $(2.24 \pm 0.05) \times 10^{21} \text{ cm}^{-2}$ (Møller & Warren 1993) and a covering factor of unity (Kanekar et al. 2009a). Our WSRT non-detection of HI 21cm

absorption then yields $T_s > 925 \times (f/1.0)$ K. We note that Srianand et al. (2012) present a GBT spectrum of this absorber, obtaining an upper limit of $\int \tau_{21\text{cm}} dV < 0.58 \text{ km s}^{-1}$ and $T_s > 2103$ K, using the b-parameter of the detected H_2 absorption for the line width. We have quoted this result in Table 5, due to its higher sensitivity.

(xi) 0738+313, $z = 0.0912$: This is the lowest redshift DLA of the sample, with $N_{\text{HI}} = (1.5 \pm 0.21) \times 10^{21} \text{ cm}^{-2}$ (Rao & Turnshek 1998) and $T_s = (775 \pm 100) \times (f/0.98)$ K (Chengalur & Kanekar 1999; Lane et al. 2000). Note that this is one of the few DLAs whose spin temperature has been directly measured from a VLBA H I 21cm absorption study (Lane et al. 2000). Kulkarni et al. (2005) detected Fe II and Cr II absorption from this system in an HST-STIS spectrum, yielding $[\text{Fe}/\text{H}] = -1.61 \pm 0.16$ and $[\text{Cr}/\text{H}] = -1.55 \pm 0.23$; their non-detection of $\text{Zn II } \lambda 2026$ absorption gives $[\text{Zn}/\text{H}] < -1.15$. Our Keck-HIRES spectrum yields $\log[N_{\text{TiII}}/\text{cm}^{-2}] = 12.51 \pm 0.04$ and thus a titanium abundance $[\text{Ti}/\text{H}] = -1.58 \pm 0.08$. This is consistent with the original Ti II detection of Khare et al. (2004), from a medium-resolution spectrum ($\log[N_{\text{TiII}}/\text{cm}^{-2}] = 12.53^{+0.14}_{-0.06}$).

(xii) 0738+313, $z = 0.2212$: The second DLA towards 0738+313 was also detected by Rao & Turnshek (1998), with $N_{\text{HI}} = (7.9 \pm 1.5) \times 10^{20} \text{ cm}^{-2}$; this has $T_s = (870 \pm 160) \times (f/0.98)$ K (Lane et al. 1998; Chengalur & Kanekar 1999; Kanekar et al. 2001). Zn II absorption was not conclusively detected in the HST-STIS spectrum of Kulkarni et al. (2005), giving $[\text{Zn}/\text{H}] < -0.72$. However, these authors did detect Cr II absorption from the DLA, with $[\text{Cr}/\text{H}] = -1.43 \pm 0.22$. We obtain $\log[N_{\text{FeII}}/\text{cm}^{-2}] > 14.30$ and $\log[N_{\text{TiII}}/\text{cm}^{-2}] < 11.90$ from our Keck-HIRES spectrum, yielding $[\text{Fe}/\text{H}] > -2.05$ and $[\text{Ti}/\text{H}] < -1.91$.

(xiii) 0800+618, $z = 2.9603$: This absorber was detected in the UCSD survey of Jorgenson et al. (2006), with an H I column density of $N_{\text{HI}} = (3.16 \pm 0.15) \times 10^{20} \text{ cm}^{-2}$. Using this with our covering factor estimate ($f = 0.63$) and our limit on the H I 21cm optical depth yields $T_s > 570 \times (f/0.63)$ K.

(xiv) 0824+355, $z = 2.2433$: The PDLA towards 0824+355 has $N_{\text{HI}} = 2 \times 10^{20} \text{ cm}^{-2}$ (Jorgenson et al. 2006). The VLBA 327 MHz image shows three clear components, apparently a core with an extended jet, and possibly a fourth weak component. We fit a 3-component model to the image, obtaining a core covering factor of $f = 0.20$. Our non-detection of H I 21cm absorption then yields $T_s > 320 \times (f/0.20)$ K.

(xv) 0827+243, $z = 0.5247$: This is another DLA from the HST sample of Rao & Turnshek (2000), with $N_{\text{HI}} = (2.00 \pm 0.18) \times 10^{20} \text{ cm}^{-2}$. H I 21cm absorption was detected in this absorber by Kanekar & Chengalur (2001a) and its covering factor measured by Kanekar et al. (2009a); the DLA spin temperature is $T_s = (330 \pm 65) \times (f/0.7)$ K. Kulkarni et al. (2005) give weak upper limits on the Zn and Cr abundances from their HST-STIS non-detections of absorption, with $[\text{Zn}/\text{H}] < -0.04$ and $[\text{Cr}/\text{H}] < 0.43$. Conversely, detections of Fe II and Mn II absorption in a medium-resolution spectrum Khare et al. (2004) yielded $[\text{Fe}/\text{H}] = -1.01 \pm 0.11$ and $[\text{Mn}/\text{H}] = -0.86 \pm 0.35$ (Chen et al. 2005). Our high-resolution VLT-UVES spectrum gives a slightly higher Fe II column density (albeit consistent within the errors), with $[\text{Fe}/\text{H}] = -0.91 \pm 0.05$, and also yields $[\text{Ti}/\text{H}] = -1.39 \pm 0.06$. The DLA metallicity is then $[\text{Z}/\text{H}] = [\text{Fe}/\text{H}] + 0.4 = -0.51 \pm 0.05$.

(xvi) 0913+003, $z = 2.7434$: The DLA towards 0913+003 has $N_{\text{HI}} = (5.5 \pm 1.4) \times 10^{20} \text{ cm}^{-2}$ (Ellison et al. 2001) and $f = 0.54$. Our GBT non-detection of H I 21cm absorption then yields $T_s > 925 \times (f/0.54)$ K.

(xvii) 0952+179, $z = 0.2378$: The $z = 0.2378$ DLA towards 0952+179 was detected by Rao & Turnshek (2000), with $N_{\text{HI}} = (2.09 \pm 0.24) \times 10^{21} \text{ cm}^{-2}$. Kanekar & Chengalur (2001a) detected H I 21cm absorption in this absorber, and its covering factor was measured to be $f = 0.66$ by Kanekar et al. (2009a), giving $T_s = (6470 \pm 965) \times (f/0.66)$ K. Kulkarni et al. (2005) report an upper limit on the Zn II column density (with $[\text{Zn}/\text{H}] < -1.02$) and a detection of Cr II absorption (with $[\text{Cr}/\text{H}] = -1.64 \pm 0.16$). Our VLT-UVES spectrum yields $\log[N_{\text{FeII}}/\text{cm}^{-2}] = 14.52 \pm 0.03$, and $[\text{Fe}/\text{H}] = 2.29 \pm 0.06$. This gives a metallicity of $[\text{Z}/\text{H}] = [\text{Fe}/\text{H}] + 0.4 = -1.89 \pm 0.06$. We also obtain $[\text{Ti}/\text{H}] = -1.61 \pm 0.07$ and $[\text{Mn}/\text{H}] = -2.22 \pm 0.07$.

(xviii) 1013+615, $z = 2.7670$: Prochaska et al. (2005) obtain $N_{\text{HI}} = (4.0 \pm 0.9) \times 10^{20} \text{ cm}^{-2}$ for this PDLA from an SDSS spectrum [see also Jorgenson et al. (2006) and Srianand et al. (2012)]. No VLBI studies of this quasar have been carried out at frequencies similar to that of the redshifted H I 21cm line. While Srianand et al. (2012) estimate $f = 0.86$, this is from a 1.4 GHz VLBA image. Our GBT non-detection of H I 21cm absorption yields $T_s > 1100 \times f$ K, about a factor of 1.5 more sensitive than the non-detection of Srianand et al. (2012).

(xix) 1122-168, $z = 0.6819$: The $z = 0.6819$ DLA towards 1122-168 has $N_{\text{HI}} = (2.82 \pm 0.99) \times 10^{20} \text{ cm}^{-2}$ (de la Varga et al. 2000). The VLBA image of the background quasar shows at least two components, with a total flux density of ≈ 50 mJy. We identify the more compact component with the quasar core; this has a total 1.4 GHz flux density of 12 mJy, yielding a covering factor of $f \approx 0.04$. If both components are covered by the foreground DLA, the covering factor would be $f \approx 0.17$. Our GBT upper limit to the H I 21cm optical depth yields $T_s > 100 \times (f/0.04)$ K; the weak limit is due to the extremely low covering factor.

(xx) 1127-145, $z = 0.3127$: With $N_{\text{HI}} = (5.01 \pm 0.92) \times 10^{21} \text{ cm}^{-2}$ (Rao & Turnshek 2000), this is one of the highest column density DLAs at low redshifts, $z \lesssim 0.5$. H I 21cm absorption from this DLA was originally detected by Lane et al. (1998) (see also Kanekar & Chengalur 2001b) and the covering factor measured by Kanekar et al. (2009a); the DLA spin temperature is $(820 \pm 145) \times (f/0.9)$ K. Our detection of Zn II absorption in the HST-STIS spectrum yields $\log[N_{\text{ZnII}}/\text{cm}^{-2}] = 13.53 \pm 0.13$, and $[\text{Zn}/\text{H}] = -0.80 \pm 0.16$. We also obtain $\log[N_{\text{MnII}}/\text{cm}^{-2}] = 13.26 \pm 0.03$ and $\log[N_{\text{FeII}}/\text{cm}^{-2}] > 15.16$, implying $[\text{Mn}/\text{H}] = -1.92 \pm 0.09$ and $[\text{Fe}/\text{H}] > -2.0$, from the VLT-UVES spectrum.

(xxi) 1157+014, $z = 1.9436$: H I 21cm absorption from this DLA was detected by Wolfe et al. (1981), using the Arecibo telescope. The DLA has an H I column density of $N_{\text{HI}} = (6.3 \pm 1.5) \times 10^{21} \text{ cm}^{-2}$ (Wolfe et al. 1981; Ledoux et al. 2003) and a covering factor of $f = 0.63$ (Kanekar et al. 2009a). The new GBT H I 21cm spectrum, shown in Fig. 1[A], confirms the detection of Wolfe et al. (1981), although the absorption is significantly weaker in our spectrum. We note, however, that strong out-of-band RFI has been found at the GBT around the redshifted H I 21cm line frequency (≈ 482.5 MHz); this could imply significant uncertainty in our flux density calibration. We will hence use the original integrated H I 21cm optical depth of Wolfe et al. (1981) to estimate the spin temperature; this yields $T_s = (1015 \pm 255) \times (f/0.63)$ K.

(xxii) 1354-170, $z = 2.7799$: This DLA has an H I column density of $N_{\text{HI}} = (2.0 \pm 0.7) \times 10^{20} \text{ cm}^{-2}$ (Prochaska et al. 2003) and a covering factor of ≈ 0.97 (this work). Our GBT non-detection of H I absorption then yields $T_s > 1030 \times (f/0.97)$ K.

(xxiii) 1402+044, $z = 2.7076$: The H I column density of this DLA is $N_{\text{HI}} = (1.0 \pm 0.5) \times 10^{21} \text{ cm}^{-2}$ (Noterdaeme et al. 2009; see also Prochaska et al. 2005) and its covering factor is $f = 0.34$

(this work). Combining these with our upper limit on the HI 21cm optical depth yields $T_s > 890 \times (f/0.34)$ K.

(xxiv) 1418–064, $z = 3.4483$: This CORALS DLA has an HI column density of $N_{\text{HI}} = (2.5 \pm 0.6) \times 10^{20} \text{ cm}^{-2}$ (Ellison et al. 2001) and a covering factor of $f = 0.69$ (Kanekar et al. 2009a). Our GMRT non-detection of HI 21cm absorption then yields $T_s > 930 \times (f/0.69)$ K.

(xxv) 1614+051, $z = 2.5200$: This DLA has $N_{\text{HI}} = 2.5 \times 10^{20} \text{ cm}^{-2}$ (Storrie-Lombardi & Wolfe 2000), but does not have an estimate of the covering factor; we obtain $T_s > 450 \times f$ K.

(xxvi) 2003–025, $z = 1.4106$: This DLA was found by Rao et al. (2006) in their HST survey of strong MgII $\lambda 2796$ absorbers, with $N_{\text{HI}} = (3.5 \pm 1.6) \times 10^{20} \text{ cm}^{-2}$. HI 21cm absorption was later detected in this absorber by Kanekar et al. (2009b). The VLBA image shows a central core with weak extended emission, and a core covering factor of $f = 0.53$; this yields a spin temperature of $T_s = (485 \pm 195) \times (f/0.53)$ K.

(xxvii) 2149+212, $z = 0.9115$: The $z = 0.9115$ DLA towards 2149+212 was also found by Rao et al. (2006). Unfortunately, its very low covering factor ($f = 0.03$) implies that our GBT upper limit on the HI 21cm optical depth only yields a weak limit on the spin temperature, $T_s > 55 \times (f/0.03)$ K.

(xxviii) 2342+342, $z = 2.9082$: This DLA was detected by White et al. (1993), and has $N_{\text{HI}} = (1.3 \pm 0.3) \times 10^{21} \text{ cm}^{-2}$ (Prochaska et al. 2003) and $f = 0.71$ (Kanekar et al. 2009a). Our GMRT non-detection of HI 21cm absorption then yields $T_s > 2200 \times (f/0.71)$ K.

6 THE FULL SAMPLE

Including systems from the literature, the full sample of DLAs and sub-DLAs towards “compact” radio quasars with estimates of the spin temperature via HI 21cm absorption spectroscopy now contains 60 systems (e.g. Kanekar & Chengalur 2003; Srianand et al. 2012; Ellison et al. 2012; Kanekar et al. 2013; this work). This includes six sub-DLAs, with $10^{19} \text{ cm}^{-2} < N_{\text{HI}} < 2 \times 10^{20} \text{ cm}^{-2}$, and seven PDLAs, for which the absorber redshift lies within 3000 km s^{-1} of the quasar redshift. Note that we have excluded DLAs towards extended radio sources (e.g. at $z = 0.4369$ towards 3C196 (Brown & Mitchell 1983; Briggs et al. 2001), $z = 0.5318$ towards 1629+12 (Rao & Turnshek 2000; Kanekar & Chengalur 2003) and $z = 0.6561$ towards 3C336 (Rao & Turnshek 2000; Curran et al. 2007) from the sample, as the optical and radio sightlines are very different for these sources.

Seven absorbers of the full sample are PDLAs. As noted earlier, spin temperatures in PDLAs are likely to be affected by the proximity of a bright radio source; we will hence exclude these systems from our analysis. The six sub-DLAs are also expected to have systematically higher spin temperatures than DLAs, based on observations in the Galaxy (Kanekar et al. 2011); these too will be excluded from the analysis. For seven DLAs, the lack of covering factor estimates implies that we only have estimates of T_s/f from the HI 21cm absorption spectroscopy; we will exclude these systems from the following discussion. 37 of the remaining 40 DLAs have covering factor estimates at low frequency (≤ 1.4 GHz) VLBI studies, at frequencies within a factor of ≈ 1.5 of the redshifted HI 21cm line frequency (e.g. Kanekar et al. 2009a; Ellison et al. 2012; Kanekar et al. 2013, ; this work). The covering factor estimates are likely to be reliable in these cases. However, for three absorbers at $z > 2$, the VLBI images are at 1.4 GHz, more than a factor of 3 larger than the redshifted HI 21cm line frequency (Srianand et al.

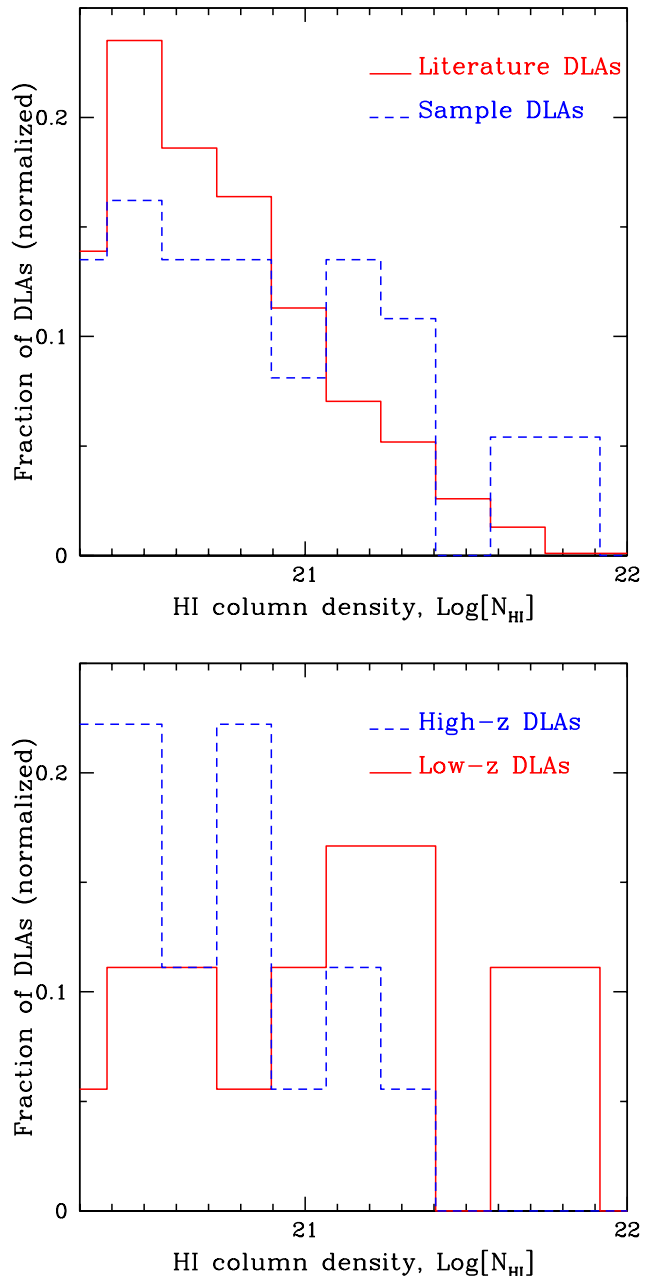


Figure 11. [A] Top panel: Histograms of the distribution of the N_{HI} values of the 37 DLAs of our sample and of a sample of 1080 DLAs from a number of surveys in the literature. A Wilcoxon two-sample test finds no statistically-significant evidence against the hypothesis that the sample DLAs are drawn from the general population; see main text for discussion. [B] Bottom panel: Histograms of the distributions of the N_{HI} values of the low- z (solid) and high- z (dashed) DLA sub-samples, separated at the median redshift $z = 2.192$. A Wilcoxon two-sample test finds that the two N_{HI} distributions are different at $\approx 3\sigma$ significance.

2012; Kanekar et al. 2013). Compact radio cores are likely to have an inverted spectrum (due to synchrotron self-absorption), while extended radio structure is expected to have a steep spectrum. As a result, measurements of the covering factor at a significantly higher frequency than the line frequency could over-estimate the covering factor, and hence, under-estimate the spin temperature. We will

hence also exclude these three systems from our analysis, ending with 37 *bona fide* DLAs towards compact background quasars with covering factor measurements close to the redshifted HI 21cm line frequency.

Our final sample of 37 absorbers contains 19 detections of HI 21cm absorption, nine at $z < 1$, five at $1 < z < 2$, four at $2 < z < 3$ and one at $z > 3$. Of the 18 remaining systems with non-detections of HI 21cm absorption, fourteen have strong lower limits on the spin temperature, $T_s > 500$ K, while four have weak lower limits, $T_s > 55 - 270$ K. We emphasize that all systems of the sample have estimates of the DLA covering factor from low-frequency VLBI studies. These covering factor estimates have been used to derive the DLA spin temperatures.

Detailed information on various properties of the absorbers of the full sample is provided in Tables 4 and 5. The 37 absorbers constituting our final sample are listed in Table 4, while Table 5 contains the 23 excluded systems: (1) the seven PD-LAs, (2) the six sub-DLAs, (3) the three DLAs with estimates of f at frequencies > 1.5 times the redshifted HI 21cm line frequency, and (4) the seven DLAs with no covering factor estimates. The columns of both tables contain: (1) the quasar name, (2) the quasar emission redshift, (3) the DLA absorption redshift, (4) the HI column density and error, (5) the covering factor (i.e. the quasar core fraction at low frequencies), (6) the spin temperature or lower limits to T_s , after correcting for the absorber covering factor, (7) the metallicity $[Z/H]$, (8) Z , the element used for the metallicity estimate, (9) the dust depletion $[Z/Fe]$, (10) “Dust”, the element used for the dust abundance, (11) the velocity spread of the low-ionization metal lines, between 90% optical depth points, ΔV_{90} , in km s^{-1} (Prochaska & Wolfe 1997), (12) the metal-line transition on which the ΔV_{90} estimate is based, and (13) references for the HI column density, spin temperature, abundances and ΔV_{90} values. The metallicities are relative to the solar abundance, on the scale of Asplund et al. (2009). Following Prochaska et al. (2003), we have used, in order of preference, $[Z/H] \equiv [Zn/H]$, $[S/H]$, $[Si/H]$ and $[Fe/H]+0.4$, except for the $z = 0.524$ DLA towards AO0235+164, where the metallicity is from an X-ray measurement (Junkkarinen et al. 2004). Most of the ΔV_{90} estimates are from our own Keck- HIRES or VLT-UVES high-resolution echelle spectra.

7 RESULTS AND DISCUSSION

7.1 The present T_s sample and the general DLA population

Before proceeding with a discussion of the various properties of our final sample of DLAs, it is relevant to test whether the sample is representative of the known DLA population, so that inferences drawn from the former can be applied to the latter. Since the defining property of a damped Lyman- α system is its HI column density, we compared the distribution of N_{HI} values in our sample with those of the general DLA population. The comparison sample was made up of 1080 DLAs drawn from a variety of surveys (Storrie-Lombardi & Wolfe 2000; Ellison et al. 2001; Jorgenson et al. 2006; Rao et al. 2006; Prochaska et al. 2005; Noterdaeme et al. 2009). The distributions of N_{HI} values in the two samples are shown in Fig. 11[A], where the fraction of DLAs plotted on the y-axis has been normalized to unity in the bin with the largest fraction to allow for a direct comparison between the two distributions. A similar plot in Fig. 11[B] compares the N_{HI} distributions in the high- z and low- z DLA samples.

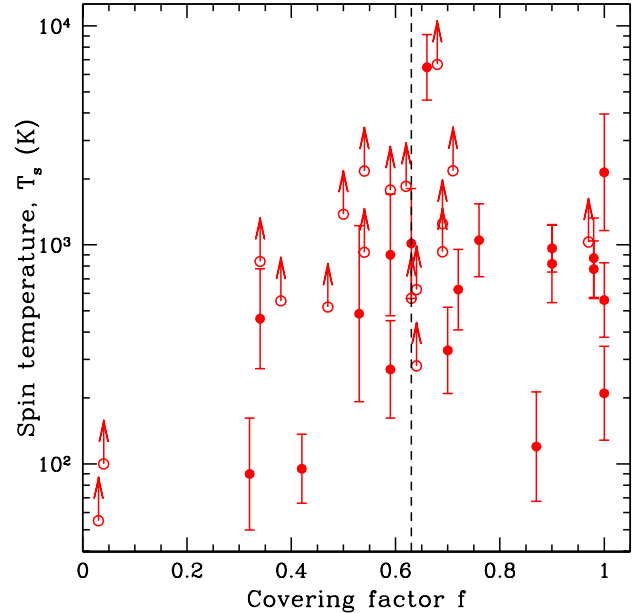


Figure 13. The spin temperature T_s plotted against the covering factor for the 37 DLAs of the sample; non-detections of HI 21cm absorption are indicated by lower limits to the spin temperature. The median covering factor $f_{\text{med}} = 0.63$ is indicated by the vertical dashed line. No evidence was found that either the detection probability or the spin temperature depends on the absorber covering factor.

While the fraction of high- N_{HI} DLAs appears larger in the HI 21cm sample, the number of absorbers in this sample is quite small (37 systems), implying large fluctuations from Poisson statistics. The literature sample is dominated by the SDSS DLAs, at $z \geq 2.2$; conversely, the median absorber redshift in our sample is $z_{\text{med}} = 2.192$, so our sample contains a significantly higher fraction of low- z DLAs than the literature sample (e.g. $\approx 40\%$ at $z < 1.5$ in our sample, against $\approx 3\%$ for the literature sample). While the samples have different redshift distributions, a number of studies have found no evidence for redshift evolution in the HI column density distribution function (e.g. Prochaska et al. 2005; Zwaan et al. 2005). We find that the N_{HI} distributions of our sample and the literature DLAs agree within 1.8σ significance in a Wilcoxon two-sample test⁴. We hence conclude that there is no statistically significant evidence against the null hypothesis that the DLAs of our sample are representative of the general DLA population.

7.2 The covering factor

It has been suggested by Curran & Webb (2006) (see also Curran 2012) that unknown covering factors are the main cause of the high spin temperature estimates in high- z DLAs. These authors argue that this is due to a geometric effect, owing to the fact that the angular diameter distances of absorbers at $z \geq 1$ are comparable to those of the background quasars (at $z > 1$), implying that higher-redshift absorbers are “less efficient” at obscuring the background radio emission and hence have lower covering factors. While this

⁴ The statistical tests described here were mostly carried out using the Astronomical Survival analysis ASURV package (Isobe et al. 1986).

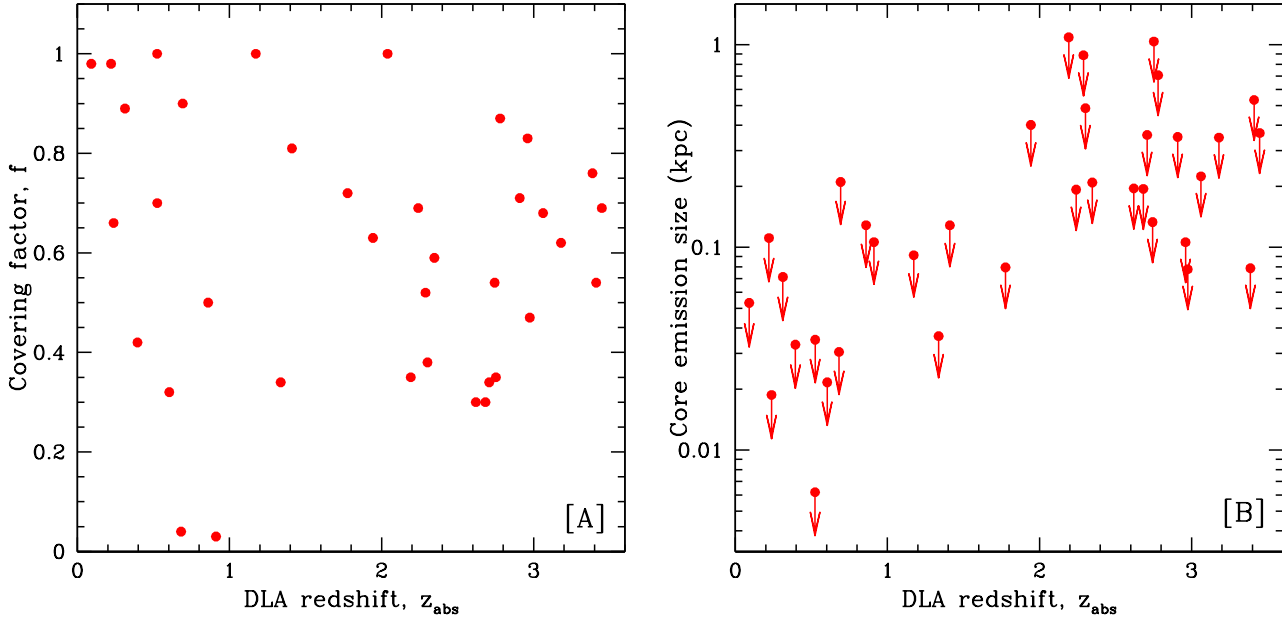


Figure 12. [A] Left panel: The covering factors of the 37 DLAs of the full sample, plotted against absorber redshift, z_{abs} . No difference is apparent between the distributions of covering factors above and below the median redshift, $z_{\text{med}} = 2.192$. [B] Right panel: The spatial extent of the compact radio emission of the background quasars (at the DLA redshift), plotted against z_{abs} . Note that each point is an upper limit to the size of the radio emission, due to the possibility of residual phase errors in the VLBA data. The points have hence been shown with downward-pointing arrows. As a result, the limits are much poorer for the DLAs at $z \geq 2$, as all these systems were observed with the VLBA at 327 MHz, where the ionospheric activity is significantly worse than at higher frequencies. Despite this, the upper limit to the core size is ≤ 1 kpc in 36 out of the 37 DLAs of the sample.

may or may not be applicable for systems which do not have estimates of the low-frequency covering factor f , all 37 DLAs of our sample have estimates of the covering factor at frequencies within a factor of 1.5 of the redshifted HI 21cm line frequency. The estimated covering factors are plotted versus redshift in Fig. 12[A]; no evidence was found for a difference between the distributions of covering factors for the sub-samples of absorbers with $z < z_{\text{med}}$ and $z > z_{\text{med}}$ (note that $z_{\text{med}} = 2.192$); the distributions agree within 0.7σ significance in a Wilcoxon two-sample test.

Fig. 12[B] plots the upper limit to the spatial extent of the core radio emission at the DLA redshift versus the DLA redshift. While the spatial extent does appear to be larger at high redshifts, it should be emphasized that the core spatial extents plotted in Fig. 12[B] are *upper limits*, due to the possibility of residual phase errors in the VLBA data. This issue is especially important at low frequencies (327 MHz and 606 MHz), due to ionospheric effects. As a result, the size estimates of Fig. 12[B] are systematically larger for the DLAs at $z \geq 2$, as these were all observed with the 327 MHz VLBA receivers.

Fig. 12[B] shows that the background radio cores have a transverse size of ≤ 1 kpc at the absorber redshift in 36 of the 37 absorbers, significantly smaller than the size of even dwarf galaxies. For DLAs at $z > 2$, the median upper limit (due to the possibility of residual phase errors) to the transverse size of the core emission is ≈ 350 pc. This indicates that the radio cores are likely to be entirely covered by all the foreground absorbers. The sole exception is 0458–020, where the agreement between VLBI and single-dish HI 21cm absorption profiles led Briggs et al. (1989) to argue that the $z = 2.0395$ DLA covers both the radio core and the extended lobes, implying an absorber size ≥ 16 kpc; note that this system lies off the scale in Fig. 12[B].

We also examined whether the probability of detecting HI 21cm absorption or the estimated spin temperatures depend on the absorber covering factors. Fig. 13 plots the spin temperature versus covering factor for the 37 DLAs of the sample. The median covering factor of the absorbers in the sample is $f_{\text{med}} = 0.64$. For sightlines with $f > f_{\text{med}}$, there are 12 detections and 5 non-detections of HI 21cm absorption, while sightlines with $f < f_{\text{med}}$ have 7 detections and 11 non-detections. The detection probabilities are $71^{+27}_{-20}\%$ for the high- f sample and $37^{+20}_{-13}\%$ for the low- f sample.⁵ Thus, while the detection rate appears higher for the high- f sample (as would be expected on physical grounds), the difference is not statistically significant (agreeing within $\approx 1.2\sigma$ significance) in the current sample. Similarly, a Peto-Prentice generalized Wilcoxon two-sample test (for censored data) finds no evidence for a difference between the distributions of T_s values for the high- f and low- f samples; the two T_s distributions agree within 0.1σ significance. We thus find no statistically significant evidence that the probability of detecting HI 21cm absorption or the spin temperature estimates depend on the absorber covering factor.

The fact that we do not detect a significant dependence of the

⁵ The quoted errors are 1σ Gaussian confidence intervals, based on small-number Poisson statistics (Gehrels 1986). Note that the error does not scale linearly with confidence interval, e.g. the 2σ lower confidence interval is not twice the 1σ lower confidence interval, and care is hence needed while comparing detection rates for different sub-samples. In all cases, we have used two approaches to test whether the detection rates for different sub-samples are in agreement: (1) naively assuming that the errors scale linearly with confidence interval, and (2) checking whether the 2σ confidence intervals of the detection rates of the sub-samples overlap with each other. The quoted differences in the detection rates are from the first approach.

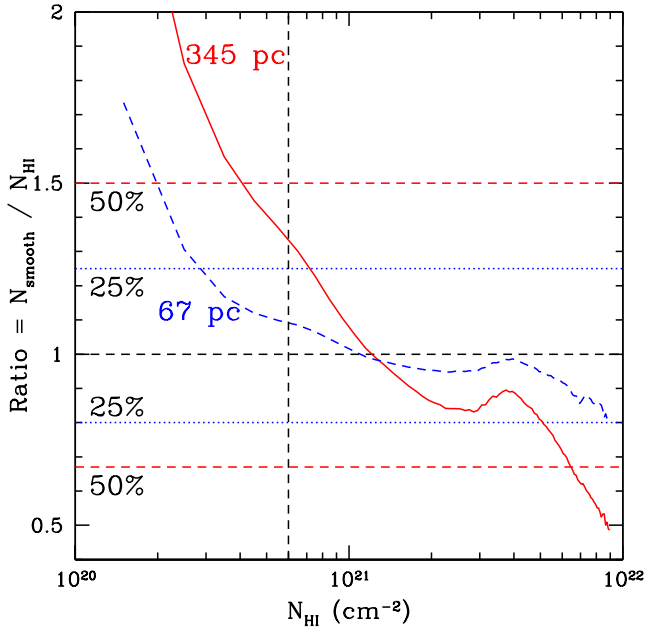


Figure 14. HI in the LMC: the ratio of the smoothed HI column density N_{smooth} at spatial resolutions of 67 pc (dashed curve) and 345 pc (solid curve) to the HI column density at the original (15 pc) resolution N_{HI} plotted versus N_{HI} . The horizontal dotted and dashed lines respectively demarcate regions where the ratio is within 25% and 50% of unity. The dashed vertical line indicates $N_{\text{HI}} = 6 \times 10^{20} \text{ cm}^{-2}$, the median HI column density of the DLA sample.

detection rate of HI 21cm absorption on covering factor may appear surprising. This is likely to be at least partly due to the fact that the sample is still relatively small, with only ≈ 18 systems apiece in the high- f and low- f sub-samples. Further, the sensitivity to HI 21cm absorption is not uniform across the sample: the optical depth sensitivity is typically better for brighter background sources.

We will revisit the arguments of Curran & Webb (2006) regarding angular diameter distances in Section 7.6.

7.3 Differing HI columns along optical and radio sightlines

As noted in Section 3, a critical assumption in estimating spin temperatures in DLAs is that the HI column densities measured from the damped Lyman- α profile can be used in equation (3), i.e. that the N_{HI} values along the optical and radio sightlines are the same. If the HI columns are systematically different along the radio and the optical sightlines (e.g. if there is significant spatial structure in the HI distribution), it would lead to systematic errors in the derived spin temperatures. For example, Wolfe et al. (2003) suggest that the average HI column towards the radio core of 0201+113 may be significantly lower than that towards the optical quasar, thus resulting in an incorrectly high estimate of the spin temperature. Note that this effect is not the same as the issue of the geometric covering factor discussed in the preceding section, although the two are often confused in the literature.

Absorption spectroscopy of lensed quasars provides an interesting tool to measure HI column density along multiple sightlines through a DLA, and to thus test for structure in the HI distribution (e.g. Smette et al. 1995; Zuo et al. 1997; Lopez et al. 2005; Monier et al. 2009). For example, Smette et al. (1995) measured HI column densities of $\log[N_{\text{HI}}/\text{cm}^{-2}] = 20.6$ and $\log[N_{\text{HI}}/\text{cm}^{-2}] =$

17.6 at $z = 1.6616$ towards images A and B of quasar HE 1104–1805, respectively, at a separation of $\approx 3''$ (≈ 26 kpc at the redshift). Conversely, Lopez et al. (2005) found the HI column densities in a $z = 0.9313$ galaxy towards images A and B of the quasar HE 0552–3315 to be in excellent agreement, at a separation of $0.644''$ (≈ 5.2 kpc at the absorber redshift). Unfortunately, there are as yet only a handful of DLAs known towards lensed quasars.

The most direct way of testing whether the HI columns are different along the radio and optical sightlines is to compare HI column densities measured from pencil-beam (i.e. ultraviolet or optical) studies and studies at coarser angular resolution. This has been done in the Galaxy (Dickey & Lockman 1990; Wakker et al. 2011), by comparing N_{HI} values obtained at the same or neighbouring locations from Lyman- α absorption studies of background quasars and HI 21cm emission studies. Wakker et al. (2011) carried out such a comparison along 59 sightlines, using HST-STIS Lyman- α absorption spectra and HI 21cm emission spectra at angular resolutions of $9' - 36'$ from the GBT and the 140-foot telescope. For the former, the N_{HI} values were derived from the usual Voigt profile fits to the damping wings of the Lyman- α line, as is done for high- z DLAs. For the latter, the N_{HI} values were inferred under the assumption that the HI 21cm emission is optically-thin, in which case the observed HI 21cm emission brightness temperature is directly proportional to the HI column density (Rohlfs & Wilson 2006). Wakker et al. (2011) found the HI column densities obtained from the two methods to be in excellent agreement, with the ratio having a mean value of unity and a dispersion of 10%. Note that one does not know the distance to the absorbing clouds, and hence cannot estimate the spatial resolution of the HI 21cm emission spectra. If the clouds are at an average distance of ≈ 1 kpc, it would imply that the HI column density averaged over regions of size ≈ 10 pc is similar to that on scales of 100 – 1000 AU.

Similarly, Welty et al. (2012) compared HI column densities in the Large Magellanic Cloud (LMC) measured from the Lyman- α absorption profile towards stars in the LMC and HI 21cm emission spectroscopy at a spatial resolution of 15 pc. They found good agreement between the N_{HI} values by excluding HI 21cm emission from gas lying behind the stars (based on the emission velocity). This too indicates that the HI column density on scales of $\approx 100 - 1000$ AU is similar to that on scales of ≈ 15 pc.

However, Fig. 12[B] shows that the spatial extent subtended by the radio core at the DLA redshift may be significantly larger than 10 pc, with a median value of ≈ 350 pc for DLAs at $z > 2$. Although, as noted in the preceding section, these transverse sizes are upper limits, most of the background quasars are likely to have radio cores of spatial extent greater than a few tens of parsecs at the redshift of the foreground DLA (see Wolfe et al. 2003, for the $z = 3.387$ DLA towards 0201+113). This is because the angular size of the radio core must be sufficiently large at low frequencies to have a brightness temperature lower than either the equipartition limit or the inverse Compton limit ($\approx 10^{11} - 10^{12}$ K; Kellermann & Pauliny-Toth 1969; Readhead 1994; Singal 2009), unless the radio emission is relativistically beamed towards us. Relativistic beaming is unlikely to be important for most of the background quasars of our sample, as few of them have highly variable flux densities. Thus, for most of the absorbers of the sample, the radio core emission is likely to subtend a transverse size of tens of pc, and perhaps as large as a few hundred pc, at the DLA redshift.

One thus has to hence examine whether the HI column density averaged over spatial scales of a few hundred pc is systematically different from that measured along a pencil beam. A direct comparison between the HI column densities measured from the

Lyman- α line and from HI 21cm emission has so far been carried out in a single DLA, at $z = 0.009$ towards SBS 1549+593 (Bowen et al. 2001). For this system, Chengalur & Kanekar (2002) measured $N_{\text{HI}} \approx (4.9 \pm 0.6) \times 10^{20} \text{ cm}^{-2}$ from a GMRT HI 21cm emission study with a spatial resolution of ≈ 5.3 kpc at the DLA redshift, while Bowen et al. (2001) obtained a slightly lower value, $N_{\text{HI}} \sim (2.2 \pm 0.5) \times 10^{20} \text{ cm}^{-2}$, from the damped Lyman- α profile (albeit with unknown systematic errors due to the extended wings of the STIS G140L grating line spread function and blending with the Lyman- α line of the Galaxy; Bowen et al. 2001). Note that the spatial resolution of the HI 21cm study here is far larger than the typical transverse scale subtended by the radio cores at the redshifts of the DLAs of our sample.

An alternative approach is to compare the HI column density measured at high spatial resolution along sightlines in an HI 21cm emission cube of a nearby galaxy with the N_{HI} values obtained along the same sightlines on smoothing the cube to lower spatial resolutions. Such a comparison was carried out by Ryan-Weber et al. (2005), between N_{HI} values measured at 15 pc and 3.6 kpc resolution. These authors found that the fine structure — both low and high column density — is washed out on smoothing to 3.6 kpc resolution, resulting in sightlines with original N_{HI} values in the sub-DLA regime returning higher values and gas with $N_{\text{HI}} > 10^{21} \text{ cm}^{-2}$ yielding values with $N_{\text{HI}} < 10^{21} \text{ cm}^{-2}$.

We follow the same approach as Ryan-Weber et al. (2005), analysing a high-spatial-resolution HI 21cm emission image of the LMC, obtained by combining data from the Australia Telescope Compact Array and the Parkes multi-beam receiver (Kim et al. 2003). The spectral cube has a spatial resolution of ≈ 15 pc at the distance of the LMC. We have smoothed the cube to different spatial resolutions, up to a maximum of 1 kpc, and measured the HI column density at the same position at each resolution, assuming the HI 21cm emission to be optically thin in all cases. Finally, we averaged the results from different spatial locations with the same value of the original, unsmoothed HI column density, using uniform N_{HI} bins.

The results are shown in Fig. 14, which plots the ratio of the HI column density measured at two different spatial resolutions (67 pc and 345 pc) to that at the original resolution (15 pc) versus the unsmoothed N_{HI} . These spatial resolutions were chosen because the median transverse sizes of quasar radio cores at the absorber redshift are ≈ 70 pc and ≈ 350 pc for DLAs at $z < 2$ and $z > 2$, respectively, allowing a direct comparison.

It is clear that the behaviour depends on the absolute value of the HI column density: at both smoothed resolutions, the ratio is larger than unity (i.e. the smoothed HI column density is larger than the original) for $N_{\text{HI}} \lesssim 10^{21} \text{ cm}^{-2}$, and lower than unity (i.e. the smoothed N_{HI} is lower than the original) for $N_{\text{HI}} \gtrsim 10^{21} \text{ cm}^{-2}$. However, smoothing to a resolution of ≈ 67 pc does not significantly alter the HI column density over most of the range: the mean value of the ratio is within $\approx 10\%$ of unity for $5.0 \times 10^{20} \text{ cm}^{-2} < N_{\text{HI}} < 6.3 \times 10^{21} \text{ cm}^{-2}$. Even for $2 \times 10^{20} \text{ cm}^{-2} < N_{\text{HI}} < 5 \times 10^{20} \text{ cm}^{-2}$, the ratio is < 1.5 .

The situation is similar in the case of smoothing to a spatial resolution of 345 pc, although with somewhat larger deviations from unity. Here, the ratio is within 25% of unity for $N_{\text{HI}} = (0.7 - 5.1) \times 10^{21} \text{ cm}^{-2}$, within 50% of unity over the ranges $N_{\text{HI}} = (5.1 - 6.5) \times 10^{21} \text{ cm}^{-2}$ and $N_{\text{HI}} = (4 - 7) \times 10^{20} \text{ cm}^{-2}$, and lower than 2 for $N_{\text{HI}} = (2 - 4) \times 10^{20} \text{ cm}^{-2}$.

The above results can be used to draw inferences about the derived spin temperatures in DLAs, *assuming that the spatial distribution of HI in DLAs is similar to that in the LMC*. From the

above results, using the HI column density measured from the damped Lyman- α profile in the equation for the HI 21cm optical depth to derive the spin temperature would not result in a *systematically higher or lower* T_s estimate in all DLAs. The spin temperature would be slightly under-estimated for DLAs with $N_{\text{HI}} < 1 \times 10^{21} \text{ cm}^{-2}$, and over-estimated for DLAs with $N_{\text{HI}} > 1 \times 10^{21} \text{ cm}^{-2}$.

All DLAs of the sample have HI column densities in the range $2 \times 10^{20} - 6.3 \times 10^{21} \text{ cm}^{-2}$. For absorbers at $z < 2$ (where the median transverse size of the radio core is ≈ 69 pc), the derived spin temperature would be within 10% of the “true” value for all N_{HI} values except the range $2 \times 10^{20} \text{ cm}^{-2} < N_{\text{HI}} < 5 \times 10^{20} \text{ cm}^{-2}$, where the derived T_s could be lower than the “true” value by up to a factor of 1.5. Conversely, for DLAs at $z > 2$ (where the median transverse size of the radio core is ≈ 350 pc), the derived T_s would be within 50% of the correct value for all N_{HI} values except for the range $N_{\text{HI}} = (2 - 4) \times 10^{20} \text{ cm}^{-2}$. For the latter range, the T_s estimate could be lower than the “true” value by up to a factor of 2.

The median HI column density of the present DLA sample is $N_{\text{HI}} \approx 6 \times 10^{20} \text{ cm}^{-2}$, with 23 absorbers having $N_{\text{HI}} \leq 1 \times 10^{21} \text{ cm}^{-2}$. Of the remaining 14 systems, twelve have $N_{\text{HI}} < 5.1 \times 10^{21} \text{ cm}^{-2}$ and should thus, on the average, have systematic errors lower than 25% on the spin temperature. There are thus only two absorbers, at $z = 1.9436$ towards 1157+014 and $z = 2.0395$ towards 0458-020, whose HI column densities are in the regime where the spin temperature might be over-estimated by $\approx 50\%$. Conversely, there are 10 DLAs in the sample with $N_{\text{HI}} < 4 \times 10^{20} \text{ cm}^{-2}$, seven of which are at $z > 2$, for which the spin temperature could be under-estimated, on the average, by using the optical N_{HI} in equation (3).

For clarity, we emphasize that the above statements are only valid in a statistical sense; it is certainly possible that the HI column densities along the radio and optical sightlines are very different in individual absorbers. However, on the average, the use of the HI column density derived from the Lyman- α profile is likely to result in *under-estimating* the spin temperature for most DLAs of the present sample, by up to a factor of two at the lowest HI column densities. The spin temperature is likely to be over-estimated for only a few DLAs with the highest N_{HI} values, $N_{\text{HI}} > 5 \times 10^{21} \text{ cm}^{-2}$.

7.4 HI 21cm optical depths, DLA spin temperatures and HI column densities

It is well known that the strength of the HI 21cm absorption in the Galaxy and M31 shows a rough power-law dependence on the HI column density (e.g. Braun & Walterbos 1992; Carilli et al. 1996; Kanekar et al. 2011). A similar trend has been seen in earlier studies of DLAs, using smaller samples and without covering factor measurements (Carilli et al. 1996; Kanekar & Chengalur 2001a). For the current sample of 37 DLAs, Fig. 15[A] shows the integrated HI 21cm optical depth ($\int \tau_{21\text{cm}} dV$), corrected for absorber covering factor, plotted against the HI column density N_{HI} . It is clear that the strength of the HI 21cm absorption does correlate with N_{HI} ; the correlation is detected at $\approx 3.8\sigma$ significance in a non-parametric generalized Kendall-tau test (Brown et al. 1974; Isobe et al. 1986).

Fig. 15[B] shows the spin temperature plotted versus HI column density for the 37 DLAs of the sample; no evidence is seen for a relation between the two quantities. We further tested whether the DLA spin temperatures are systematically different in absorbers with low and high HI column densities, below and above the median $N_{\text{HI}} \approx 6 \times 10^{20} \text{ cm}^{-2}$. A Peto-Prentice test finds that the spin temperature distributions of the sub-samples with N_{HI} values above and below the median are in agreement within $\approx 0.8\sigma$ significance.

We also considered the possibility that the N_{HI} values along

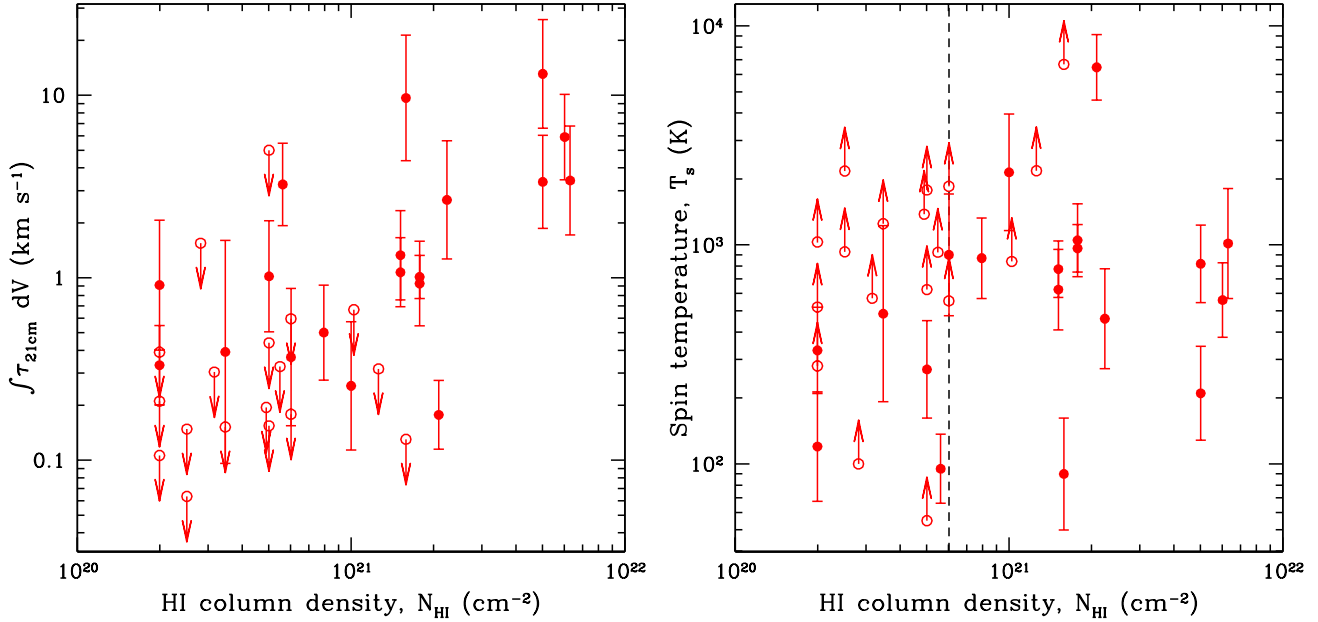


Figure 15. [A] (left panel) The integrated HI 21cm optical depth $\int \tau_{21\text{cm}} dV$, corrected for DLA covering factor, and [B] (right panel) the spin temperature T_s , plotted against the HI column density N_{HI} for the 37 DLAs of the sample. Non-detections of HI 21cm absorption are plotted as open circles, with arrows indicating upper limits to the HI 21cm optical depth and lower limits to the spin temperature. The dashed vertical line in the right panel indicates the median value of the HI column density, $N_{\text{HI}} \approx 6 \times 10^{20} \text{ cm}^{-2}$. See text for discussion.

the radio and optical sightlines might be somewhat different at low and high HI column densities, as inferred from the results in Section 7.3 for the LMC. This was done by using the ratio of the HI column densities measured along the high-resolution and the smoothed sightlines in the LMC (from Fig. 14) to convert the measured N_{HI} values towards the optical QSO to that towards the radio core. For DLAs at $z < 2$ and $z > 2$, we used the ratios measured at smoothed resolutions of 67 pc and 345 pc, respectively, in each case equal to the median size of the core at the DLA redshift. We also corrected the spin temperature for the new N_{HI} value. Again, no significant difference was obtained in the spin temperature distributions for the sub-samples with low and high HI column densities; the distributions agree at 1.4σ significance in a Peto-Prentice test.

We thus find no evidence that DLA spin temperatures have a systematic dependence on the HI column density (see also Srianand et al. 2012). Note that the spin temperatures of the Galactic sample also do not show a statistically significant dependence on the HI column density: a similar Peto-Prentice test finds that the Galactic spin temperature distributions above and below the median HI column density ($1.48 \times 10^{21} \text{ cm}^{-2}$) are in agreement within $\approx 1.3\sigma$ significance.

In order to consider whether the detection rate of HI 21cm absorption depends on HI column density, we restricted the sample to the 34 DLAs with either detections of HI 21cm absorption or strong lower limits on the spin temperature ($T_s > 500 \text{ K}$). This was done to avoid the possibility that our conclusions might be biased by DLAs with weak limits on the HI 21cm optical depth. The median HI column density of this sub-sample is $N_{\text{HI}} = 6 \times 10^{20} \text{ cm}^{-2}$. The detection rates of HI 21cm absorption are $\approx 81_{-22}^{+19}\%$ and $\approx 33_{-14}^{+23}\%$ for absorbers with HI column densities higher and lower than $6 \times 10^{20} \text{ cm}^{-2}$, respectively. While the detection rate appears higher in the high- N_{HI} sample, the difference has only 1.3σ

significance. At present, we find no statistically significant evidence that the detection rate of HI 21cm absorption in DLAs depends on the HI column density (although we note that this too might arise due to the relatively small size of the two sub-samples).

7.5 Redshift evolution of DLA spin temperatures

The high spin temperatures obtained in DLAs have been an issue of interest ever since the earliest studies of HI 21cm absorption in high- z DLAs (Wolfe & Davis 1979; Wolfe et al. 1981). There are two separate questions here: (1) whether DLA spin temperatures are systematically different from those measured in the Milky Way and local spiral galaxies, and (2) whether DLA spin temperatures evolve with redshift (i.e. whether low- z and high- z DLAs have different distributions of spin temperatures). While a number of studies have indicated that high- z DLAs tend to have higher spin temperatures than those seen in both low- z DLAs and the Galaxy (e.g. Carilli et al. 1996; Chengalur & Kanekar 2000; Kanekar & Chengalur 2001a, 2003; Srianand et al. 2012), the results have been uncertain due to a combination of small sample size and lack of covering factor measurements.

Fig. 16 shows the spin temperature plotted versus redshift for the 37 DLAs of our sample; the median absorber redshift is $z_{\text{med}} = 2.192$. We emphasize that all systems have estimates of the absorber covering factor and that this is by far the largest sample that has been used for such studies. There are 3 detections and 15 non-detections of HI 21cm absorption in DLAs at $z > 2.192$, and 15 detections and 3 non-detections of HI 21cm absorption in systems at $z < 2.192$. The detection fractions are $(17_{-9}^{+16})\%$ ($z > 2.192$) and $(83_{-21}^{+17})\%$ ($z < 2.192$). The detection fraction thus appears higher in the low- z sample, albeit only at $\approx 2.5\sigma$ significance (see also Kanekar et al. 2009b). However, a comparison between the two spin temperature distributions via a Peto-Prentice test finds that the

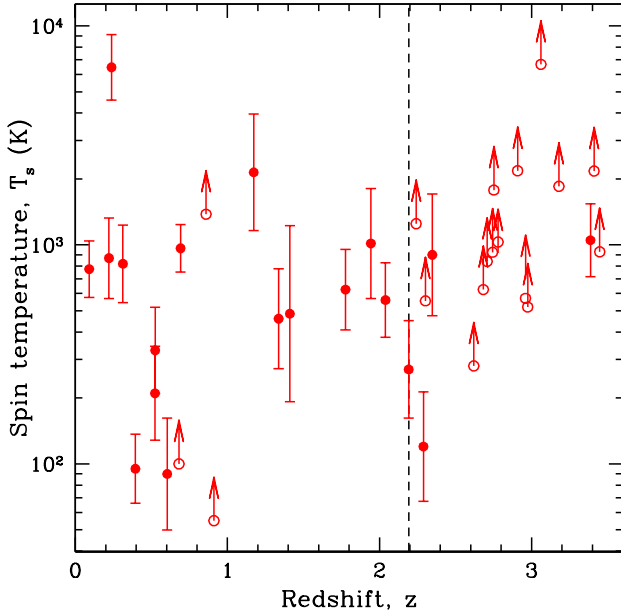


Figure 16. The spin temperature T_s plotted against redshift for the 39 DLAs (filled circles) and sub-DLAs (open stars) of the sample; non-detections of HI 21cm absorption are indicated by lower limits to the spin temperature. The median absorption redshift, $z_{med} = 2.192$, is indicated by the vertical dashed line. A generalized Wilcoxon two-sample test finds that the distributions of spin temperatures are different in the high- z and low- z sample; see text for discussion.

T_s distributions are different at $\approx 3.5\sigma$ significance. Note there is nothing special about the median redshift, $z = 2.192$, chosen to demarcate the high- z and low- z DLA sub-samples. For example, a comparison between the T_s distributions of absorber at redshifts above and below $z = 2.4$ (23 systems in the low- z sample and 14 in the high- z sample), yields a difference with 4.0σ statistical significance. We conclude that there is statistically-significant evidence for evolution in the spin temperatures of DLAs from high redshifts to low redshifts, with a larger fraction of low- T_s DLAs in the low redshift sample as well as a higher detection fraction at low redshifts.

It should be mentioned that DLAs in the low- z and high- z samples were not gathered via the same selection criteria. Most of the DLAs in the low- z sample were initially targeted due to the presence of strong MgII $\lambda 2796$ absorption in the quasar spectrum, with follow-up Lyman- α spectroscopy resulting in the detection of the DLA (e.g. Rao & Turnshek 1998, 2000; Rao et al. 2006; Ellison et al. 2012). Conversely, DLAs in the high- z sample were obtained from direct absorption surveys in the Lyman- α absorption line. While the MgII $\lambda 2796$ rest equivalent width is correlated with the absorber metallicity (Murphy et al. 2007), there is no evidence that the MgII $\lambda 2796$ selection criterion (at an MgII $\lambda 2796$ rest equivalent width threshold of 0.5; Rao et al. 2006) preferentially yields DLAs with higher metallicity. It thus appears unlikely that the different selection methods could give rise to differing spin temperature distributions in the low- z and high- z samples.

The distributions of HI column densities of the low- z and high- z DLA samples (again separated at the median redshift, $z = 2.192$) do show a weak difference in a Wilcoxon two-sample test (at $\approx 2.7\sigma$ significance). Histograms of the N_{HI} distributions of the low- z and high- z sub-samples are plotted in Fig. 11[B]. While it

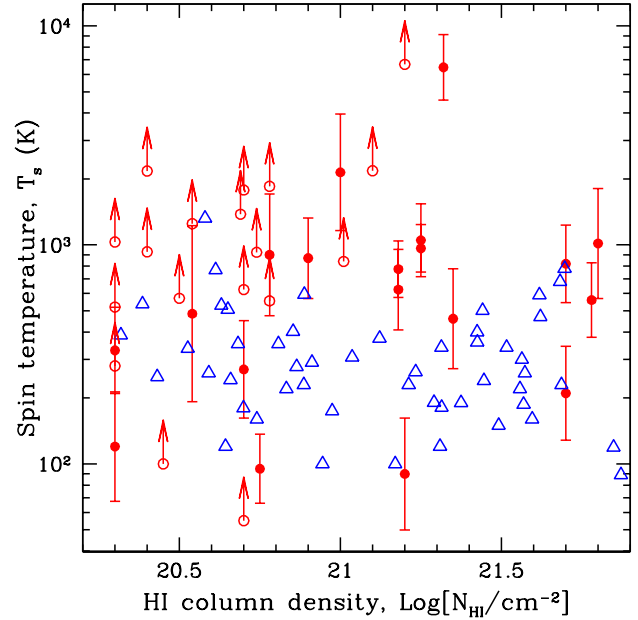


Figure 17. A comparison between the spin temperature distributions in the 37 DLAs of the full sample (filled circles) and sightlines in the Milky Way (open triangles), with both quantities plotted against HI column density. Note that the Milky Way spin temperatures were estimated by comparing HI 21cm emission and HI 21cm absorption studies on neighbouring sightlines, while the DLA spin temperatures were estimated by comparing the HI 21cm optical depth with the HI column density measured from the Lyman- α absorption profile. The figure shows that the majority of DLA spin temperature lie at or above the upper edge of the envelope of Galactic T_s values (see also; Carilli et al. 1996). Two-sample tests yield strong evidence that the spin temperature distributions in DLAs and in the Galaxy are very different.

should be noted that the sizes of the two sub-samples are small (with only 18 systems in each sub-sample), there appear to be more high- N_{HI} DLAs in the low- z sub-sample, and more low- N_{HI} DLAs in the high- z sub-sample. Since the strength of the HI 21cm absorption correlates with the HI column density, this could contribute to the larger fraction of detections of HI 21cm absorption in the low- z sample. However, this would be the case only if the HI 21cm studies were carried out at uniform optical depth sensitivity. In reality, the HI 21cm absorption studies have been targeted at detecting gas at high spin temperatures, by aiming for higher optical depth sensitivity in DLAs with lower HI column densities. It thus appears unlikely that the difference in HI column density distributions in the low- z and high- z DLA samples significantly influences the detection rates of HI 21cm absorption. Of course, it was shown in Section 7.4 that the spin temperature does not correlate with the HI column density, either in DLAs or in the Galaxy. The difference in HI column density distributions should hence also not yield a difference in the spin temperature distributions of the high- z and low- z samples.

Fig. 17 shows the spin temperatures of the 37 DLAs of the sample (filled circles) and the T_s values measured along 51 Galactic sightlines towards compact radio sources with $N_{HI} \geq 2 \times 10^{20} \text{ cm}^{-2}$ (open triangles) plotted versus HI column density; the Galactic data are from Colgan et al. (1988) and Kanekar et al. (2011). As was originally pointed out by Carilli et al. (1996) (albeit for integrated HI 21cm optical depths), the majority of the DLAs lie at or above

the upper edge of the distribution of the Galactic T_s values. While the HI column densities of the two samples are consistent with being drawn from the same distribution, a Peto-Prentice test finds that the distributions of spin temperatures in DLAs and the Galaxy are different at $\approx 6.0\sigma$ significance. We conclude that there is clear evidence that conditions in the neutral ISM in DLAs are very distinct from those measured along sightlines through the Galaxy, with significantly higher spin temperatures in most DLAs than are observed in the Milky Way.

7.6 Spin temperature or covering factor as the cause for T_s evolution ?

Curran & Webb (2006) have argued that the apparent difference in spin temperature distributions between low- z and high- z DLA samples arises mainly due to covering factor effects (see also Curran 2012). These authors argue that high- z DLAs are inefficient at covering the quasar radio emission because the angular diameter distances of the absorber (DA_{DLA}) and the quasar (DA_{QSO}) are essentially the same for DLAs at $z \gtrsim 1$. Conversely, low- z ($z < 1$) DLAs are typically more efficient at covering the radio emission because many low- z DLAs would have $DA_{\text{DLA}} < DA_{\text{QSO}}$ (Curran 2012).

As discussed in Section 7.2, our VLBA estimates of the covering factor have shown that the median upper limit to the transverse size of the radio core emission in DLAs at $z > 2$ is 350 pc. This is significantly lower than the size of even a dwarf galaxy, making it likely that all the core radio emission is covered in all cases: covering factor estimates should thus not be a serious issue for DLAs of the sample, especially since we have shown in Section 7.2 that the covering factor does not correlate with redshift. However, the increased sample size allows a simple test of whether the argument of Curran (2012), based on the similar angular diameter distances of foreground DLAs and background quasars, is indeed tenable. For this purpose, we restrict the base sample to the 25 DLAs at $z \gtrsim 1$, the redshift above which the angular diameter distances to both the foreground DLAs and the background quasars are roughly equal. We divide these 25 absorbers into two sub-samples with redshifts above and below the median redshift of DLAs with $z \gtrsim 1$ ($z_{\text{med}} = 2.683$), and compare the spin temperature distributions of the two sub-samples. Since all 25 DLAs have $DA_{\text{DLA}} \approx DA_{\text{QSO}}$, the issue of angular diameter distances cannot affect the results.

There are 12 DLAs each in the low- z ($1.0 < z < 2.683$) and high- z ($z > 2.683$) sub-samples (one absorber is at $z = 2.683$). The low- z sample has 9 detections and 3 non-detections of absorption, while the high- z sample has 11 non-detections and a single detection. We used a Peto-Prentice generalized Wilcoxon test to compare the spin temperature distributions (again appropriately taking into account the limits on T_s) and find that the two T_s distributions differ at $\approx 3.5\sigma$ significance. There are both far more non-detections and higher spin temperatures in the high- z DLA sample.

Thus the spin temperature distributions are clearly different even within the sub-sample of absorbers at $z \gtrsim 1$, i.e. with $DA_{\text{DLA}} \approx DA_{\text{QSO}}$. We conclude that angular diameter distances (and hence, DLA covering factors) do not play a significant role in the low HI 21cm optical depths measured in high- z DLAs, and that it is indeed the spin temperature that shows redshift evolution.

7.7 The CNM fraction in DLAs

As noted in Section 3, for sightlines containing a mixture of neutral gas in different temperature phases, the spin temperature derived

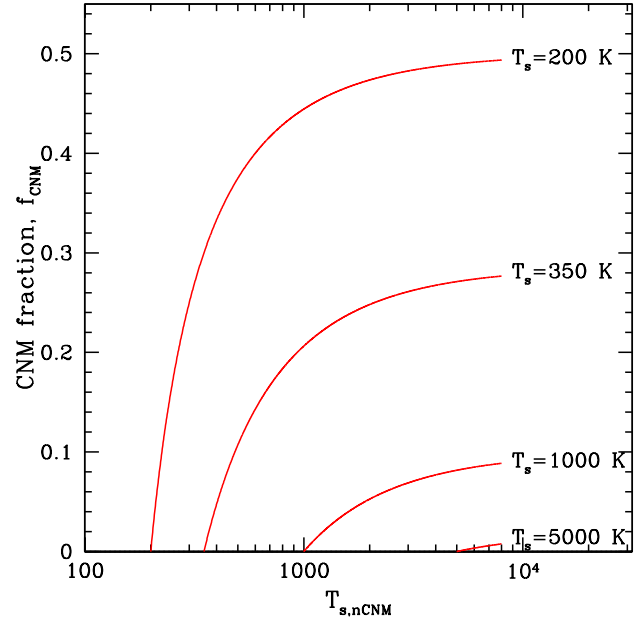


Figure 18. The CNM fraction plotted against the column-density weighted harmonic mean spin temperature of gas that is *not* in the CNM phase $T_{s,\text{nCNM}}$, for different DLA spin temperatures T_s and an assumed CNM spin temperature of 100 K. Note that the DLA spin temperature T_s is the value inferred from equation 3, when the possible multiphase nature of the gas is not taken into account. The *highest* CNM fraction is obtained when $T_{s,\text{nCNM}} = 8000$ K (not shown in the figure).

from equation (3) is the column-density-weighted harmonic mean of the spin temperatures of different phases. One can hence use the measured spin temperatures in DLAs and assumptions about the spin temperatures in different gas phases to estimate the fraction of cold (≤ 200 K) gas along each sightline.

For the standard two-phase medium models of the ISM in the Milky Way, the kinetic temperatures of the CNM and WNM are $\approx 40 - 200$ K and $\approx 5000 - 8000$ K, respectively (Field et al. 1969; Wolfire et al. 1995). While the actual temperature range depends on local conditions (e.g. the metallicity, pressure, the constituents of the ISM, etc), detailed studies have shown that typical CNM kinetic temperatures are ≈ 100 K in both the Milky Way and external galaxies like M31 (e.g. Braun & Walterbos 1992; Heiles & Troland 2003). Further, the high densities in the CNM imply that the HI 21cm hyperfine transition is thermalized by collisions and the spin temperature in the CNM is hence approximately equal to the kinetic temperature (e.g. Field 1959; Liszt 2001).

On the other hand, there are few reliable estimates of the gas kinetic temperature in the WNM, even in the Milky Way, and there is even evidence that significant amounts of gas are in the unstable phase (e.g. Heiles & Troland 2003; Kanekar et al. 2003). In DLAs, there have so far been two estimates of the WNM kinetic temperature, in the $z = 0.0912$ and $z = 0.2212$ DLAs towards 0738+313: Lane et al. (2000) obtained $T_k \approx 5500$ K in the former system, while Kanekar et al. (2001) measured $T_k \approx 7600$ K in the latter, both in agreement with the temperature ranges predicted by the two-phase models. Note that the spin temperature is expected to be lower than the kinetic temperature in the WNM, as the low gas density in WNM implies that collisions are insufficient to thermalize the HI 21cm line here (e.g. Liszt 2001).

Kanekar & Chengalur (2003) and Srianand et al. (2012) as-

sumed specific values for the CNM and WNM spin temperatures in order to infer the CNM fraction in their absorber samples. However, while it is reasonable to assume that the CNM spin temperature is equal to its kinetic temperature, this assumption is unlikely to be valid for the WNM. Given this, we will use a conservative approach to estimating the fraction of cold gas in the DLAs of our sample. We assume that each DLA contains some fraction of neutral gas (f_{CNM}) in the CNM phase and that the remaining gas is not in the CNM phase but at higher kinetic temperatures, with a fraction $f_{\text{nCNM}} = 1 - f_{\text{CNM}}$. Note that both fractions include gas at different kinetic (and spin) temperatures, in the range $T_s \approx T_k = 40 - 200$ K for the CNM and at higher temperatures for the remaining gas in the non-CNM phase. We also assume that the column-density weighted harmonic mean spin temperature in the CNM is $T_{s,\text{CNM}} \approx 100$ K (the results do not change significantly if one assumes a higher CNM spin temperature, ≈ 200 K). This allows us to rewrite equation (4) for the measured DLA spin temperature as

$$\frac{1}{T_s} = \frac{f_{\text{CNM}}}{100} + \frac{1 - f_{\text{CNM}}}{T_{s,\text{nCNM}}}, \quad (5)$$

where T_s is the DLA spin temperature and $T_{s,\text{nCNM}}$ is the column-density weighted harmonic mean spin temperature for the gas that is *not* CNM. One then obtains

$$f_{\text{CNM}} = \left[\frac{1}{(T_{s,\text{nCNM}}/100) - 1} \right] \left[\frac{T_{s,\text{nCNM}}}{T_s} - 1 \right]. \quad (6)$$

Fig. 18 shows the CNM fraction f_{CNM} plotted against $T_{s,\text{nCNM}}$ for different values of the DLA spin temperature, T_s . It is clear that, for a given DLA spin temperature, the *highest* value of f_{CNM} will be obtained when $T_{s,\text{nCNM}}$ is large. We can thus obtain an upper limit on the CNM fraction for each DLA by assuming $T_{s,\text{nCNM}} = 8000$ K in equation (6), along with the DLA spin temperature. Note that this is equivalent to assuming that all the remaining (non-CNM) gas is in the WNM, with $T_s = 8000$ K. This is a stringent assumption for two reasons: (1) 8000 K is the upper limit of the range of stable WNM kinetic temperatures (Wolfire et al. 1995), and (2) the spin temperature is expected to be lower than the kinetic temperature in the WNM (Liszt 2001).

Fig. 19 shows the CNM fraction estimated from the above approach plotted versus DLA redshift for the 37 DLAs of the full sample. The downward arrows in the figure indicate non-detections of HI 21cm absorption, and thus lower limits on the DLA spin temperature and upper limits on the CNM fraction. The figure shows that the CNM fractions in DLAs are typically quite low, $\lesssim 20\%$, at all redshifts, with only a few absorbers having comparable CNM and WNM fractions. At high redshifts, $z > 1.7$, only two of the 23 absorbers have CNM fractions greater than 27%, with one of the upper limits also in this range. This is significantly lower than the CNM fraction along Galactic sightlines, where the median CNM fraction is $\approx 27\%$ (Heiles & Troland 2003). We emphasize further that every point in Fig. 19 is an *upper* limit to the CNM fraction in a DLA, due to the assumption that gas in the non-CNM phase has $T_{s,\text{nCNM}} = 8000$ K. We conclude that the CNM fractions in high- z DLAs are significantly lower than those typical of the Galaxy. Similar conclusions have been drawn based on smaller HI 21cm absorption samples by Kanekar & Chengalur (2003), Srianand et al. (2012) and Ellison et al. (2012), and from H₂ absorption studies by Petitjean et al. (2000).

We note that three of the four low- z absorbers with $f_{\text{CNM}} \geq 0.27$ have been identified with spiral galaxies; these are the DLAs at $z = 0.3950$ towards 1229–021 ($f = 1$), $z = 0.5242$ towards 0235+164 ($f = 0.47$), and $z = 0.5247$ towards 0827+243 ($f =$

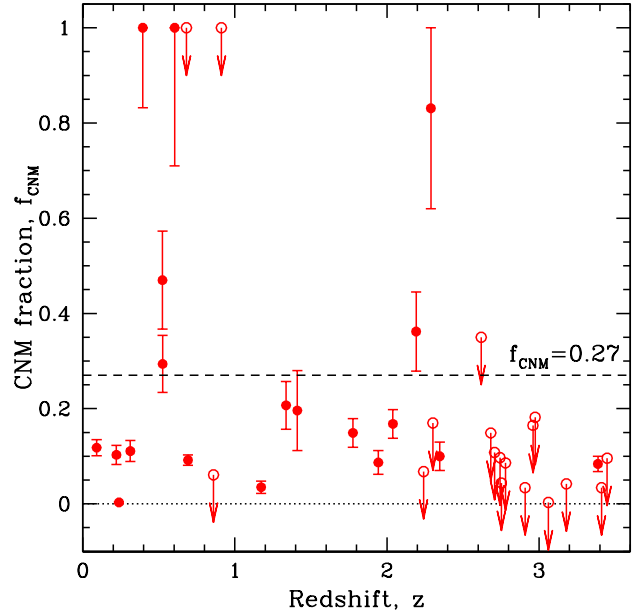


Figure 19. The CNM fraction plotted against redshift for the 37 DLAs of the sample (i.e. excluding the two sub-DLAs); the dashed horizontal line shows the median CNM fraction in the Galaxy ($f_{\text{CNM}} = 0.27$). The column-density weighted harmonic mean spin temperatures are assumed to be 100 K in the CNM and 8000 K in the non-CNM phases; this ensures that the derived CNM fraction is an upper limit to the “true” CNM fraction. The majority of DLAs, especially at high redshifts, have low CNM fractions, $\lesssim 20\%$.

0.294; le Brun et al. 1997; Burbidge et al. 1996; Chen et al. 2005). We suggest that the fourth system, at $z = 0.6019$ towards 1429+400 ($f = 1$; Ellison et al. 2012), as well as the two high-CNM absorbers at $z \sim 2.192$ towards 2039+187 ($f = 0.36$; Kanekar et al. 2013) and $z \sim 2.2890$ towards 0311+430 ($f = 0.83$; York et al. 2007) are also likely to be bright disk galaxies. Imaging studies of these DLAs would be of much interest.

7.8 DLA spin temperatures, metallicities and dust depletions

The results of the preceding sections have shown that the majority of DLAs at all redshifts have higher spin temperatures and lower CNM fractions than typically seen in the Milky Way and M31 (e.g. Colgan et al. 1988; Braun & Walterbos 1992; Kanekar et al. 2011), due to lower fractions of the cold phase of neutral hydrogen. In the ISM, collisional excitation of the fine-structure lines of metals like CII and OI dominates the cooling below temperatures of ≈ 8000 K (Launay & Roueff 1977; Wolfire et al. 1995). Galaxies with low metallicities would then be expected to have fewer cooling routes than high-metallicity systems like the Milky Way, and hence larger amounts of warm gas. For example, Fig. 6 of Wolfire et al. (1995) shows that, at lower metallicities, a higher central pressure is needed to produce the cold phase of HI. Kanekar & Chengalur (2001a) used this to argue that the high spin temperatures in most high- z DLAs could be naturally explained if the absorbers are typically low-metallicity systems with low CNM fractions due to a lack of cooling routes. Conversely, DLAs with high metallicities would be expected to have higher CNM fractions and low spin temperatures. Kanekar & Chengalur (2001a) hence predicted an anti-correlation between spin temperature and metallicity, if metallicity

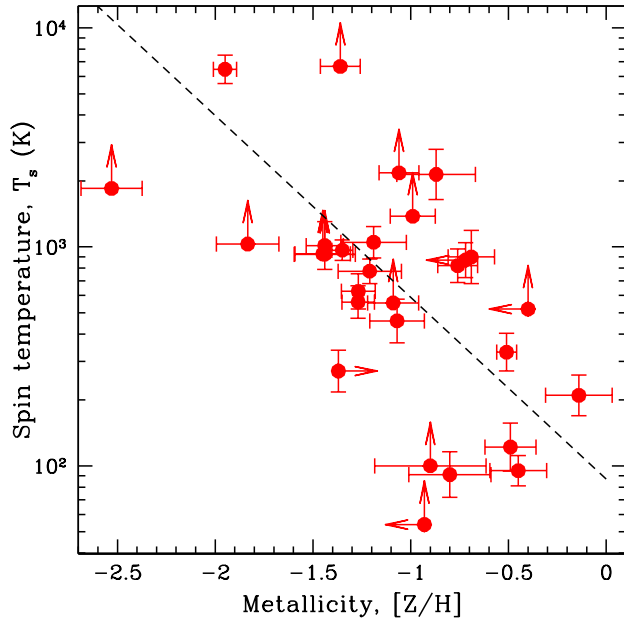


Figure 20. The spin temperature T_s plotted against metallicity $[Z/H]$ for the 29 DLAs of the full sample that have measurements of both quantities. The dashed line shows the linear regression fit, $\text{Log}[T_s] = (-0.83 \pm 0.16) \times [Z/H] + (1.94 \pm 0.20)$, to the 16 measurements of both T_s and $[Z/H]$.

is indeed the dominant cause in determining the cold gas content of a galaxy.

A test of this hypothesis was first carried out by Kanekar et al. (2009c) Kanekar & Chengalur (see also 2005), who used T_s and $[Z/H]$ data on 26 DLAs (including limits) to detect the predicted anti-correlation at 3.6σ significance, via a non-parametric generalized Kendall test (Brown et al. 1974; Isobe et al. 1986). The anti-correlation was detected at lower significance ($\approx 3\sigma$) in a sub-sample of 20 systems with estimates of the covering factor. Ellison et al. (2012) extended this study to 26 DLAs and sub-DLAs with covering factor estimates, using some of the new data presented in this paper; this improved the detection significance of the anti-correlation to $\approx 3.4\sigma$. Recently, Srianand et al. (2012) examined the possibility of redshift evolution in the relation between T_s and $[Z/H]$, but found no evidence in support of this, perhaps due to the small size of their sample.

Three of the DLAs in this paper have new VLBA estimates of the covering factor, while the detection of HI 21cm absorption at $z = 2.192$ towards 2039+187 has recently been presented by Kanekar et al. (2013). These systems were not included in the analysis of Ellison et al. (2012). We have also in this paper obtained more accurate estimates of the metallicities of the $z = 0.3127$ and $z = 0.5247$ DLAs towards 1127–145 and 0827+243, respectively. The sample of DLAs with estimates (including limits) of T_s and $[Z/H]$, as well as measurements of the low-frequency covering factor now contains 29 systems. Fig. 20 shows the spin temperature T_s plotted against metallicity $[Z/H]$ for this sub-sample. We have used the generalized Kendall-tau rank correlation test (the BHK statistic; Brown et al. 1974) to detect the anti-correlation between T_s and $[Z/H]$ at $\approx 3.5\sigma$ significance, somewhat higher than the result of Ellison et al. (2012). We emphasize that this is a non-parametric test that also takes into account the presence of limits in the sample.

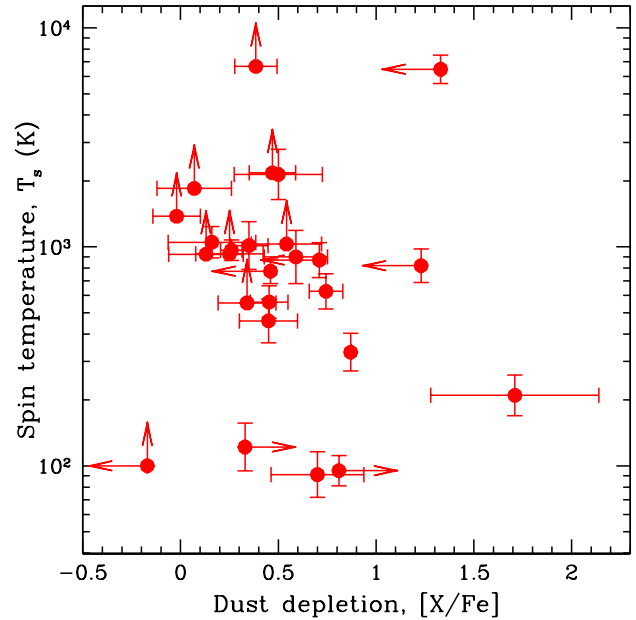


Figure 21. The spin temperature T_s plotted against dust depletion $[X/Fe]$ for the 26 DLAs with low-frequency covering factor estimates that have measurements of both quantities. Only weak evidence is found for an anti-correlation between T_s and $[X/Fe]$.

Further, unlike Ellison et al. (2012), we have excluded sub-DLAs from the present analysis.

We also tested whether either the high- z or the low- z DLA sub-samples dominate the detected anti-correlation between metallicity and spin temperature. The median redshift of the 29 DLAs with estimates of both metallicity and spin temperature is $z = 1.7763$, with 14 DLAs each in the low- z and high- z sub-samples. The anti-correlation between T_s and $[Z/H]$ is detected at 2.3σ and 2.2σ significance in the low- z and high- z sub-samples, respectively. A similar statistical significance (2.2σ) is obtained for the anti-correlation even on restricting the sample to the 12 DLAs at $z < 1$. This indicates that the anti-correlation is not dominated by either the low- z or the high- z DLAs. Specifically, the high- z DLAs, where the covering factor is more uncertain, do not dominate the anti-correlation.

The dashed line in Fig. 20 shows an update of the linear fit of Ellison et al. (2012) to the T_s - $[Z/H]$ relation. This uses a regression analysis based on the BCES(Y/X) estimator (Akritas & Bershady 1996), with $[Z/H]$ as the independent variable, X, applied to the 16 DLAs with measurements of *both* T_s and $[Z/H]$ (Kanekar et al. 2009c; Ellison et al. 2012). We obtain $\text{Log}[T_s] = (-0.83 \pm 0.16) \times [Z/H] + (1.94 \pm 0.20)$, essentially the same as the fit of Ellison et al. (2012). Note that the sample used for the latter regression analysis included the $z = 1.6724$ sub-DLA towards 0237–233.

We have also examined the sample for a relation between T_s and dust depletion $[X/Fe]$. 26 DLAs with covering factor measurements also have estimates of both quantities (cf. 23 DLAs and sub-DLAs in Ellison et al. 2012). Fig. 21 plots the spin temperature against dust depletion for this sub-sample. We find only weak evidence for an anti-correlation between T_s and $[X/Fe]$; this is detected at $\approx 2.4\sigma$ significance. As argued by Kanekar et al. (2009c) and Ellison et al. (2012), it does not appear that the anti-correlation between T_s and metallicity is due to an underlying relation between T_s and dust depletion.

We find no evidence that the probability of detecting HI 21cm absorption depends on the absorber metallicity. For the 25 DLAs with measurements of metallicity (i.e. excluding absorbers with only limits on the metallicity), the median metallicity is $[Z/H]_{med} = -1.09$. The HI 21cm detection rates are $75^{+25}_{-25}\%$ and $54^{+29}_{-20}\%$ for systems above and below the median metallicity, consistent within 1σ confidence intervals.

In passing, we note that the above analysis has used the X-ray metallicity estimate for the $z = 0.524$ DLA towards QSO 0235+164. As discussed in Ellison et al. (2012), excluding this DLA from the sample does not significantly affect the significance of the anti-correlation between metallicity and spin temperature.

Note that the DLA spin temperatures have been estimated under the assumptions that (1) the HI column density measured along the optical sightline is the same as that towards the radio core, and (2) the quasar core fraction can be interpreted as the DLA covering factor. Conversely, the DLA metallicities have been estimated from the optical spectra alone, without any such assumptions. Any breakdown in the assumptions (e.g. due to differences in the HI column densities along the optical and radio sightlines) should weaken any underlying relation between T_s and $[Z/H]$. The fact that the predicted anti-correlation between T_s and $[Z/H]$ is yet detected in a non-parametric test indicates that such differences between the optical and radio sightlines are very unlikely to give rise to the high spin temperatures seen in the majority of high- z DLAs. We conclude that the assumptions regarding the HI column density and the DLA covering factor are likely to be reliable, at least in a statistical sense (unless the observed anti-correlation is mere coincidence).

7.9 On the assumption that the covering factor is equal to the core fraction

The results in Sections 7.5–7.8 are based on the assumption that the DLA covering factor is equal to the radio core fraction. While the measured radio core sizes are quite small, < 1 kpc, far smaller than the size of a typical absorbing galaxy, it is possible that this assumption is violated for at least some DLAs of the sample. Further, it is also possible that any detected HI 21cm absorption might arise against extended radio structure and not against the radio core; in such a situation, the covering factor would be uncorrelated with the core fraction. Unfortunately, it is very difficult to directly measure the covering factor of individual DLAs. In this section, we hence use Monte Carlo simulations to test whether our results critically depend on the assumption that the covering factor is equal to the core fraction.

We first considered the possibility that the covering factor is indeed statistically equal to the core fraction, but that there is a random error associated with each covering factor estimate. We assume that this error is normally distributed with a standard deviation equal to 10%, 20%, 50% and 100% of the measured core fraction. For each assumed standard deviation, we randomly select values of f (constrained to be in the range $0 < f \leq 1$), re-compute the spin temperature, and use the Kendall-tau test to estimate the significance of the anti-correlation between metallicity and spin temperature, and the Peto-Prentice test to determine the significance of the redshift evolution of the spin temperature, as done in Sections 7.8 and 7.5, respectively. The process was repeated over 10,000 Monte Carlo runs for each assumed standard deviation, and we then computed the mean statistical significance of the anti-correlation between T_s and $[Z/H]$ and of the redshift evolution in T_s over each set of 10,000 runs. We found that the significance of both results

remains high, even if the error on the covering factor has a 50% standard deviation. Specifically, for a standard deviation of 50%, the anti-correlation between T_s and $[Z/H]$ is detected at $\approx 3.2\sigma$ significance, while the difference in the T_s distributions in high- z and low- z samples (separated at the median redshift, $z_{med} = 2.192$) has $\approx 3.3\sigma$ significance. Indeed, even allowing for a 100% error in the covering factor only reduces the significance of the anti-correlation between T_s and $[Z/H]$ to 2.7σ , not a very strong effect, while the difference in T_s distributions has $\approx 3.2\sigma$ significance. We conclude that even a large random error in the inferred covering factor does not significantly affect our results.

We also considered the worst-case scenario in which the covering factor is entirely uncorrelated with the measured radio core fraction. Since the covering factor must take values between 0 and 1, we randomly selected values for f in this range (assuming a uniform distribution between 0 and 1), independently for each DLA of the sample, and then re-computed the spin temperature for each DLA. We then repeated the Monte Carlo simulations for the anti-correlation between spin temperature and metallicity and the redshift evolution of the spin temperature (following the approach described in the previous paragraph), with the mean statistical significance of the two relations again computed from 10,000 Monte Carlo runs. The anti-correlation between T_s and $[Z/H]$ is then detected at $\approx 2.9\sigma$ significance, while the difference between the spin temperature distributions in the high- z and low- z DLA samples (again separated at the median redshift, $z_{med} = 2.192$) has $\approx 3.1\sigma$ significance, averaging over 10,000 Monte Carlo runs. Again, while the significances of both results are somewhat lower than the values obtained on using the assumption that the covering factor is equal to the core fraction ($\approx 3.5\sigma$ for the T_s - $[Z/H]$ relation and $\approx 3.5\sigma$ for the redshift evolution in T_s ; see Sections 7.5 and 7.8), it is clear that there is no significant change in the results even on assuming an entirely random distribution of DLA covering factors.

We also used the above Monte Carlo simulations to examine the effect of systematic biases in the covering factor. We find that if all DLAs have low (or high) covering factors, our two main results (the anti-correlation between T_s and $[Z/H]$ and the redshift evolution of T_s) remain unchanged. The only way to reduce the statistical significance of the T_s - $[Z/H]$ anti-correlation is to assign very low covering factors ($f < 0.1$) to DLAs with high inferred spin temperatures, so as to effectively reduce the derived T_s . This is essentially similar to the argument of Curran & Webb (2006), that low DLA covering factors due to geometric effects can account for the inferred high DLA spin temperatures. However, as discussed in Section 7.6, there is statistically significant evidence for redshift evolution in the spin temperature even when we only consider the sub-sample of DLAs at $z > 1$, for which geometric effects cannot yield different DLA covering factors. As such, the result that the spin temperature of DLAs shows evidence of redshift evolution remains unaffected by the possibility that high- z DLAs are less effective at covering the background quasars.

Further, if low covering factors of high- z DLAs are the cause of the anti-correlation between metallicity and spin temperature, we would expect that the anti-correlation would be detected at higher significance in the high- z DLA sample. As discussed in Section 7.8, this is not the case, with the low- z and high- z sub-samples making roughly equal contributions to the significance of the anti-correlation.

We conclude that our results do not significantly depend on the assumption that the DLA covering factors are equal to the quasar

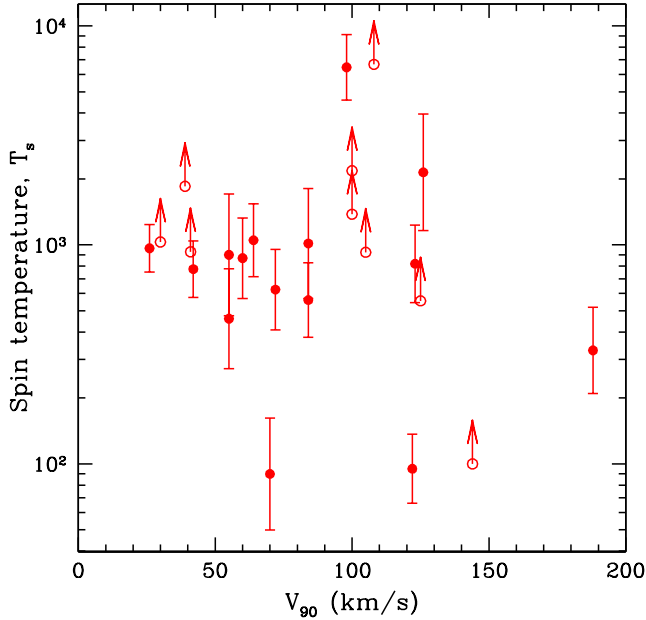


Figure 22. The spin temperature T_s plotted against velocity width at 90% optical depth in the low-ionization metal lines, ΔV_{90} , for the 25 DLAs (filled circles) and sub-DLAs (open star) with estimates of both quantities. The figure shows no evidence for a relation between T_s and ΔV_{90} .

radio core fractions. We also find no evidence that our results might be affected by systematic biases in the covering factor.

7.10 DLA spin temperatures and velocity widths

DLA metallicities have been shown to be correlated with the velocity spreads of low-ionization metal lines (Wolfe & Prochaska 1998; Ledoux et al. 2006; Prochaska et al. 2008), as well as with the rest equivalent widths of the MgII $\lambda 2796$ and SiII $\lambda 1526$ lines (Murphy et al. 2007; Prochaska et al. 2008). We hence examined the possibility that the anti-correlation between spin temperature and metallicity might arise because the spin temperature depends on the velocity spread of the absorber.

Our sample contains ΔV_{90} measurements for 24 DLAs, with a median ΔV_{90} value of 84 km s^{-1} . The detection rates of HI 21cm absorption are $45^{+31}_{-20}\%$ and $73^{+27}_{-25}\%$ for systems with ΔV_{90} values above and below the median, respectively. We thus find no evidence that the detection rate of HI 21cm absorption depends on the velocity spread of the low-ionization metal lines.

Fig. 22 plots the spin temperature against the 90% optical depth velocity spread ΔV_{90} for the 24 DLAs with estimates of both quantities. The figure resembles a scatter plot, with no obvious relation between the two quantities. Similarly, the generalized Kendall-tau test (taking limits into account) finds no evidence of a correlation between T_s and ΔV_{90} (0.2σ statistical significance). We conclude that it is very unlikely that the observed correlation between T_s and metallicity arises due to an underlying relation between the spin temperature and the velocity spread of the low ionization metal lines.

The correlation between metallicity and velocity spread in DLAs has usually been interpreted in terms of a mass-metallicity relation (Ledoux et al. 2006), similar to those observed in the local Universe or in bright high- z galaxies (e.g. Tremonti et al. 2004;

Erb et al. 2006; Prochaska et al. 2008; Neeleman et al. 2013). Since high-mass galaxies have higher central pressures, they are expected to have higher CNM fractions (Wolfire et al. 1995). It might then appear curious that no relation is seen between T_s and ΔV_{90} . While the sample size of systems with ΔV_{90} estimates is relatively small (24 systems), the anti-correlation between spin temperature and metallicity is detected at 3.6σ significance with a similar number of systems (29). We surmise that this is because the metallicity directly determines the number of cooling routes and hence the cold gas fraction. Conversely, it is clear that there are other contributors besides mass to the observed ΔV_{90} in absorption. For example, high mass galaxies observed at low inclinations to the line of sight can have low velocity spreads in absorption; DLA surveys may have some bias towards such systems, due to their larger surface area on the sky. There are also contributions to the velocity spread from merging galaxies, outflows from galactic winds, galactic infall, etc, which can increase ΔV_{90} for low-mass galaxies above the values expected due to rotation. For galaxies in the local Universe, where the mass can be estimated directly, Zwaan et al. (2008) find only a weak relation between ΔV_{90} and mass. Finally, the relation between $[Z/H]$ and ΔV_{90} itself has a large spread, ≈ 1.5 dex in metallicity at a given ΔV_{90} (see Fig.6[A] of Prochaska et al. 2008). It is hence perhaps not very surprising that the observed spin temperature does not depend strongly on the velocity spread of the absorbing galaxy.

7.11 Comparisons with results from CII* absorption studies

Over the last decade, it has been suggested that the strength of CII* $\lambda 1335.7$ absorption provides a means of distinguishing between DLAs containing significant CNM fractions and ones whose neutral phase is dominated by the WNM (Wolfe et al. 2003, 2004). This is because the most important coolant of the neutral ISM is the [CII]- $158\mu\text{m}$ line (e.g. Pottasch et al. 1979; Wright et al. 1991; Wolfire et al. 1995). Since this arises from transitions between the $^2P_{3/2}$ and $^2P_{1/2}$ levels in the ground state of ionized carbon, it should be possible to determine the cooling rate per H atom by measuring the abundance in the [CII] $^2P_{3/2}$ state from the strength of the UV CII* $\lambda 1335.7$ line (Pottasch et al. 1979). Assuming thermal balance then allows one to infer the heating rate from the cooling rate: for the CNM, where the cooling is dominated by the [CII]- $158\mu\text{m}$ line, the heating rate is approximately equal to the cooling rate, while, for the WNM, the heating rate is significantly larger than the derived cooling rate. Since the heating rate is dominated by photoelectric emission of electrons from grains by incident far-UV radiation (Bakes & Tielens 1994), Wolfe et al. (2003) argued that one could use this heating rate in conjunction with measurements of the dust-to-gas ratio in DLAs and an assumed grain photoelectric heating efficiency to infer the SFR per unit area in high- z DLAs. This could further be used to probe the distribution of neutral gas between the CNM and WNM phases, by assuming two-phase models in pressure equilibrium (Field et al. 1969; Wolfire et al. 1995, 2003).

Wolfe et al. (2003) considered two models for the neutral ISM, a “pure-WNM” model with all the HI in the WNM and a “CNM+WNM” model in which comparable amounts of HI are in each phase. They find that “pure-WNM” models are ruled out for DLAs with strong CII* $\lambda 1335.7$ absorption, as the bolometric luminosities of such DLAs would be far higher than observed values (see also Wolfe et al. 2003, 2004). The “pure-WNM” model was found to be applicable to absorbers with low CII* $\lambda 1335.7$ column densities (i.e. either non-detections of CII* $\lambda 1335.7$ absorption or weak CII* $\lambda 1335.7$ absorbers). About half the DLAs in the sam-

Table 6. DLAs with HI 21cm and CII* λ 1335.7 or H₂ absorption studies.

QSO	z_{QSO}	z_{abs}	$\log[N_{\text{HI}}/\text{cm}^{-2}]$	$\log[l_c/\text{ergs}^{-1}\text{H}^{-1}]$	[Z/H]	T_s K	$\log[f_{\text{H2}}]$
DLAs with HI 21cm and CII*λ1335.7 absorption studies							
0201+113	3.639	3.3869	21.25 ± 0.07	-26.66 ± 0.14	-1.19 ± 0.17	1050 ± 175	-4.6 to -6.2
0336-017	3.197	3.0621	21.20 ± 0.10	-26.71 ± 0.10	-1.36 ± 0.10	> 8890	< -6.90
0458-020	2.286	2.0395	21.78 ± 0.07	> -26.37	-1.269 ± 0.072	560 ± 95	< -6.40
1157+014	2.000	1.9436	21.80 ± 0.07	> -26.51	-1.440 ± 0.086	1015 ± 255	< -6.65
1331+170	2.084	1.7764	21.18 ± 0.07	< -27.12	-1.268 ± 0.076	625 ± 115	-1.25 ± 0.05
1354-170	3.147	2.7799	21.30 ± 0.15	-27.06 ± 0.16	-1.83 ± 0.16	> 1030	–
2342+342	3.053	2.9084	21.10 ± 0.10	-26.92 ± 0.12	-1.06 ± 0.10	> 2200	< -6.19
DLAs with HI 21cm and H₂, but no CII*λ1335.7, absorption studies							
0335-122	3.442	3.1799	20.78 ± 0.11	–	-2.53 ± 0.16	> 1850	< -5.10
0432-440	2.649	2.3023	20.78 ± 0.11	–	-1.09 ± 0.13	> 555	< -5.15
1418-064	3.689	3.4482	20.40 ± 0.10	–	-1.45 ± 0.14	> 930	< -5.69

References: The H₂ fractions are from Cui et al. (2005), Noterdaeme et al. (2008) and Srianand et al. (2012), while the $\log[l_c]$ values are from Wolfe et al. (2008). References for the metallicities, HI column densities and spin temperatures are given in Table 4. Note that PDLAs (e.g. the $z = 2.8111$ system towards 0528–250) have not been included in the table.

ple of Wolfe et al. (2008) lie in this category. Wolfe et al. argue that the observed strong CII* λ 1335.7 absorption in the remaining DLAs must arise in the CNM and that the “CNM+WNM” model is applicable here. Finally, Wolfe et al. (2008) argue that the CII 158 μm cooling rate per hydrogen atom l_c may be a separator of DLAs into two categories, “high-cool” systems with high cooling rates $l_c > 10^{-27} \text{ erg s}^{-1} \text{ H}^{-1}$ (with high metallicities, large velocity spreads and significant CNM fractions) and “low-cool” systems with low cooling rates $l_c < 10^{-27} \text{ erg s}^{-1} \text{ H}^{-1}$ (with low metallicities, low velocity spreads and with the HI mostly in the WNM phase).

With regard to HI 21cm studies, Wolfe et al. (2003) noted that there are two high- z DLAs with non-detections of HI 21cm absorption and high inferred lower limits on the spin temperatures, but which show strong CII* λ 1335.7 absorption: these are the systems at $z = 3.0621$ towards 0336–017 and $z = 3.387$ towards 0201+113. Wolfe et al. (2003) suggested that both systems are likely to have high CNM fractions ($\approx 50\%$) along the sightline to the optical QSO; they argued that the high spin temperature limits obtained from the HI 21cm absorption studies might arise because the relatively small (10 – 20 pc) CNM clouds do not entirely cover even the radio quasar core, which is significantly more extended than the optical quasar in both cases. Later, Kanekar et al. (2007) detected HI 21cm absorption towards 0201+113 (see also Briggs et al. 1997) and also found that the radio quasar core here has a transverse size of ≤ 286 pc. This implies that it is possible that the CNM clouds do not fully cover the radio core, as suggested by Wolfe et al. (2003). However, Kanekar et al. (2007) also showed that the CNM fraction towards the radio quasar core is $\leq 17\%$, even if one assumes that the sightline towards the optical core has a far higher CNM fraction, $\approx 50\%$. Thus, even if the arguments of Wolfe et al. (2003) are correct and the 10 – 20 pc-sized CNM clouds do not efficiently cover the radio core, the sightline towards the radio core is still dominated by the WNM, with $> 80\%$ of the HI in this phase.

For clarity, the upper part of Table 6 summarizes the CII* λ 1335.7 and HI 21cm results for the subset of DLAs with studies in both transitions and VLBI estimates of the covering factor. The columns in this table are: (1) the quasar name, (2) the quasar redshift z_{QSO} , (3) the DLA redshift, (4) the HI column density, (5) the CII 158 μm cooling rate per atom, $\log[l_c]$, inferred from the CII* λ 1335.7 line strength (Wolfe et al. 2008), (6) the metallicity, [Z/H], (7) the spin temperature T_s , (8) the CNM fraction, assum-

ing $T_{s,\text{CNM}} = 100$ K and $T_{s,\text{WNM}} = 8000$ K, and (9) the H₂ fraction (Ledoux et al. 2003; Noterdaeme et al. 2008). Based on the classification of Wolfe et al. (2008), the absorbers towards 1354–170 and 1331+170 are “low-cool” systems ($\log[l_c/\text{ergs}^{-1}\text{H}^{-1}] \leq -27$), while those towards 0201+113, 0336–017, 0458–020, 1157+014 and 2342+342 are “high-cool” systems ($\log[l_c/\text{ergs}^{-1}\text{H}^{-1}] > -27$). Note that the systems towards 1354–170 and 2342+342 are consistent with both categories, within 1σ errors, but are definitely not strong CII* λ 1335.7 absorbers.

At the outset, it is relevant to note that the CII* λ 1335.7 and HI 21cm absorption results appear in reasonable agreement for about half the DLA sample, the systems with weak or undetected CII* λ 1335.7 absorption (i.e. the “low-cool” systems). Wolfe et al. (2008) find that these systems have systematically lower metallicities (and dust-to-gas ratios and velocity widths) than the “high-cool” systems that have strong CII* λ 1335.7 absorption, and conclude that the neutral gas here is predominantly WNM. The anti-correlation between metallicity and spin temperature would lead us to conclude that such DLAs have high spin temperatures and are thus dominated by the WNM; there is thus no disagreement between the CII* λ 1335.7 and HI 21cm results for systems with weak CII* λ 1335.7 absorption and high spin temperatures. These include the DLAs at $z = 2.7799$ towards 1354–170 and $z = 2.9084$ towards 2342+342, for which both the relatively weak CII* λ 1335.7 absorption and the high spin temperatures are consistent with most of the HI being in the WNM.

The primary difference between the results on the CNM fractions obtained from the CII* λ 1335.7 and HI 21cm absorption studies are for the “high-cool” sample of Wolfe et al. (2008). However, the apparent discrepancy appears mainly due to the fact that Wolfe et al. (2003) (and later works) only consider two models, “CNM+WNM”, with half the HI in the CNM phase and the other half in the WNM, and “pure-WNM”, with all the HI in the WNM, and rule out the latter model, based on the fact that the CII* λ 1335.7 absorption must arise from the CNM. But even if one accepts that all the CII* λ 1335.7 absorption arises from the CNM (although see Srianand et al. 2005), this does not imply that half the HI must be CNM. There is no obvious problem with a model in which 10–20% of the HI in DLAs with strong CII* λ 1335.7 absorption is CNM (as suggested by Fig. 19), and with all the CII* λ 1335.7 absorption produced by the CNM. There are three DLAs at $z > 1.7$ that show both HI 21cm and strong CII* λ 1335.7 absorption; these are

the absorbers at $z \sim 1.9436$ towards 1157+014, $z \sim 2.0395$ towards 0458–020 and $z \sim 3.3869$ towards 0201+113. The three absorbers have inferred CNM fractions of $\approx 9 - 17\%$ and intermediate metallicities, $[Z/H] \approx -1.3$ (see Section 7.7 and Tables 4 and 6); these are not inconsistent with the observed strong CII* $\lambda 1335.7$ absorption. In fact, given that these DLAs all have high column densities, $N_{\text{HI}} \geq 1.8 \times 10^{21} \text{ cm}^{-2}$, it is possible that the HI column density towards the radio core is lower than that towards the optical quasar by a factor of ≈ 1.5 in these systems (see Section 7.3). The spin temperature estimates in these DLAs could hence be lower, and the inferred CNM fractions higher, by $\approx 50\%$. We emphasize that Wolfe et al. (2003, 2004) only rule out the “pure-WNM” model for such strong CII* $\lambda 1335.7$ absorbers, but do not rule out models with CNM fractions of $\approx 10 - 20\%$ and WNM fractions of $\approx 80 - 90\%$.

The sole absorber in Table 6 for which there remains a clear discrepancy between the CII* $\lambda 1335.7$ and T_s data is the $z = 3.0621$ DLA towards 0336–017. Wolfe et al. (2008) classify this as a “high-cool” DLA, since $\log[l_c/\text{ergs}^{-1}\text{H}^{-1}] = -26.71 \pm 0.10$, while we obtain $T_s > 8890 \times (f/0.68)$. One way of accounting for this difference is a fortuitously high fraction of CNM clouds towards the optical quasar, which do not efficiently cover the more-extended radio core (Wolfe et al. 2003). Following the argument of Kanekar et al. (2007) (in the context of the $z = 3.387$ DLA towards 0201+113), this would still imply a high WNM fraction towards the radio core of 0336–017, since the core is small enough (≤ 224 pc; Kanekar et al. 2009a) to be entirely covered by the extended WNM clouds. Another possibility is that the average HI column density towards the quasar radio core is lower in the $z = 3.0621$ DLA towards 0336–017 than that towards the optical QSO. While the upper limit to the transverse core size is only ≈ 224 pc in the $z = 3.0621$ DLA (i.e. lower than the median for DLAs at $z > 2$), it is possible that there is small-scale structure in the HI distribution, so that the average HI column towards the optical core is a few times larger than that towards the radio core. This is certainly possible along individual sightlines. Finally, it is also possible that some of the CII* $\lambda 1335.7$ absorption along this sightline arises in either the WNM or ionized gas (Srianand et al. 2005).

Finally, the $z = 1.7764$ DLA towards 1331+170 is a “low-cool” DLA, with $\log[l_c/\text{ergs}^{-1}\text{H}^{-1}] < -27.12$ (Wolfe et al. 2008; Jorgenson et al. 2010). This has $T_s = (625 \pm 115) \times (f/0.72)$ K and a CNM fraction of $\leq 15\%$, derived from a new HI 21cm absorption spectrum (Carswell et al. 2011) and the VLBA covering factor of $f = 0.72$ (Kanekar et al. 2009a). There is no significant contradiction between the T_s and CII* $\lambda 1335.7$ results in this absorber, since both suggest high WNM fractions. However, it is difficult to reconcile the weak CII* $\lambda 1335.7$ absorption with the fact that H₂ and CI absorption have both been detected in this DLA (Meyer et al. 1986; Cui et al. 2005; Jorgenson et al. 2010), clearly indicating the presence of CNM in the absorber (as is also shown by the detected HI 21cm absorption). Indeed, the H₂ fraction in the $z = 1.7764$ DLA is one of the highest in the entire DLA sample (Cui et al. 2005; Noterdaeme et al. 2008). Despite this, CII* $\lambda 1335.7$ absorption is not detected (or is, at best, quite weak) in this absorber (Jorgenson et al. 2010). Similarly, the CII* $\lambda 1335.7$ absorption is weak in the $z = 2.431$ DLA towards 2343+125 ($\log[l_c/\text{ergs}^{-1}\text{H}^{-1}] = -27.09 \pm 0.10$), despite the presence of H₂ absorption in this system and a high metallicity, $[Z/H] = -0.54 \pm 0.01$ (Petitjean et al. 2006). It thus appears that, contrary to the discussion in Wolfe et al. (2004), the absence of CII* $\lambda 1335.7$ absorption does not imply the absence of CNM in individual DLAs, while, conversely, the presence of strong CII* $\lambda 1335.7$ absorption

merely indicates the presence of CNM, and not necessarily a high CNM fraction.

In summary, we find that there is no significant discrepancy between the CII* $\lambda 1335.7$ results of Wolfe et al. (2003, 2004) and our results from HI 21cm absorption studies. The anti-correlation between metallicity and spin temperature is consistent with the finding of Wolfe et al. (2008) that DLAs with high metallicities tend to be “high-cool” systems, while those with low metallicities have low cooling rates. The apparent discrepancy between the results is because Wolfe et al. (2003) (and later papers) only considered two models, one with half the gas each in the CNM and WNM and the other with all the gas in the WNM. Both the CII* $\lambda 1335.7$ and HI 21cm absorption results appear to be consistent with a model in which (1) high-metallicity ($[Z/H] \gtrsim -0.5$) DLAs have high CNM fractions, $\approx 50\%$, (2) intermediate-metallicity DLAs (with $[Z/H] \approx -1$) have 10 – 20% of the neutral gas in the CNM, with this phase producing the CII* $\lambda 1335.7$ and HI 21cm absorption, and (3) low-metallicity DLAs ($[Z/H] \lesssim -1.5$) have most of their gas in the WNM, with low cooling rates and high spin temperatures.

7.12 Comparing CNM and molecular fractions

It is also interesting to compare the inferred CNM fractions f_{CNM} in DLAs (from Section 7.7 to the molecular hydrogen fraction $f_{\text{H}_2} \equiv 2N(\text{H}_2)/(2N(\text{H}_2) + N_{\text{HI}})$, for absorbers with estimates of both quantities. Since both trace the presence of cold gas, a relation between f_{CNM} and f_{H_2} might provide information on the process of molecule formation in DLAs. Searches for molecular hydrogen have now been carried out in nearly a hundred DLAs, mostly with high-resolution optical spectroscopy (e.g. Levshakov & Varshalovich 1985; Petitjean et al. 2000; Ledoux et al. 2003; Cui et al. 2005; Petitjean et al. 2006; Noterdaeme et al. 2008). However, detections of H₂ absorption have been obtained in only $\approx 16\%$ of DLAs at $z > 2$, with most absorbers showing low molecular fractions, $f_{\text{H}_2} \leq 10^{-5}$ (e.g. Ledoux et al. 2003; Noterdaeme et al. 2008). Detections of H₂ absorption have been obtained in DLAs with relatively high metallicity and dust depletion, $[X/\text{Fe}] > 0.4$ (Noterdaeme et al. 2008). This is consistent with the anti-correlation obtained between spin temperature and metallicity, as high-metallicity absorbers should have higher CNM fractions and are thus more likely to form the molecular phase.

Unfortunately, there are at present only 9 DLAs with estimates of both f_{CNM} and f_{H_2} . Most of these have also been observed in the CII* $\lambda 1335.7$ line and are listed in the upper part of Table 6. Three additional systems with searches for HI 21cm and H₂, but not CII* $\lambda 1335.7$, absorption are listed in the lower part of the table. The two H₂ absorbers of this sub-sample, at $z = 1.7764$ towards 1331+170 and $z = 3.3869$ towards 0201+113, both show HI 21cm absorption. However, H₂ absorption was not detected in two HI 21cm absorbers, at $z = 2.0395$ towards 0458–020 and $z = 2.3476$ towards 0438–436. Five DLAs were detected in neither HI 21cm nor H₂ absorption, with strong upper limits on the molecular fraction ($\log[f_{\text{H}_2}] < -5$) and lower limits on the spin temperature ($T_s > 500$ K). The small sample size makes it difficult to draw any inferences from these results, especially given that all DLAs of the sample have high spin temperatures, $T_s \gtrsim 500$ K. Searches for H₂ absorption in DLAs with low spin temperatures would be of much interest.

8 SUMMARY

We have carried out a deep search for redshifted HI 21cm absorption in a large sample of DLAs at $0.68 < z < 3.44$ with the GMRT, the GBT and the WSRT. This has yielded detections of HI 21cm absorption in two new DLAs, at $z = 3.387$ towards 0201+113 and $z = 2.347$ towards 0438–436, and confirmations of detections in two known HI 21cm absorbers. We present evidence that the HI 21cm absorption from one of the DLAs, at $z = 2.0395$ towards 0458–020, has varied on timescales of ≈ 2 months. Similar variability in the HI 21cm absorption profile has been earlier reported on even shorter timescales in two DLAs.

We have also used the VLBA to obtain high spatial resolution images of a sample of background quasars with foreground DLAs or HI 21cm absorbers at frequencies close to the redshifted HI 21cm line frequency, in order to estimate the quasar core fraction. We assume that the DLA covering factor is the same as this core fraction. We have used our measurements of the HI 21cm optical depth and the DLA covering factor in conjunction with the known HI column density from the Lyman- α profile to estimate the spin temperature of each absorber. Finally, we report metallicity, abundance and velocity width measurements for a set of DLAs with HI 21cm absorption spectroscopy, from either our own observations or archival data.

We have combined our results with data from the literature to compile a sample of 37 DLAs with spin temperatures derived from a combination of the Lyman- α profile, HI 21cm absorption spectroscopy and low-frequency VLBI estimates of the absorber covering factor. This sample does not include PDLAs, where the spin temperature could be influenced by the proximity of the absorber to the background quasar, or sub-DLAs, where the spin temperature may be affected by self-shielding issues. The HI column density distribution of this sample is statistically indistinguishable from that of the much larger sample of all known DLAs, including absorbers detected in the SDSS. 29 DLAs of the sample have estimates of the gas metallicity $[Z/H]$, 26 of the dust depletion $[Z/Fe]$, and 24 of the velocity width between 90% optical depth points, ΔV_{90} .

The main results of the paper are:

- We find that the spatial extent of the quasar radio core at the foreground absorber redshift (as estimated from the VLBI images) is larger for high- z DLAs than for low- z DLAs. However, these are *upper limits* to the transverse core size, due to the possibility of residual phase errors in the VLBA data. This is especially important for lower-frequency VLBI images, due to ionospheric effects; DLAs at $z > 2$ are thus the worst affected of the sample. Despite this, the median upper limit to the transverse core size is ≈ 130 pc for the full sample, while that for $z > 2$ DLAs is ≈ 350 pc. For all DLAs but one, the maximum value for the (upper limit to the) transverse core size is ≈ 1 kpc. These are significantly lower than the size of a typical galaxy. We conclude that the foreground DLAs are likely to cover at least the radio cores for all the 37 DLAs of the sample.

- We have examined whether the use of the HI column density derived from the pencil-beam optical sightline in the equation for the HI 21cm optical depth for the sightline towards the radio emission can cause systematic effects in the spin temperature estimates. This was done by smoothing a high-spatial-resolution (15 pc) HI 21cm emission cube of the LMC to coarser resolutions, out to ≈ 1 kpc, to test whether the HI column densities measured from the smoothed spectral cubes are systematically different from those at the highest spatial resolution. We find that the HI column densities in the smoothed cube are systematically larger than those

in the 15 pc cube for $N_{\text{HI}} \lesssim 1 \times 10^{21} \text{ cm}^{-2}$, and systematically lower than those in the 15 pc cube for $N_{\text{HI}} \gtrsim 1 \times 10^{21} \text{ cm}^{-2}$. In other words, the use of the HI column density from the damped Lyman- α profile in the equation for the HI 21cm optical depth will tend to under-estimate the spin temperature for DLAs with $N_{\text{HI}} \lesssim 1 \times 10^{21} \text{ cm}^{-2}$, and to over-estimate the spin temperature for DLAs with $N_{\text{HI}} \gtrsim 1 \times 10^{21} \text{ cm}^{-2}$ (assuming that the spatial distribution of neutral gas in DLAs is similar to that in the LMC). We estimated the magnitude of this effect at two spatial resolutions, 67 pc and 345 pc, approximately the median transverse size of the radio cores at the DLA redshifts for DLAs at $z < 2$ and $z > 2$, respectively. We find that the effect is not very significant, within a factor of 25% for most of the DLAs of the sample, except for systems at low and very high N_{HI} values ($N_{\text{HI}} < 4 \times 10^{20} \text{ cm}^{-2}$ and $N_{\text{HI}} > 5.5 \times 10^{21} \text{ cm}^{-2}$, respectively) and with large core sizes. At these extremes of the N_{HI} distribution, the spin temperature could be under-estimated by up to a factor of 2 for $N_{\text{HI}} \approx 2 \times 10^{20} \text{ cm}^{-2}$, or over-estimated by up to a factor of 1.5 for $N_{\text{HI}} \approx 6 \times 10^{21} \text{ cm}^{-2}$. Since there are far more DLAs at low N_{HI} values than at extremely high ones, the overall effect is to give a weak bias of the spin temperature distribution of high- z DLAs towards lower values.

- We have examined the full sample of DLAs for trends between different quantities, including the detection rate of HI 21cm absorption, the spin temperature, the HI column density, the covering factor, the metallicity, the dust depletion, the velocity width at 90% optical depth, etc. Survival analysis methods, as implemented in the ASURV package, were used to appropriately handle censored data.

We found no evidence that the detection rate of HI 21cm absorption depends on the HI column density, the absorber covering factor, the DLA metallicity or the velocity width at 90% optical depth. For all these variables, the detection rates of HI 21cm absorption above and below the median value were found to be consistent with each other within the statistical uncertainties. Similarly, there is no statistically-significant evidence that the estimated DLA spin temperatures depend on the absorber covering factor, the HI column density or the velocity width at 90% optical depth. However, we caution that the sample size of DLAs with HI 21cm absorption studies is still quite small and the above detection rates are dominated by Poisson errors. It is plausible that larger absorber samples will indeed show that the detection rates do depend on, e.g., the metallicity and the covering factor.

The detection rate of HI 21cm absorption in high- z DLAs (with $z > z_{\text{med}}$, where $z_{\text{med}} = 2.192$) is $17_{-9}^{+16}\%$, while that in low- z DLAs (with $z < z_{\text{med}}$) is $83_{-21}^{+17}\%$. The difference between the two detection rates has $\approx 2.6\sigma$ significance. This is tentative evidence that the probability of detecting HI 21cm absorption increases with decreasing redshift.

- We detect a difference between the spin temperature distributions of absorbers above and below the median redshift, $z_{\text{med}} = 2.192$, at $\approx 3.5\sigma$ significance. The statistical significance of the difference in T_s distributions is even higher, 4.0σ , if the redshift $z = 2.4$ is used to demarcate the low- z and high- z samples.

We have also restricted the low- z sample to absorbers with redshifts $z > 1$, to ensure that the angular diameter distances of the DLAs and their background quasars are similar for all absorbers. Again sub-dividing the sample in low- z ($z < 2.683$) and high- z ($z > 2.683$) DLAs yields a clear difference, with 3.5σ statistical significance, between the T_s distributions of the two sub-samples. Angular diameter distances thus do not appear to play a significant role in the lower HI 21cm optical depths observed in high- z DLAs. We conclude that DLA spin temperatures show clear redshift evo-

lution: the high- z sample contains both a smaller fraction of DLAs with low spin temperatures and a lower detection rate of HI 21cm absorption.

- We also find that the spin temperature distributions in the full sample of DLAs and in the Milky Way are different, at $\approx 6\sigma$ significance. This is definitive evidence that the neutral ISM in DLAs is significantly different from that in the Galaxy, with far smaller CNM fractions ($\lesssim 20\%$) in DLAs than in the Milky Way (median CNM fraction $\approx 27\%$).

- We continue to find that the DLA metallicities and their spin temperatures are anti-correlated: the anti-correlation between $[Z/H]$ and T_s is detected at $\approx 3.5\sigma$ significance in a generalized Kendall-tau test, based on 29 absorbers with estimates of metallicity, spin temperature and covering factor. This supports the conjecture of Kanekar & Chengalur (2001a) that the low CNM fractions in DLAs arise due to a paucity of cooling routes in the absorbers, due to their low metallicities. Differences between the HI column densities along the radio and optical sightlines can only worsen any existing anti-correlation. We find only weak ($\approx 2.4\sigma$) evidence for an anti-correlation between T_s and dust depletion, from 26 systems. It is thus unlikely that the relation between spin temperature and metallicity arises due to an underlying relation between spin temperature and dust depletion.

The DLA spin temperature estimates are based on the assumptions that the quasar core fraction can be interpreted as the DLA covering factor and that the HI column density measured towards the optical quasar is the same as that towards the more-extended radio emission. The metallicity estimates do not make either of these assumptions. If the above assumptions are violated for most of the absorbers, we would not expect to detect an underlying relation between T_s and $[Z/H]$. The fact that the predicted anti-correlation between T_s and $[Z/H]$ is indeed detected indicates that the assumptions are reliable, at least in a statistical sense.

- We have also examined whether the two main results of this paper, viz. the redshift evolution of DLA spin temperatures and the anti-correlation between spin temperature and metallicity, are affected by the assumption that the DLA covering factor is equal to the quasar radio core fraction. This was done via Monte Carlo simulations with DLA spin temperatures inferred assuming (1) an error in the inferred covering factor, with standard deviation ranging from 10 – 100% of the measured core fraction, and (2) entirely random covering factors, selected from a uniform distribution of values between 0 and 1. For both types of errors, the above two results were obtained at $\geq 3\sigma$ significance, after averaging over 10,000 Monte Carlo runs. Our results thus do not appear to critically depend on the assumption that the DLA covering factor is equal to the quasar radio core fraction.

- We have examined the CII* λ 1335.7 model of Wolfe et al. (2003, 2004) in the light of our spin temperature estimates. We find that the CII* λ 1335.7 results are entirely consistent with our results for at least half the DLA sample, the systems with low metallicities and undetected or weak CII* λ 1335.7 absorption. The anti-correlation between metallicity and spin temperature implies that the neutral ISM in such systems should be predominantly WNM, as expected from the low cooling rates derived from the CII* λ 1335.7 model. Similarly, DLAs with high metallicity are expected to have high CNM fractions based on the T_s - $[Z/H]$ anti-correlation and are also expected to have a high cooling rate from their strong CII* λ 1335.7 absorption; the spin temperature and CII* λ 1335.7 results are thus also in agreement for such systems. Thus, the CII* λ 1335.7 results are broadly consistent with the spin temperature results except for a few cases where line-of-sight effects may

be important. Further, even for these cases, the apparent discrepancy between the spin temperature and CII* λ 1335.7 results arises for systems with intermediate metallicity, $[Z/H] \approx -1.3$. We find that the difference essentially arises because Wolfe et al. (2003, 2004) use a CNM+WNM model with 50% of the neutral gas in each phase; such a model is not required by the CII* λ 1335.7 data. It appears possible to alleviate the apparent discrepancy between the CII* λ 1335.7 and the HI 21cm results by considering a model wherein 10 – 20% of the HI in intermediate-metallicity DLAs is in the CNM, producing the majority of the the CII* λ 1335.7 absorption. Such a two-phase model would yield both strong CII* λ 1335.7 absorption and a high spin temperature ($T_s \approx 1000$ K). While it is beyond the scope of the present work to explicitly test this possibility, we conclude that there is no significant disagreement between the CII* λ 1335.7 results and the spin temperature estimates.

ACKNOWLEDGEMENTS

We thank the staff of the GMRT, the GBT, the VLBA, the WSRT, the VLT, the Keck Observatory, the Space Telescope Science Institute and the Gemini Observatory. The GMRT is run by the National Centre for Radio Astrophysics of the Tata Institute of Fundamental Research. The WSRT is operated by ASTRON (the Netherlands Institute for Radio Astronomy), with support from the Netherlands Foundation for Scientific Research (NWO). The NRAO is a facility of the National Science Foundation operated under cooperative agreement by Associated Universities, Inc.. Based on observations obtained at the Gemini Observatory, which is operated by the Association of Universities for Research in Astronomy, Inc., under a cooperative agreement with the NSF on behalf of the Gemini partnership: the National Science Foundation (United States), the Science and Technology Facilities Council (United Kingdom), the National Research Council (Canada), CONICYT (Chile), the Australian Research Council (Australia), Ministério da Ciência, Tecnologia e Inovação (Brazil) and Ministerio de Ciencia, Tecnología e Innovación Productiva (Argentina). Based on observations made with the NASA/ESA Hubble Space Telescope, obtained from the data archive at the Space Telescope Science Institute. STScI is operated by the Association of Universities for Research in Astronomy, Inc. under NASA contract NAS 5-26555. Based on observations made with ESO Telescopes at the Paranal Observatory under programme IDs 67.A-0567, 68.A-0170 and 69.A-0371. Some of the data presented herein were obtained at the W.M. Keck Observatory, which is operated as a scientific partnership among the California Institute of Technology, the University of California and the National Aeronautics and Space Administration. The Observatory was made possible by the generous financial support of the W.M. Keck Foundation. NK acknowledges support from the Department of Science and Technology through a Ramanujan Fellowship. Part of this work was carried out during a visit by NK to ESO-Santiago; he thanks ESO for hospitality. JXP is partly supported by NSF grant AST-1109447. Basic research in radio astronomy at the Naval Research Laboratory is supported by 6.1 base funds. ERW acknowledges the support of Australian Research Council grant DP1095600. We thank Art Wolfe and an anonymous referee for detailed comments on earlier versions of the manuscript that have significantly improved its clarity.

REFERENCES

- Abazajian K. N. et al. 2009, *ApJS*, 182, 543
- Akerman C. J., Ellison S. L., Pettini M., Steidel C. C., 2005, *A&A*, 440, 499
- Akritas M. G., Bershadsky M. A., 1996, *ApJ*, 470, 706
- Asplund M., Grevesse N., Sauval A. J., Scott P., 2009, *ARA&A*, 47, 481
- Bakes E. L. O., Tielens A. G. G. M., 1994, *ApJ*, 427, 822
- Battisti A. J., Meiring J. D., Tripp T. M., Prochaska J. X., Werk J. K., Jenkins E. B., Lehner N., Tumlinson J., Thom C., 2012, *ApJ*, 744, 93
- Becker R. H., White R. L., Helfand D. J., 1995, *ApJ*, 450, 559
- Bergeron J., Stasińska G., 1986, *A&A*, 169, 1
- Boisse P., Le Brun V., Bergeron J., Deharveng J.-M., 1998, *A&A*, 333, 841
- Bowen D. V., Tripp T. M., Jenkins E. B., 2001, *AJ*, 121, 1456
- Braun R., Walterbos R., 1992, *ApJ*, 386, 120
- Briggs F. H., 1983, *AJ*, 88, 239
- Briggs F. H., Brinks E., Wolfe A. M., 1997, *AJ*, 113, 467
- Briggs F. H., de Bruyn A. G., Vermeulen R. C., 2001, *A&A*, 373, 113
- Briggs F. H., Wolfe A. M., 1983, *ApJ*, 268, 76
- Briggs F. H., Wolfe A. M., Liszt H. S., Davis M. M., Turner K. L., 1989, *ApJ*, 341, 650
- Brown B. W. M., Hollander M., Korwar R. M., 1974, in Prochan F., Serfling R. J., eds, *Reliability and Biometry Philadelphia: SIAM*, p. 327
- Brown R. L., Mitchell K. J., 1983, *ApJ*, 264, 87
- Brown R. L., Roberts M. S., 1973, *ApJ*, 184, L7
- Brown R. L., Spencer R. E., 1979, *ApJ*, 230, L1
- Burbidge E. M., Beaver E. A., Cohen R. D., Junkkarinen V. T., Lyons R. W., 1996, *AJ*, 112, 2533
- Carilli C. L., Lane W. M., de Bruyn A. G., Braun R., Miley G. K., 1996, *AJ*, 111, 1830
- Carswell R. F., Jorgenson R. A., Wolfe A. M., Murphy M. T., 2011, *MNRAS*, 411, 2319
- Catinella B., Haynes M. P., Giovanelli R., Gardner J. P., Connolly A. J., 2008, *ApJ*, 685, L13
- Chen H.-W., Kennicutt Jr. R. C., Rauch M., 2005, *ApJ*, 620, 703
- Chengalur J. N., Kanekar N., 1999, *MNRAS*, 302, L29
- Chengalur J. N., Kanekar N., 2000, *MNRAS*, 318, 303
- Chengalur J. N., Kanekar N., 2002, *A&A*, 388, 383
- Chengalur J. N., Kanekar N., 2003, *Phys. Rev. Lett.*, 91, 241302
- Colgan S. W. J., Salpeter E. E., Terzian Y., 1988, *ApJ*, 328, 275
- Condon J. J., Cotton W. D., Greisen E. W., Yin Q. F., Perley R. A., Taylor G. B., Broderick J. J., 1998, *AJ*, 115, 1693
- Cooke R., Pettini M., Steidel C. C., Rudie G. C., Nissen P. E., 2011, *MNRAS*, 417, 1534
- Cui J., Bechtold J., Ge J., Meyer D. M., 2005, *ApJ*, 633, 649
- Curran S. J., 2012, *ApJ*, 748, L18
- Curran S. J., Murphy M. T., Pihlström Y. M., Webb J. K., Purcell C. R., 2005, *MNRAS*, 356, 1509
- Curran S. J., Tzanavaris P., Darling J. K., Whiting M. T., Webb J. K., Bignell C., Athreya R., Murphy M. T., 2010, *MNRAS*, 402, 35
- Curran S. J., Tzanavaris P., Pihlström Y. M., Webb J. K., 2007, *MNRAS*, 382, 1331
- Curran S. J., Webb J. K., 2006, *MNRAS*, 371, 356
- de Bruyn A. G., O'Dea C. P., Baum S. A., 1996, *A&A*, 305, 450
- de la Varga A., Reimers D., Tytler D., Barlow T., Burles S., 2000, *A&A*, 363, 69
- Dessauges-Zavadsky M., Calura F., Prochaska J. X., D'Odorico S., Matteucci F., 2004, *A&A*, 416, 79
- Dessauges-Zavadsky M., Calura F., Prochaska J. X., D'Odorico S., Matteucci F., 2007, *A&A*, 470, 431
- Dessauges-Zavadsky M., Prochaska J. X., D'Odorico S., Calura F., Matteucci F., 2006, *A&A*, 445, 93
- Dickey J. M., Lockman F. J., 1990, *ARA&A*, 28, 215
- Douglas J. N., Bash F. N., Bozayan F. A., Torrence G. W., Wolfe C., 1996, *AJ*, 111, 1945
- Drinkwater M. J., Webb J. K., Barrow J. D., Flambaum V. V., 1998, *MNRAS*, 295, 457
- Ellison S. L., Kanekar N., Prochaska J. X., Momjian E., Worseck G., 2012, *MNRAS*, 424, 293
- Ellison S. L., Pettini M., Steidel C. C., Shapley A. E., 2001, *ApJ*, 549, 770
- Ellison S. L., Ryan S. G., Prochaska J. X., 2001, *MNRAS*, 326, 628
- Ellison S. L., Yan L., Hook I. M., Pettini M., Wall J. V., Shaver P., 2001, *A&A*, 379, 393
- Ellison S. L., Yan L., Hook I. M., Pettini M., Wall J. V., Shaver P., 2002, *A&A*, 383, 91
- Ellison S. L., York B. A., Pettini M., Kanekar N., 2008, *MNRAS*, 388, 1349
- Erb D. K., Shapley A. E., Pettini M., Steidel C. C., Reddy N. A., Adelberger K. L., 2006, *ApJ*, 644, 813
- Field G. B., 1958, *Proc. I. R. E.*, 46, 240
- Field G. B., 1959, *ApJ*, 129, 536
- Field G. B., Goldsmith D. W., Habing H. J., 1969, *ApJ*, 155, L149
- Fontana A., Ballester P., 1995, *The Messenger*, 80, 37
- Fumagalli M., O'Meara J. M., Prochaska J. X., Kanekar N., 2010, *MNRAS*, 408, 362
- Fynbo J. P. U., Laursen P., Ledoux C., Møller P., Durgapal A. K., Goldoni P., Gullberg B., Kaper L., Maund J., Noterdaeme P., Östlin G., Strandet M. L., Toft S., Vreeswijk P. M., Zafar T., 2010, *MNRAS*, 408, 2128
- Fynbo J. P. U., Ledoux C., Noterdaeme P., Christensen L., Møller P., Durgapal A. K., Goldoni P., Kaper L., Krogager J.-K., Laursen P., Maund J. R., Milvang-Jensen B., Okoshi K., Rasmussen P. K., Thorsen T. J., Toft S., Zafar T., 2011, *MNRAS*, 413, 2481
- Ge J., Bechtold J., 1997, *ApJ*, 477, L73
- Ge J., Bechtold J., Kulkarni V. P., 2001, *ApJ*, 547, L1
- Gehrels N., 1986, *ApJ*, 303, 336
- Gupta N., Srianand R., Petitjean P., Noterdaeme P., Saikia D. J., 2009, *MNRAS*, 398, 201
- Gwinn C. R., 2001, *ApJ*, 561, 815
- Haehnelt M. G., Steinmetz M., Rauch M., 1998, *ApJ*, 495, 64
- Heiles C., Troland T. H., 2003, *ApJS*, 145, 329
- Heiles C., Troland T. H., 2003, *ApJ*, 586, 1067
- Heinmüller J., Petitjean P., Ledoux C., Caucci S., Srianand R., 2006, *A&A*, 449, 33
- Isobe T., Feigelson E. D., Nelson P. I., 1986, *ApJ*, 306, 490
- Jorgenson R. A., Wolfe A. M., Prochaska J. X., 2010, *ApJ*, 722, 460
- Jorgenson R. A., Wolfe A. M., Prochaska J. X., Lu L., Howk J. C., Cooke J., Gawiser E., Gelino D. M., 2006, *ApJ*, 646, 730
- Junkkarinen V. T., Cohen R. D., Beaver E. A., Burbidge E. M., Lyons R. W., Madejski G., 2004, *ApJ*, 614, 658
- Kanekar N., Braun R., Roy N., 2011, *ApJ*, 737, L33
- Kanekar N., Briggs F. H., 2004, *New Astr. Rev.*, 48, 1259
- Kanekar N., Chengalur J. N., 1997, *MNRAS*, 292, 831
- Kanekar N., Chengalur J. N., 2001a, *A&A*, 369, 42

- Kanekar N., Chengalur J. N., 2001b, *MNRAS*, 325, 631
- Kanekar N., Chengalur J. N., 2003, *A&A*, 399, 857
- Kanekar N., Chengalur J. N., 2005, in Williams P., Shu C.-G., Menard B., eds, *IAU Colloq. 199: Probing Galaxies through Quasar Absorption Lines* Cambridge University Press, Cambridge, p. 156
- Kanekar N., Chengalur J. N., Lane W. M., 2007, *MNRAS*, 375, 1528
- Kanekar N., Ellison S. L., Momjian E., York B., Pettini M., 2013, *MNRAS*, 428, 532
- Kanekar N., Ghosh T., Chengalur J. N., 2001, *A&A*, 373, 394
- Kanekar N., Lane W. M., Momjian E., Briggs F. H., Chengalur J. N., 2009a, *MNRAS*, 394, L61
- Kanekar N., Prochaska J. X., Ellison S. L., Chengalur J. N., 2009b, *MNRAS*, 396, 385
- Kanekar N., Smette A., Briggs F. H., Chengalur J. N., 2009c, *ApJ*, 705, L40
- Kanekar N., Subrahmanyan R., Chengalur J. N., Safouris V., 2003, *MNRAS*, 346, L57
- Kanekar N., Subrahmanyan R., Ellison S. L., Lane W. M., Chengalur J. N., 2006, *MNRAS*, 370, L46
- Kellermann K. I., Pauliny-Toth I. I. K., 1969, *ApJL*, 155, L71
- Khare P., Kulkarni V. P., Lauroesch J. T., York D. G., Crotts A. P. S., Nakamura O., 2004, *ApJ*, 616, 86
- Kim S., Staveley-Smith L., Dopita M. A., Sault R. J., Freeman K. C., Lee Y., Chu Y.-H., 2003, *ApJS*, 148, 473
- Kulkarni V. P., Fall S. M., Lauroesch J. T., York D. G., Welty D. E., Khare P., Truran J. W., 2005, *ApJ*, 618, 68
- Kulkarni V. P., Khare P., Som D., Meiring J., York D. G., Péroux C., Lauroesch J. T., 2010, *New Astronomy*, 15, 735
- Lane W., Smette A., Briggs F., Rao S., Turnshek D., Meylan G., 1998, *AJ*, 116, 26
- Lane W. M., Briggs F. H., Smette A., 2000, *ApJ*, 532, 146
- Lanzetta K. M., Bowen D. V., 1992, *ApJ*, 391, 48
- Launay J.-M., Roueff E., 1977, *Journal of Physics B Atomic Molecular Physics*, 10, 879
- le Brun V., Bergeron J., Boissé P., Deharveng J.-M., 1997, *A&A*, 321, 733
- Ledoux C., Bergeron J., Petitjean P., 2002, *A&A*, 385, 802
- Ledoux C., Petitjean P., Fynbo J. P. U., Møller P., Srianand R., 2006, *A&A*, 457, 71
- Ledoux C., Petitjean P., Srianand R., 2003, *MNRAS*, 346, 209
- Levshakov S. A., Varshalovich D. A., 1985, *MNRAS*, 212, 517
- Lindler D., 1999, *NASA/LASP, Greenbelt, MD*
- Liszt H., 2001, *A&A*, 371, 698
- Lopez S., Ellison S. L., 2003, *A&A*, 403, 573
- Lopez S., Reimers D., Gregg M. D., Wisotzki L., Wucknitz O., Guzman A., 2005, *ApJ*, 626, 767
- Lu L., Sargent W. L. W., Barlow T. A., Churchill C. W., Vogt S. S., 1996, *ApJS*, 107, 475
- Lu L., Wolfe A. M., Turnshek D. A., Lanzetta K. M., 1993, *ApJS*, 84, 1
- Macquart J.-P., 2005, *A&A*, 433, 827
- McKee C. F., Ostriker J. P., 1977, *ApJ*, 218, 148
- Meyer D. M., York D. G., Black J. H., Chaffee Jr. F. H., Foltz C. B., 1986, *ApJ*, 308, L37
- Milutinovic N., Ellison S. L., Prochaska J. X., Tumlinson J., 2010, *MNRAS*, 408, 2071
- Møller P., Fynbo J. P. U., Fall S. M., 2004, *A&A*, 422, L33
- Møller P., Warren S. J., 1993, *A&A*, 270, 43
- Møller P., Warren S. J., Fynbo J. U., 1998, *A&A*, 330, 19
- Monier E. M., Turnshek D. A., Rao S., 2009, *MNRAS*, 397, 943
- Murphy M. T., Curran S. J., Webb J. K., Ménager H., Zych B. J., 2007, *MNRAS*, 376, 673
- Neeleman M. et al. 2013, *ApJ* (submitted)
- Nestor D., Pettini M., Hewett P., Rao S., Wild V., 2008, *MNRAS*, 390, 1670
- Noterdaeme P. et al. 2012, *A&A*, 547, L1
- Noterdaeme P., Laursen P., Petitjean P., Vergani S. D., Maureira M.-J., Ledoux C., Fynbo J. P. U., López S., Srianand R., 2012, *A&A*, 540, 63
- Noterdaeme P., Ledoux C., Petitjean P., Srianand R., 2008, *A&A*, 481, 327
- Noterdaeme P., Petitjean P., Ledoux C., Srianand R., 2009, *A&A*, 505, 1087
- Noterdaeme P., Petitjean P., Srianand R., Ledoux C., López S., 2011, *A&A*, 526, L7
- Nulsen P. E. J., Barcons X., Fabian A. C., 1998, *MNRAS*, 301, 168
- Penprase B. E., Prochaska J. X., Sargent W. L. W., Toro-Martinez I., Beeler D. J., 2010, *ApJ*, 721, 1
- Péroux C., Bouché N., Kulkarni V. P., York D. G., Vladilo G., 2012, *MNRAS*, 419, 3060
- Péroux C., Dessauges-Zavadsky M., D’Odorico S., Kim T., McMahon R. G., 2003, *MNRAS*, 345, 480
- Petitjean P., Ledoux C., Noterdaeme P., Srianand R., 2006, *A&A*, 456, L9
- Petitjean P., Ledoux C., Srianand R., 2008, *A&A*, 480, 349
- Petitjean P., Srianand R., Ledoux C., 2000, *A&A*, 364, L26
- Pettini M., Ellison S. L., Steidel C. C., Bowen D. V., 1999, *ApJ*, 510, 576
- Pettini M., Ellison S. L., Steidel C. C., Shapley A. E., Bowen D. V., 2000, *ApJ*, 532, 65
- Pettini M., Smith L. J., Hunstead R. W., King D. L., 1994, *ApJ*, 426, 79
- Pettini M., Smith L. J., King D. L., Hunstead R. W., 1997, *ApJ*, 486, 665
- Pettini M., Zych B. J., Steidel C. C., Chaffee F. H., 2008, *MNRAS*, 385, 2011
- Planck Collaboration 2013, *arxiv:1303.5076*
- Pottasch S. R., Wesselius P. R., van Duinen R. J., 1979, *A&A*, 74, L15
- Prochaska J. X., 1999, *ApJL*, 511, L71
- Prochaska J. X., Chen H.-W., Wolfe A. M., Dessauges-Zavadsky M., Bloom J. S., 2008, *ApJ*, 672, 59
- Prochaska J. X., Gawiser E., Wolfe A. M., Castro S., Djorgovski S. G., 2003, *ApJ*, 595, L9
- Prochaska J. X., Gawiser E., Wolfe A. M., Cooke J., Gelino D., 2003, *ApJS*, 147, 227
- Prochaska J. X., Hennawi J. F., Herbert-Fort S., 2008, *ApJ*, 675, 1002
- Prochaska J. X., Herbert-Fort S., Wolfe A. M., 2005, *ApJ*, 635, 123
- Prochaska J. X., Wolfe A. M., 1997, *ApJ*, 487, 73
- Prochaska J. X., Wolfe A. M., 1999, *ApJS*, 121, 369
- Prochaska J. X., Wolfe A. M., 2009, *ApJ*, 696, 1543
- Prochaska J. X., Wolfe A. M., 2010, *arxiv:1009.3960*
- Prochaska J. X., Wolfe A. M., Howk J. C., Gawiser E., Burles S. M., Cooke J., 2007, *ApJS*, 171, 29
- Prochaska J. X., Wolfe A. M., Tytler D., Burles S., Cooke J., Gawiser E., Kirkman D., O’Meara J. M., Storrie-Lombardi L., 2001, *ApJS*, 137, 21
- Rafelski M., Wolfe A. M., Prochaska J. X., Neeleman M., Mendez A. J., 2012, *ApJ*, 755, 89

- Rao S. M., Turnshek D. A., 1998, *ApJL*, 500, L115
- Rao S. M., Turnshek D. A., 2000, *ApJS*, 130, 1
- Rao S. M., Turnshek D. A., Nestor D. B., 2006, *ApJ*, 636, 610
- Readhead A. C. S., 1994, *ApJ*, 426, 51
- Roberts M. S., Brown R. L., Brundage W. D., Rots A. H., Haynes M. P., Wolfe A. M., 1976, *AJ*, 81, 293
- Rohlf K., Wilson T. L., 2006, *Tools of Radio Astronomy*, 4th ed. Berlin: Springer
- Roy N., Mathur S., Gajjar V., Patra, N. N., 2013, *MNRAS*, 436, L94
- Ryan-Weber E. V., Staveley-Smith L., Webster R. L., 2005, *MNRAS*, 364, L51
- Savage B. D., Sembach K. R., 1991, *ApJ*, 379, 245
- Savaglio S., Glazebrook K., Le Borgne D., Juneau S., Abraham R. G., Chen H.-W., Crampton D., McCarthy P. J., Carlberg R. G., Marzke R. O., Roth K., Jørgensen I., Murowinski R., 2005, *ApJ*, 635, 260
- Schaye J., 2001, *ApJ*, 562, L95
- Singal A. K., 2009, *ApJL*, 703, L109
- Smette A., Robertson J. G., Shaver P. A., Reimers D., Wisotzki L., Koehler T., 1995, *A&AS*, 113, 199
- Srianand R., Gupta N., Petitjean P., Noterdaeme P., Ledoux C., 2010, *MNRAS*, 405, 1888
- Srianand R., Gupta N., Petitjean P., Noterdaeme P., Ledoux C., Salter C. J., Saikia D. J., 2012, *MNRAS*, 421, 651
- Srianand R., Petitjean P., Ledoux C., Ferland G., Shaw G., 2005, *MNRAS*, 362, 549
- Steidel C. C., Bowen D. V., Blades J. C., Dickinson M., 1995, *ApJ*, 440, L45
- Storrie-Lombardi L. J., Wolfe A. M., 2000, *ApJ*, 543, 552
- Tremonti C. A., Heckman T. M., Kauffmann G., Brinchmann J., Charlot S., White S. D. M., Seibert M., Peng E. W., Schlegel D. J., Uomoto A., Fukugita M., Brinkmann J., 2004, *ApJ*, 613, 898
- Viegas S. M., 1995, *MNRAS*, 276, 268
- Vogt S. S. et al. 1994, in Crawford D. L., Craine E. R., eds, *Society of Photo-Optical Instrumentation Engineers (SPIE) Conference Series Vol. 2198 of Society of Photo-Optical Instrumentation Engineers (SPIE) Conference Series*, HIREs: the high-resolution echelle spectrometer on the Keck 10-m Telescope. p. 362
- Wakker B. P., Lockman F. J., Brown J. M., 2011, *ApJ*, 728, 159
- Warren S. J., Møller P., Fall S. M., Jakobsen P., 2001, *MNRAS*, 326, 759
- Welty D. E., Xue R., Wong T., 2012, *ApJ*, 745, 173
- White R. L., Kinney A. L., Becker R. H., 1993, *ApJ*, 407, 456
- Wolfe A. M., Briggs F. H., Davis M. M., 1982, *ApJ*, 259, 495
- Wolfe A. M., Briggs F. H., Jauncey D. L., 1981, *ApJ*, 248, 460
- Wolfe A. M., Briggs F. H., Turnshek D. A., Davis M. M., Smith H. E., Cohen R. D., 1985, *ApJ*, 294, L67
- Wolfe A. M., Broderick J. J., Condon J. J., Johnston K. J., 1976, *ApJ*, 208, L47
- Wolfe A. M., Burbidge G. R., 1975, *ApJ*, 200, 548
- Wolfe A. M., Davis M. M., 1979, *AJ*, 84, 699
- Wolfe A. M., Gawiser E., Prochaska J. X., 2003, *ApJ*, 593, 235
- Wolfe A. M., Gawiser E., Prochaska J. X., 2005, *ARA&A*, 43, 861
- Wolfe A. M., Howk J. C., Gawiser E., Prochaska J. X., Lopez S., 2004, *ApJ*, 615, 625
- Wolfe A. M., Jorgenson R. A., Robishaw T., Heiles C., Prochaska J. X., 2008, *Nature*, 455, 638
- Wolfe A. M., Prochaska J. X., 1998, *ApJ*, 494, L15
- Wolfe A. M., Prochaska J. X., Gawiser E., 2003, *ApJ*, 593, 215
- Wolfe A. M., Prochaska J. X., Jorgenson R. A., Rafelski M., 2008, *ApJ*, 681, 881
- Wolfe A. M., Turnshek D. A., Lanzetta K. M., Lu L., 1993, *ApJ*, 404, 480
- Wolfire M. G., Hollenbach D., McKee C. F., Tielens A. G. G. M., Bakes E. L. O., 1995, *ApJ*, 443, 152
- Wolfire M. G., McKee C. F., Hollenbach D., Tielens A. G. G. M., 2003, *ApJ*, 587, 278
- Wright E. L. et al. 1991, *ApJ*, 381, 200
- York B. A., Kanekar N., Ellison S. L., Pettini M., 2007, *MNRAS*, 382, L53
- Zuo L., Beaver E. A., Burbidge E. M., Cohen R. D., Junkkarinen V. T., Lyons R. W., 1997, *ApJ*, 477, 568
- Zwaan M., Walter F., Ryan-Weber E., Brinks E., de Blok W. J. G., Kennicutt R. C., 2008, *AJ*, 136, 2886
- Zwaan M. A., van der Hulst J. M., Briggs F. H., Verheijen M. A. W., Ryan-Weber E. V., 2005, *MNRAS*, 364, 1467